Graphene coated fabrics for triboelectric nanogenerators

Author:
Kavya Sreeja Sadanandan

Supervisors:
Dr. Ana I S Neves
Prof. Monica F Craciun

A thesis submitted in fulfilment of the requirements
for the degree of Doctor of Philosophy in Physics/Engineering
in the
Department of Engineering
University of Exeter

Declaration of Authorship

- Submitted by Kavya Sreeja Sadanandan to the University of Exeter as a thesis for the degree of Doctor of Philosophy in Physics/Engineering, January 2023
- This thesis is available for Library use on the understanding that it is copyright material and that no quotation from the thesis may be published without proper acknowledgement
- I certify that all material in this thesis which is not my own work has been identified and that any material that has previously been submitted and approved for the award of a degree by this or any other University has been acknowledged
- Any queries regarding this thesis and relevant works should be addressed to the author, Kavya Sreeja Sadanandan via the email ks720@exeter.ac.uk

Signed:

Date:

Abstract

In this thesis, graphene-based, textile triboelectric nanogenerators (TENG) are fabricated towards energy harvesting for wearable applications. These devices are characterised and demonstrated by their ability to power up low-power electronics.

Graphene suspension is coated on textile substrates to fabricate the electrodes for these wearable devices. To this end, a novel deposition method, i.e. ultrasonic spray coating is developed and optimised for various textile fabric substrates. Using ultraviolet ozone treatments on the fabric surfaces is shown here to improve the interaction of graphene with the fabric, reducing the electrical resistance of the coated fabric compared to the non-treated fabric. Electrodes fabricated this way displayed a good range of conductivity, and resilience to varying degrees of bending, compression and tensile tests.

These textile electrodes are used in the fabrication of TENGs along with a dielectric layer of polydimethylsiloxane (PDMS) polymer on one side and a test material typically nylon fabric or nitrile rubber on the other. Different parameters affecting the TENG output such as chemical modification of the PDMS layer, frequency, contact force, contact area and separation distance between the two tribolayers are studied separately in detail to understand the working of the device and as ways to enhance the TENG output. A lower range is maintained for each parameter considering the application is towards wearable devices. TENG tested here were able to produce a power output of up to 330 mW/m^2 at 60 MΩ resistance. A maximum output of 397 V and 7.7 μA were obtained for the PDMS side tested against nylon fabric at 10 mm separation, 35 N contact force at 1 Hz frequency.

Finally, the ability of this wearable TENG device to power up low-power electronic devices was demonstrated by lighting up commercial LEDs and lab-made OLEDs. Potential applications of this device as a pressure sensor in remote health monitoring are also discussed along with possibilities of ultrasonic spray coating of graphene in applications outside electrode fabrications.

Acknowledgement

Firstly, I would like to thank my supervisors Ana and Monica. Their continuous guidance and knowledge of the field have helped me tremendously to understand and experiment with the project. Your feedback on my writing, experiments and result analysis were extremely beneficial for me to identify my strengths and weakness in those areas and work on them. I would like to thank my labmate, Zakaria for the insights into the electrical characterisation part of my project, guiding me and designing the set-ups required for the work. I would like to thank Agnes Bacon for helping me with the sheet resistance measurements in the first half of my project, your contributions were really helpful in publishing my first paper. I would also like to thank Ievgeniia, Ineta, Kieran and Conor for all the help, discussions and collaborations we had throughout.

I would like to acknowledge the training and guidance provided by Hong on my SEM measurements, Mark for RIE, Tommy for optical profilometry and Julian for tensile strength measurements. These were really useful for the characterisation part of my work and I am thankful for your help.

I would like to thank Connor, for being there for me throughout my ups and downs. I am really thankful for your constant support and encouragement. I would like to thank my former housemate and friend Iago. I always looked forward to our brunch catch-ups, movie outs, trekking and tea breaks. You were really a source of comfort for me. I would also like to thank my friend Huanling for the conversations, dinner nights and summer ball we enjoyed together.

Last but not least, I would like to thank my family, my Amma, Achan and my sister for being my cheerleaders from the beginning, for believing in my dreams and for their constant support and love.

I would like to acknowledge the funding provided by the EPSRC centre for doctoral training in metamaterials (EP/L015331/1).

Dedicated to my family

Publications

- Kavya Sreeja Sadanandan, Agnes Bacon, Dong-Wook Shin, Saad F R Alkhalifa, Saverio Russo, Monica F Craciun, Ana I S Neves, 'Graphene coated fabrics by ultrasonic spray coating for wearable electronics and smart textiles', JPhys Mater. 4 (2021). https://doi.org/10.1088/2515-7639/abc632.
- (In preparation) Kavya Sreeja Sadanandan, Zakaria Saadi, Conor Murphy, Ineta Grikalaite, Monica F Craciun, Ana I S Neves, 'Fabric based triboelectric nanogenerators with ultrasonic spray coated graphene electrode for self-powered wearable devices'

Conferences & Workshop

- Attended the workshop on Intensive Course in Layered Materials and Applications, 2021.
- Oral presentation on 'Graphene coated fabrics by ultrasonic spray coating for wearable electronics and smart textiles' at Graphene 2020 virtual conference.
- Attended and presented a poster at the 12th International Symposium on Flexible Organic Electronics (ISFOE) 2019, Thessaloniki, Greece.
- Attended and presented a poster on 'Fabrication of wearable triboelectric nanogenerators' at the Materials for Clean Energy Conference (MCEC) 2019, National Physical Laboratory, London.

Contents

List of Figures

List of Tables

Chapter 1

Introduction & Literature review

Wearable electronics include devices that can be worn as a part of clothing or accessories. The most common ones in our daily lives are spectacles to smart glasses and wristwatches to fit bands. Naturally, the next step is to include additional functionalities to these wearable devices and improve the experience of the existing ones. Incorporation of these devices into textiles (in fibre, yarn or fabric level) can tremendously simplify our day-to-day life. For example, by adding health monitoring sensors to clothing, targeting each vital sign, it can track the overall well-being of an individual. This would allow 24/7 monitoring as these devices are not cumbersome or obtrusive, providing comfortable wearability [1]. This also does not require the individual to be in a hospital environment as it can sense the signals and send the data wirelessly to a doctor to monitor and record the progress. This would be helpful to identify chronic conditions early, without waiting for scheduled checkups. However, an electronic device fabrication typically uses components generally made of hard materials such as solid pieces of metals (Cu, W, Al etc.) and semiconductors (Si, Ge). Integrating these hardware devices directly with fabrics would require planarizing the fabric surface to glue the device on top essentially. This process takes away the feel of the fabric, the comfort of the user to wear it and adds the inconvenience of removing/encapsulating the device for its washability. These issues can be addressed by switching to materials that would preserve the feel of the fabric such as solution-processed devices [2], [3].

A major issue and a gap in the advancement of wearable electronics is replacing the batteries needed for power. The battery provides an uninterrupted DC power supply to the device, but the hard and heavy nature and short life span that requires frequent replacements, make the integration to fabrics difficult. Since the device is for wearable purposes, it would be best suited if the mechanical energy produced by the various motions of the human body could be harvested to be the power source. It would also eliminate the dependency on environmental factors, such as solar and heat energy for photovoltaic and thermoelectric devices. The human body is able to produce up to 67 W from different body movements such as walking, running, bending etc., whereas common electronic devices such as sensors, smartwatches to tablets only require power ranging from micro, milli upto a Watt respectively [4]. This biomechanical energy from the human body can be converted to electrical energy with the help of the triboelectric effect.

The triboelectric effect is a common phenomenon resulting from friction between materials of different dielectric constants. When two such materials are in contact, one being more electropositive than the other, will lose electrons/ions/material transfer to the other in the process of charge exchange between the materials [5],[6]. By adding an electrode on the non-contacting side of these materials, it is possible to collect this charge by means of electrostatic induction, such a device is called a triboelectric nanogenerator (TENG). Their working mechanism, structures and mode of operations are discussed in detail in Section 2.3 of this thesis and further theoretical studies insights into the contact electrification process of these devices can be found here [7],[8],[9]. A roadmap of development and applications of TENG devices as micro/nano power sources, self-powered sensors, blue energy (water) applications and high voltage (HV) power source [10] are shown in Figure 1.1. This shows the need for a flexible, accurate and efficient design of good power management to integrate these devices into energy harvesting and self-powered sectors including wearable electronics.

TENG is a great source of energy as the triboelectric effect is an unavoidable occurrence in daily life. Since we are looking at harvesting biomechanical energy from human motions, vibration energy harvesting will be the focus from here on. By placing TENG devices at locations of the body prone to more movements such as knees, feet, underarms etc., would provide the external force for the tribolayers of the TENG to come in contact to produce an electrical output. The electrical response of TENG devices is commonly discussed in their voltage, current, charge and power outputs. Figure 1.2 below shows the first ever TENG device reported by Wang et al. in 2012 [11]. Polyethylene terephthalate (PET) and Kapton materials were used as tribolayers with gold electrodes. This structure produced an electric response of up to 3.3 V and 0.6 μA, with a peak output power of around 10.4 mW/cm^3 from the bending and releasing motion. This shows the ability of the TENG device to convert

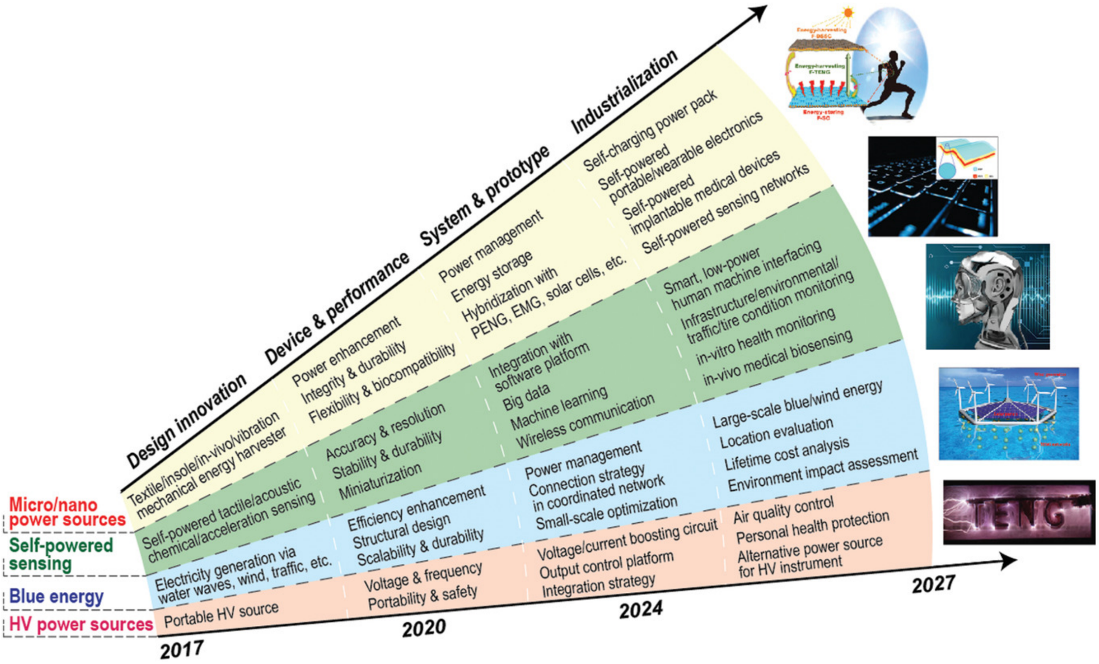

Figure 1.1: Roadmap of the progress and applications of TENG devices from their design to industrialisation in micro/nano power sources, self-powered sensors, blue energy and high voltage (HV) applications. Reproduced from [10].

irregular low-frequency mechanical energy from human motions to electrical energy.

The TENG device structure needs to be simple, flexible, lightweight, durable and shape adaptive to function efficiently as a user-friendly wearable device. In order to maintain wearability, they also need to preserve the feel of the textile fabric along with its air permeability which would be lacking in rigid plastic-based TENGs. Owing to the convenience of fabrication and integration steps, this work will focus on fabric-based TENGs instead of fibre/yarn-based ones. Within fabrics, they can be employed as substrates, electrodes, and triboelectric layers of TENG devices, which can be employed at various positions of the human body such as arm, waist, wrist, foot, fingers, knee, chest etc. to harvest from different types of mechanical motions.

TENGs generally produce low power output due to their highly resistive nature. Even though the voltage output is usually high in the hundreds, the current ranges generally in the micro to maximum milliampere range, so, they are often used in sensors as they require low power to function. For sensors made out of TENG devices, they can also be self-powered, which is useful in situations where carrying a heavy and bulky power source might not be an option, such as emergency response and military. These sensors can be used

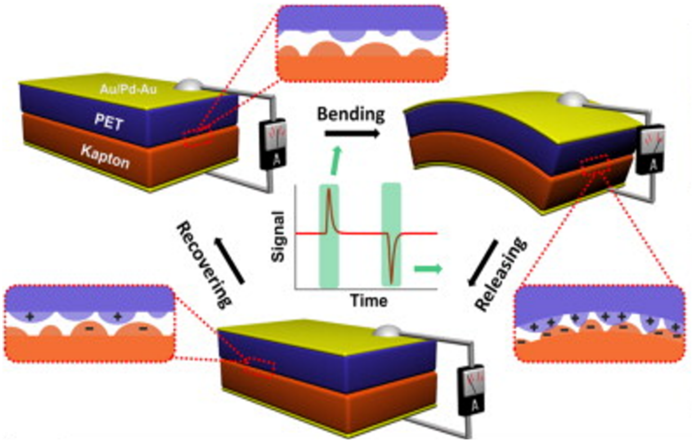

Figure 1.2: First TENG device demonstrated based on bending and releasing between PET and Kapton tribolayers. Reproduced from[11].

to monitor a soldier's or firefighter's health and fitness in emergency situations. TENGs are already demonstrated as sensors of pressure [12], acoustic [13], touch [14], motion [15] etc. They have recently been proposed towards human-machine interface where network security and information communication are explored [16], [17]. Studies and capabilities of TENGs made based on fibre/yarn [18] and fabrics [19], [20] are explored heavily for their potential applications [21]. Figure 1.3 shows the overview of applications studied for textile-based TENGs in sectors of energy harvesting, self-powered microsystems, actuators and sensors [22]. A wide range of materials are studied for their triboelectric behaviour including common ones such as nylon, polytetrafluoroethylene (PTFE), PET, polydimethylsiloxane (PDMS) etc.

It is not just tribolayers that need to be flexible and of 2D nature, electrodes used in the TENG devices also need to be wearable in nature. This requires a conductive, flexible and two-dimensional alternative material that can be integrated into fabrics instead of traditional hard metal electrodes.

The introduction of graphene into wearable TENGs helps the textile keep its 2D seamless wearable nature without compromising the device output owing to graphene's excellent electrical and mechanical properties. But different types of graphene can be used here from chemical vapour deposition (CVD) graphene to reduced graphene oxides (rGO) as detailed in Section 2.2.2 of this thesis. The choice of graphene affects the output and cost of the device due to the difference in the quality of graphene, cost of production and transfer/integration of graphene onto textiles. Even though CVD graphene shows

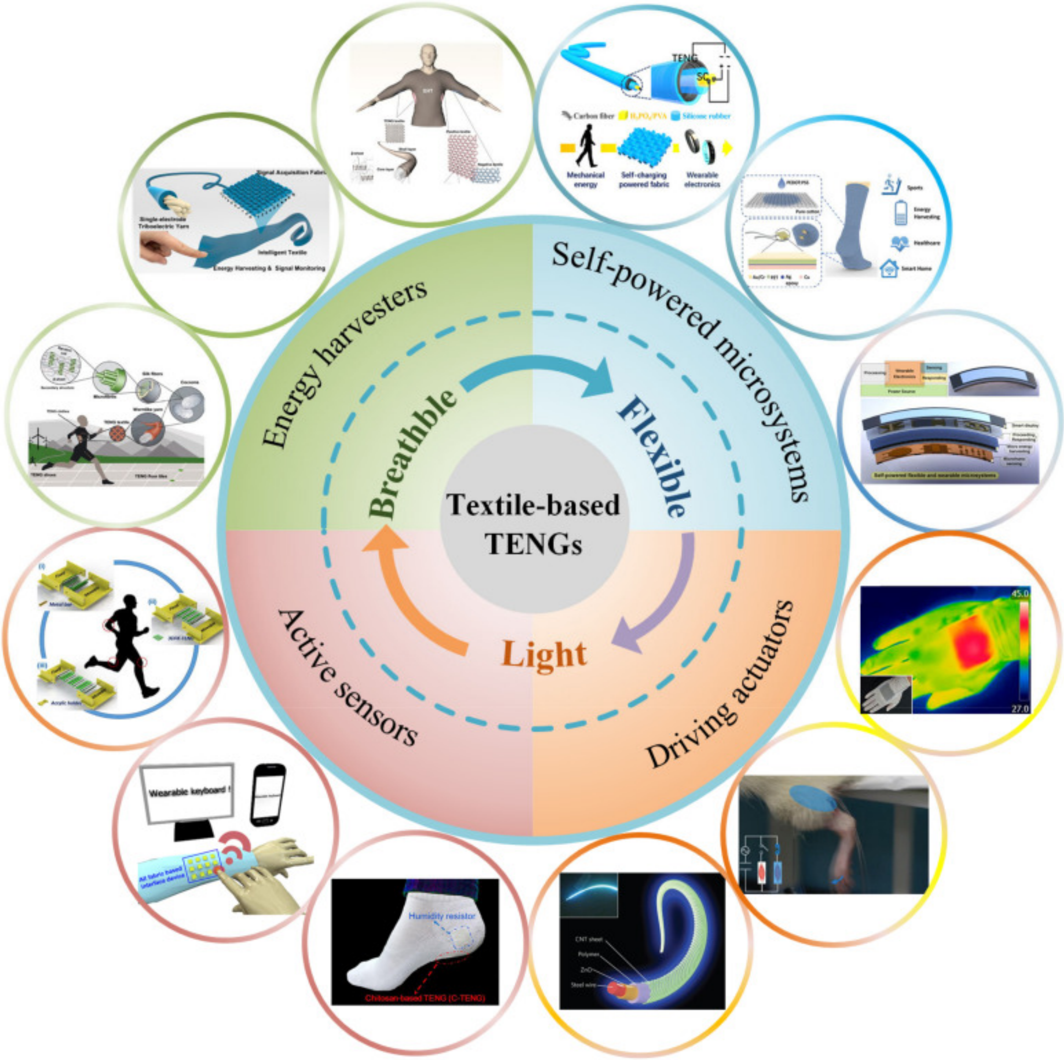

Figure 1.3: Overview of applications studied for textile-based TENGs in energy harvesting, self-powered microsystems, actuators and active sensors. Reproduced from [22].

a much higher quality with better properties, it is harder to produce large areas and quantities of few or single-layer graphene. They are made at a high temperature of 1000°C and the process requires high-purity metal substrates to grow the graphene, adding to the cost. Also, it is easier to integrate them onto individual fibres [23] than to textured fabric surfaces. For fabric surfaces, few to multi-layer graphene flakes (FLG, MLG) can follow their surface roughness better. It also has a lower cost of production for mass production. Simple and scalable transfer steps such as dip coating [24], pad-dry coating [25], spray coating [26] etc. can be followed to produce larger area coatings on fabrics. For example, porous reduced graphene oxide (rGO) is shown to work as an electrode as well as tribopositive layer against test material PTFE (polytetrafluroethylene) with an aluminium electrode to obtain an output of 81.5 V, 3.9 μA at an operating frequency of 4 Hz and an applied pressure of 256 kPa [27]. A conductive paste made of graphene, coated on nylon fabric is also studied as an electrode with blade-coated PDMS tribolayer on top to generate 213.75 V and 3.11 μA at 3 Hz and 5.6 kPa against human skin [28]. This indicates graphene would be a good addition to producing a high-performance wearable TENG device. Even though graphene is explored in TENGs as electrodes and tribolayers [29], in this work, it will be studied as a part of the textile electrode.

The aim of this thesis is to fabricate textile-based graphene electrodes compatible with wearable electronic devices and textile-based TENG devices for energy harvesting and self-powered sensing applications. Therefore it is structured into 7 chapters to discuss the background of the work, fabrication and characterisation studies of the electrode and TENG devices and applications and future directions of this work.

In Chapter 2, the theory and background required to understand and analyse the work discussed in this thesis are explained. This includes the theory behind all the methods followed for fabrication, techniques and tools used for their characterisation and scientific terms and parameters used to describe and analyse the results.

In Chapter 3, materials and experimental techniques used for the fabrication of textile electrodes and TENGs such as liquid phase exfoliation, ultrasonic spray coating etc. are discussed. This includes step-by-step details into each method of how samples are fabricated with these techniques and prepared for different characterisation techniques.

In Chapter 4, few-layer graphene and graphene nanoplatelets coated fabrics are studied in detail. Different methods followed for graphene coating on fabrics, their surface morphology, conductivity, thickness, mechanical properties etc. are studied for their application as a textile-based electrode.

In Chapter 5, TENG devices made out of textile-based electrodes are characterised. They are studied at various parameters such as frequency, separation distance, contact area, contact force, chemical modifications etc. to understand their effect on the TENG output. They are also exposed to various ambient conditions of humidity, air ionisation and mechanical strength tests to study their stability response.

In Chapter 6, the ability of TENG devices to function as a power source for low-power electronics is demonstrated with the help of LED and OLED devices. They are also studied as self-powered pressure sensors. Potential applications of both GNPs coating and TENG devices are also explored.

In Chapter 7, a summary of the work discussed in this thesis is provided.

Chapter 2

Theory & background

2.1 Introduction

In this chapter, the theory behind the materials used and the methods followed in this work are explained. The first part of this chapter includes the fabrication procedures followed for the production and coating of graphene on fabric substrates and in the second part, different techniques used for characterising these fabric-based textile electrodes and triboelectric nanogenerator (TENG) devices made from them are discussed in detail.

2.2 Graphene

2.2.1 Introduction

Graphene is a two-dimensional hexagonal honeycomb structure made of purely carbon atoms (shown in Figure 2.1) and it is the building block of commonly known and used material graphite. This one-atom-thick material was isolated in 2004, even though it was theoretically known from the 1940s. Exceptional electronic properties of graphene were already predicted at that time, but it was believed to be thermally unstable for it to exist. Much later, studies were reported on discovering related materials such as fullerenes (1985) and carbon nanotubes (1991) which again shifted the attention to producing monolayer graphene. Andre Geim and Konstantin Novoselov from Manchester used a simple scotch tape method on graphite where the sticky tape was repeatedly applied and peeled off till a single layer of graphene was left on the tape. This was confirmed by transferring onto a SiO_2 substrate and studying under an optical microscope [30].

Carbon atoms in graphene are sp^2 hybridised. The structure of single-layer graphene gives rise to its exceptional properties such as tensile strength (130 GPa), thermal conductivity (upto 5.3×10^3 $W.m^{-1}.K^{-1}$), electron mobility ($>$ 200,000 $cm^2.V^{-1}.s^{-1}$) [31] and uniform light absorption of 2.3% across the visible and IR range. These properties are explored in high-frequency electronics, energy harvesting and storage, sensing applications etc. in order to modify the performance of current devices. Mass producing high-quality graphene is still a challenge, so based on the applications, there are different types of graphene products from single layer to multilayer graphene and each, based on the method of production, will vary in quality, generally noted as the grade of graphene.

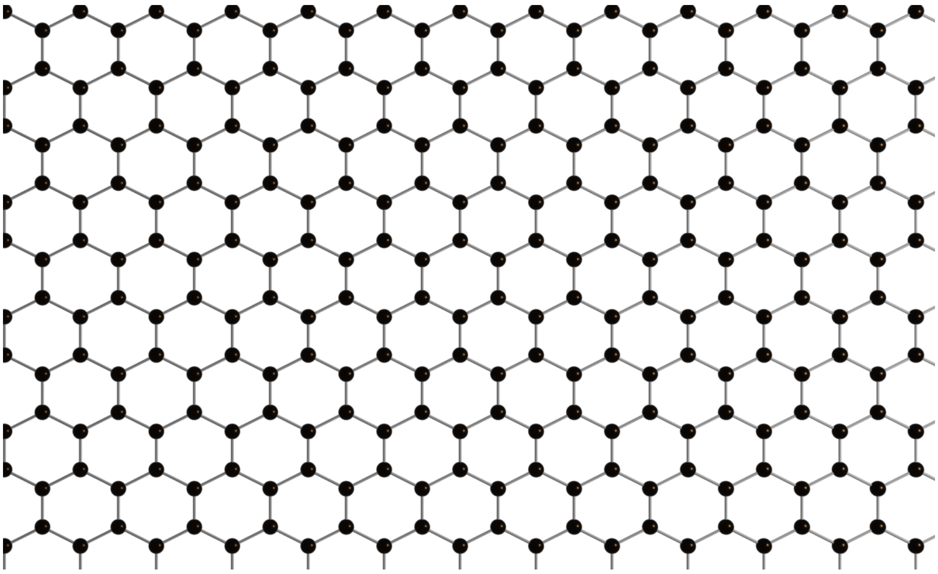

Figure 2.1: Hexagonal honeycomb structure of monolayer graphene. Carbon atoms are shown as solid circles and bonds between the atoms are shown as line segments connecting the solid circles.

Based on the number of layers or thickness of graphene layers stacked, they can be broadly divided into single layer, bilayer, few layer (3 to 10 layers) and multilayer ($>$ 10 layers) graphene. Graphene layers stacked are held together by weak van der Waals force arising from the overlap of partially filled π orbitals of each planar layer. They are spaced by 3.34 Å. The in-plane bonds present in graphene are much stronger with a lattice spacing of 1.4 Å.

2.2.2 Production of graphene

Depending on the quality and quantity of graphene required, different approaches have been followed for its production. These methods produce single-layer, few-layer to multilayer graphene and they could be of crystalline, polycrystalline, or flake structures with defects arising from their method of production. In this thesis, the term graphene would be used in general to refer to all these types of graphene and their specific details/types would be mentioned separately where they are used. Figure 2.2 below shows the main methods followed for the production of graphene including mechanical exfoliation, liquid phase exfoliation and chemical vapour deposition. This shows the quality of graphene produced against the cost for large-scale production, i.e industrial scalability of the method. A detailed study on a wide range of graphene production methods can be found here [32],[33]. Based on the type of production, all methods can be generally categorised into top-down (from bulk graphite, exfoliating it down to one or a few layers of graphene) and bottom-up (almost atom-by-atom to assemble the honeycomb lattice in a controllable number of layers as well) approaches [32].

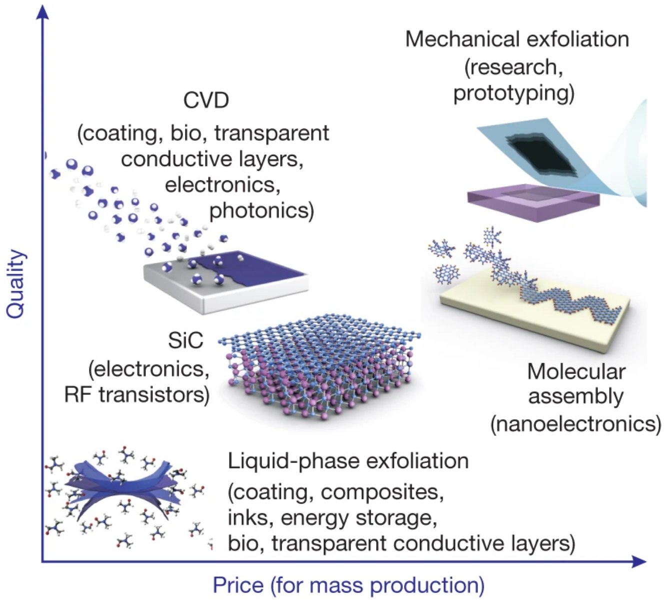

Figure 2.2: Shows general methods of fabrication used for graphene with their quality against the cost for mass production. Reproduced from [34].

For top-down approaches starting from graphite, and though different methods, they are much more efficient than the pioneer micro-mechanical exfoliation and can be shaved down to smaller and smaller numbers of layers, including single-layer graphene. These methods require a source of energy in the form of mechanical, chemical, etc. to break the van der Waals bonds between the layers of graphite. Increasing the distance between the layers with chemical functionalisation of graphite (e.g. oxidation of graphite) makes it easier to break those bonds and exfoliate, but at the expense of the defects and remaining oxygen-containing groups when reduced back to graphene (hence the term reduced graphene oxide).

In the case of the bottom-up approach graphene is synthesised from smaller components, such as with molecular assembly or CVD, using a source of carbon and high energy. Thermal energy is used for CVD, with methane or another carbon source and a catalyst, grown on copper or nickel substrates. In between the top-down and bottom-up approach (but often considered bottom-up) is epitaxial growth in SiC, where Si is thermally removed, leaving only C behind.

Bottom up

Chemical vapour deposition

CVD is a bottom-up approach to producing single and few-layer graphene. Carbon precursor in the vapour phase (eg. CH_4 gas) is introduced to a high-temperature reaction chamber along with H_2 gas. The precursor gas is then catalytically decomposed to be adsorbed onto a highly pure transition metal substrate (eg. Cu, Ni) placed in the chamber. This method produces relatively high-quality graphene [35]. The main drawbacks of this process come from the transfer methods required to isolate the single or few-layer graphene from the metal substrate and the energy cost for high-temperature production.

Molecular assembly

This method of graphene production is able to produce polycrystalline graphitic to graphene structures on Si substrate [36]. This greatly benefits electronic applications as graphene is directly grown on this conventional substrate of choice, avoiding graphene transfer procedures.

Epitaxial growth on SiC

Here, the silicon carbide (SiC) semiconductor is used as the substrate to grow few-layer graphene. At a high temperature of $> 1000°C$ and ultra-high vacuum, silicon desorbs from the surface of SiC crystal, leaving carbon atoms behind to form graphene/graphitic structures [37]. This is useful in applications involving high-frequency electronics, LEDs etc. as SiC is already the preferred substrate for these applications. Drawbacks to this method of production mainly come from the cost of SiC substrate, synthesis conditions, transfer methods and limitations to large-scale production.

Top-down

Micromechanical cleavage

Mechanical exfoliation of highly organised pyrolytic graphite (HOPG) produces high-quality graphene. The in-plane sigma bonds of graphene are much stronger than the van der Waals force present between the stacked graphene layers of graphite. This helps to keep the planar layers intact during the mechanical cleavage force to separate/ delaminate the stacked layers to reveal few-layer to single-layer graphene. This is best suited for studies regarding the properties of single-layer graphene as they are difficult to mass produce for applications that require higher quantities of graphene. Details of this method of graphene production can be found here [38].

Reduced Graphene Oxide

Reduced graphene oxides are generally produced by the Hummers and modified Hummers methods. Hummers method consists of oxidising graphite with strong oxidising agents such as sulphuric acid, sodium nitrate or potassium permanganate to form graphite oxide while in the modified hummers method, graphite oxide is produced at room temperature without using sodium nitrate. This graphite oxide compound has a higher interlayer distance compared to graphite structure due to the intercalation of oxygen groups from the oxidation process. This is followed by a reduction process to obtain a graphene-like structure, called reduced graphene oxide (rGO). For this, graphite or graphene oxide goes through chemical (hydrazine, L-ascorbic acid, sodium borohydride) or thermal reduction and a final step of base washing (NaOH) to remove further oxygen content present. Even though some of its electrical conductivity is restored, rGO still has residual oxygen groups along with other atoms and structural defects. This produces graphene-like material and is mostly used in applications requiring larger quantities of graphene such as fillers, composite materials etc.[39].

2.2.3 Liquid phase exfoliation

For industrial-level applications of graphene such as screen printing, composites etc. production methods used need to be scalable and cost-effective. The top-down method of liquid phase exfoliation of graphite suits mass production of few-layer to monolayer graphene without requiring high temperature and vacuum conditions such as CVD. In general, this is done by either ultrasonication or shear mixing. The sonication process makes use of ultrasonic waves to create regions of high and low pressure while propagating through the graphite suspension. This creates microcavities in the suspension which expand with each cycle reaching an unstable state, resulting in an implosion of the cavity, releasing shock waves through the suspension. This delaminates the graphene layers producing few to monolayer graphene as the interaction between solvent and graphene balances the energy needed for the exfoliation [40]. For this surface energy of the solvent needs to match that of graphene. But sonication as an energy source is a limitation in the cost-effectiveness of this method.

High shear mixing creates shear forces in the suspension to exfoliate graphite to few-layer down to monolayer graphene. They are generally used for dispersing agglomerates of nanoparticles which are bound by weaker forces. So in order to exfoliate graphite, they have to be either intercalated to weaken the inter-layer bond further or needs to be exfoliated in the right solvent. For the latter, the solvent used should be able to provide a stronger solvent-to-graphene interaction compared to graphene-to-graphene to prevent the layers from reaggregating due to their high surface energy. Organic solvents fit well for this method, but they are expensive and are generally toxic in nature. A greener option would be to use water as the solvent. But graphite and graphene layers are hydrophobic in nature, preventing a dispersion in water. Water also has a high surface tension reducing any interaction with the graphite/graphene material. This can be overcome by adding a surfactant that would reduce the surface tension and help suspend the exfoliated graphene layers in water, preventing their aggregation.

Here a rotor-stator mixer is used for high-shear mixing to both exfoliate graphite as well as dispersing graphene nanoplatelets to produce a homogeneous suspension. An example is the Silverson L5M high shear mixer used in this work, shown in Figure 2.3. The mixer head consists of stator housing with a rotor head inside at around 100 μm narrow gap. The high-speed rotation set to the rotor creates an upward suction like a pump, bringing the materials from the bottom into the mixer head. Centrifugal force pushes the particles into the ends of the mixer where it gets exfoliated between the rotor blades and inner wall of the stator owing to the shear force present, pushing the exfoliated layers through the perforations on the stator, back into the suspension. This technique is able to produce graphene flakes that are unoxidised with no defects to its basal plane [41]. By varying rotation speed, time of mixing, the diameter of the mixer head, the volume of solvent and the initial concentration of graphite, the concentration of graphene in the resulting suspension can be scaled up accordingly.

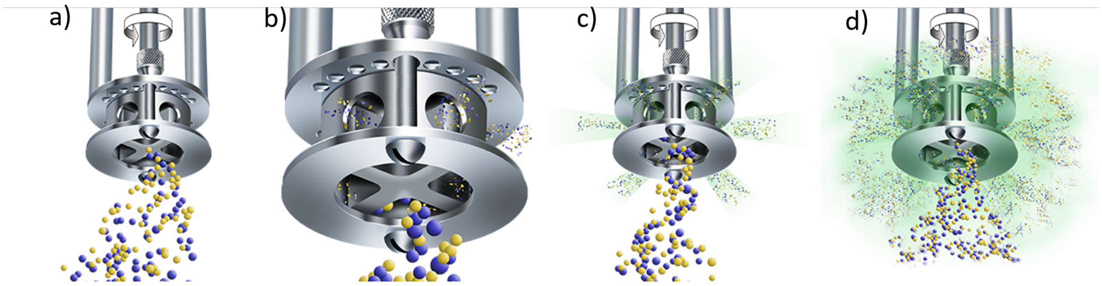

Figure 2.3: Different stages of working of Silverson L5M high shear mixer: a) material going into the mixer head due to suction created by high-speed rotor; b), c) and d) show the successive milling, exfoliation and expulsion of materials out into the suspension passing between the rotor blades and inner wall of the stator chamber. Reproduced from the Silverson website.

Since this method of production is able to produce reasonable quality graphene flakes at high quantities in a cost-effective manner, the liquid phase exfoliation process is chosen as one of the methods for graphene synthesis in this work. The shear mixer is used here for both exfoliations of graphite to produce FLG suspension as well as homogeneous dispersion of commercially available graphene nanoplatelets.

2.2.4 Graphene nanoplatelets (GNPs)

GNPs are a few nm thick layers of stacked graphene layers of platelet shapes. They exhibit a good range of electrical and thermal conductivity due to their graphitic form and are generally used as fillers in composites and inks to improve their properties [42]. GNPs are widely produced by chemical exfoliation and dry exfoliation with plasma among other exfoliation methods. The quality of the GNPs depends on the chosen production method. Here we have used industrial-grade GNPs produced chemically. They have an average thickness of 8-15 nm comprising 10 to 12 atomic layers. Nanoplatelets have an average diameter of 2 μm in x & y dimension with a surface area of 600 to 750 m^2/g and 2.1 g/cm^3 density at 20 °C. Figure 2.4 shows a transmission electron microscope (TEM) image of the nanoplatelets.

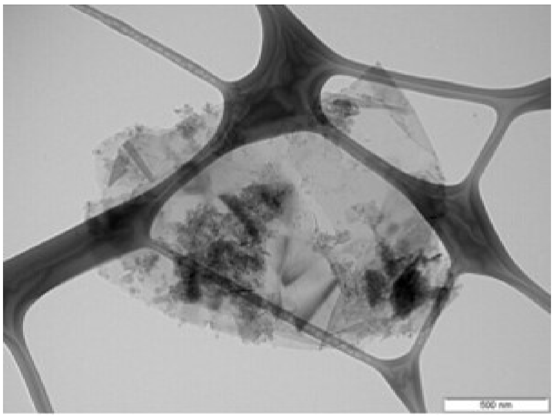

Figure 2.4: TEM image of graphene nanoplatelets purchased. The white scale bar corresponds to 0.5 μm. Reproduced from the Cheap Tubes website.

2.2.5 Graphene coating methods

There are two types of graphene used in this work, FLG and GNP. Water-based suspensions of both types of graphene are used to produce graphene as a film coating on flexible and textile substrates for the wearable applications targeted in this work. Graphene films produced this way will always comprise of overlapping individual graphene flakes, single- or few-layers, that will arrange at the surface to form a conductive network. General methods followed for graphene coatings on textile substrates are dip and dry [43][24], spray coating [44], screen printing, inkjet printing [45], pad dry method [25], vacuum filtration [46] etc. In this work, a few of these methods are followed for both FLG and GNPs suspension (discussed in chapters 3 & 4) before opting for spray coating as the optimal method and GNPs suspension as the best choice for conductive coating

Spray coating of graphene

Ultrasonic spraying is an emerging technology to coat various substrates avoiding the waste of chemicals, extreme operating conditions and multi-step procedures of conventional coating methods. This method has been employed recently in the deposition of the light emitting layer of polymer LEDs [47], fabrication of fuel cell electrodes [48], organic solar cells [49] etc. An ultrasonic spray coater compared to regular pressure nozzles can produce precise and controlled spray to form a thin, uniform coating allowing repeatability. Figure 2.5a shows this comparison of pressure nozzle sprays compared to an ultrasonic nozzle where the latter provides a narrow droplet size distribution minimising the overspray. This translates to the ability of ultrasonic nozzles to provide thin and uniform coatings with reduced material consumption. The ultrasonic nozzle used to spray the liquid operates at a certain resonant frequency which would determine the median of the droplet size. The higher the frequency, the smaller the droplet size with a narrow droplet distribution (Figure 2.5b). In a normal pressure spray system, air pressure is utilised to force liquid out through a small orifice to form the spray causing a wide distribution in droplet size, affecting the uniformity of coating.

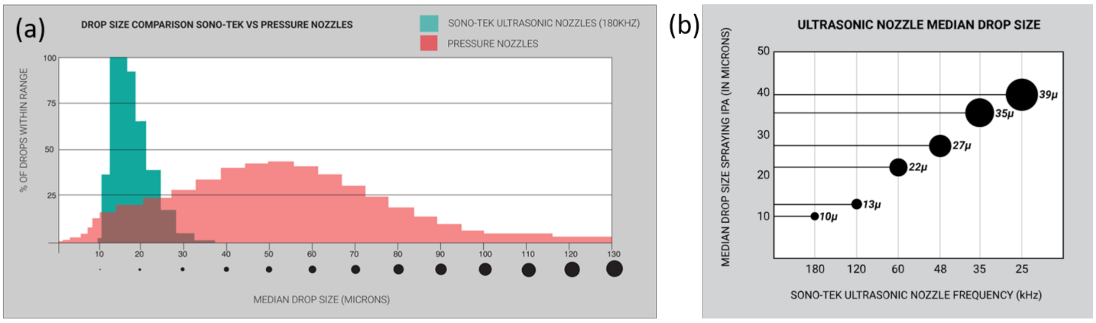

Figure 2.5: a) The droplet size distribution of regular pressure nozzle spray (red) compared to an ultrasonic nozzle spray (green). b) Dependency of droplet size on the frequency of ultrasonic nozzle, showing higher droplet size for lower frequency nozzles. Reproduced with permission from SONO-TEK website.

For the working of the ultrasonic nozzle, high-frequency sound waves are converted into mechanical energy to produce standing waves in the liquid, forming atomised spray at the nozzle orifice. The spray is then shaped and directed towards the substrate with the help of a low-velocity compressed air supply. The titanium alloy used for the construction of the nozzle head provides better acoustic properties along with good resistance to strong chemicals. Since the ultrasonic nozzle forms a low-velocity spray, it does not bounce off upon hitting the substrate, reducing the amount of over-spray and thus wastage. Different types of spray shaping systems are used depending on the application to produce fine lines, conical, wide flat fan shape sprays. Figure 2.6 shows the structure of a wide fan-shaped nozzle at different angles, demonstrating the nozzle's working. Piezoelectric crystals inside the nozzle undergo compression and expansion converting high-frequency sound waves to mechanical energy, which is transferred to the suspension inside the nozzle. This creates standing waves in the suspension and on reaching the tip of the nozzle, the waves acquire an amplitude large enough and the droplets detach from the tip, forming the spray. As shown in the figure, here the sprayed suspension is shaped and directed onto the substrate by a compressed air stream from a jet air deflector equipped above the nozzle. The ultrasonic vibration is also helpful in breaking down any aggregates formed in the suspension into individual particles.

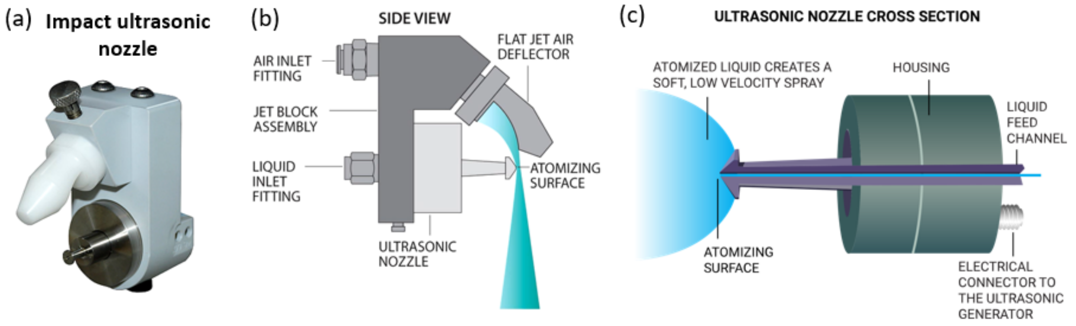

Figure 2.6: a) Structure of a wide fan-shaped impact ultrasonic nozzle and schematic diagrams of its b) side and c) cross-sectional view showing the components of the nozzle. Reproduced with permission from the SONO-TEK website.

2.3 Triboelectric nanogenerator

2.3.1 Introduction

The triboelectric effect is a contact electrification phenomenon. When two materials of different dielectric constants are in contact, due to differences in their electron affinities, the charge is transferred between them in the form of electrons / ions / materials transfer. Triboelectric nanogenerators (TENGs) are devices that produce electricity by combining this triboelectric effect with electrostatic induction [50]. This is done by adding two electrodes on the non-contact side of these dielectrics. When these dielectric materials in contact begin to separate from each other, the electrodes connected get charged due to electrostatic induction, which is collected through an external circuit. So the general structure of TENG devices consists of two dielectric materials (tribolayers) with electrodes on either side as shown in Figure 2.7.

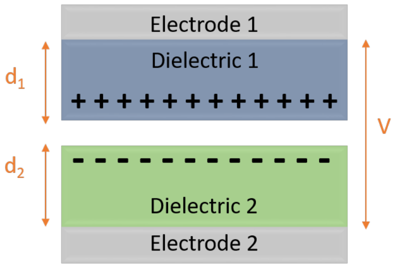

Figure 2.7: General structure of a dielectric-to-dielectric TENG showing the tribolayers (dielectric 1, dielectric 2) and their respective electrodes (electrode 1, electrode 2). The thickness of the dielectrics is marked as d_1, d_2 and the potential difference generated between the electrodes is labelled as V.

In TENGs with a general dielectric-to-dielectric structure, electrodes can be considered infinitely large as the area of electrodes is much larger than the separation between them. From Figure 2.7, the electric field between the electrodes is perpendicular to the surface and points from dielectric 1 to dielectric 2. The relative electrical permittivity of the dielectrics 1 and 2 are taken as ϵ_{r1} and ϵ_{r2} with their surface charge densities +σ and -σ. The size of the electrode area is noted as S and the charge induced on electrodes 1 and 2 as -Q and +Q. According to Gauss's theorem, The electric field inside the dielectric 1, E_1, inside the air gap E_{air} and inside dielectric 2, E_2 can be expressed as :

$$E_1 = \frac{-Q}{S\epsilon_0\epsilon_{r1}} \tag{2.3.1.1}$$

$$E_{air} = \frac{-Q}{S\epsilon_0} + \frac{\sigma(t)}{\epsilon_0} \tag{2.3.1.2}$$

$$E_2 = \frac{-Q}{S\epsilon_0\epsilon_{r2}} \tag{2.3.1.3}$$

So the total voltage between the two electrodes is given by :

$$V = E_1 d_1 + E_2 d_2 + E_{air} x \tag{2.3.1.4}$$

where d_1 and d_2 are the thickness of dielectrics 1 and 2 respectively and x is the air gap/separation distance between the dielectrics 1 and 2.

Substituting equations 2.1, 2.2 and 2.3 to equation 2.4,

$$V = \frac{-Qd_1}{S\epsilon_0\epsilon_{r1}} - \frac{Qd_2}{S\epsilon_0\epsilon_{r2}} - \frac{Qx}{S\epsilon_0} + \frac{\sigma(t)x}{\epsilon_0} \tag{2.3.1.5}$$

$$V = \frac{-Q}{S\epsilon_0}[\frac{d_1}{\epsilon_{r1}} + \frac{d_2}{\epsilon_{r2}} + x(t)] + \frac{\sigma x(t)}{\epsilon_0} \tag{2.3.1.6}$$

Equation 2.6 can be considered a general equation from which all the rest of the TENG operation modes and parameters can be derived. For example, this V-Q-x relation shows that the open circuit voltage is linearly proportional to the distance between the dielectrics, x.

Material choice for a TENG significantly affects the output produced as it is directly proportional to the difference in the electron affinity between the two tribolayers. The materials that are more electropositive will easily lose electrons to the more electronegative materials. Therefore it is useful to have a triboelectric series where various materials are listed in the order of their electron affinity with more electropositive ones at the top to the most electronegative ones at the bottom. Figure 2.8 shows such a triboelectric series with commonly tested materials including Teflon, Kapton, rubber, PET, cotton, silk etc.

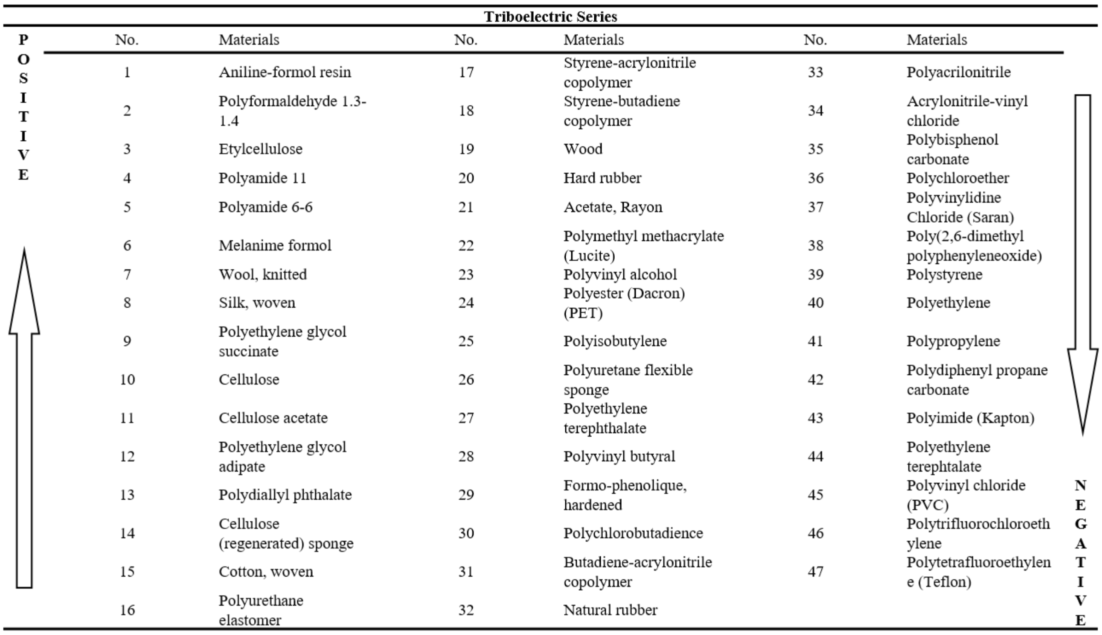

Triboelectric Series

No.	Materials	No.	Materials	No.	Materials
1	Aniline-formol resin	17	Styrene-acrylonitrile copolymer	33	Polyacrilonitrile
2	Polyformaldehyde 1.3-1.4	18	Styrene-butadiene copolymer	34	Acrylonitrile-vinyl chloride
3	Etylcellulose	19	Wood	35	Polybisphenol carbonate
4	Polyamide 11	20	Hard rubber	36	Polychloroether
5	Polyamide 6-6	21	Acetate, Rayon	37	Polyvinylidine Chloride (Saran)
6	Melanime formol	22	Polymethyl methacrylate (Lucite)	38	Poly(2,6-dimethyl polyphenyleneoxide)
7	Wool, knitted	23	Polyvinyl alcohol	39	Polystyrene
8	Silk, woven	24	Polyester (Dacron) (PET)	40	Polyethylene
9	Polyethylene glycol succinate	25	Polyisobutylene	41	Polypropylene
10	Cellulose	26	Polyuretane flexible sponge	42	Polydiphenyl propane carbonate
11	Cellulose acetate	27	Polyethylene terephthalate	43	Polyimide (Kapton)
12	Polyethylene glycol adipate	28	Polyvinyl butyral	44	Polyethylene terephtalate
13	Polydiallyl phthalate	29	Formo-phenolique, hardened	45	Polyvinyl chloride (PVC)
14	Cellulose (regenerated) sponge	30	Polychlorobutadience	46	Polytrifluorochloroethylene
15	Cotton, woven	31	Butadiene-acrylonitrile copolymer	47	Polytetrafluoroethylene (Teflon)
16	Polyurethane elastomer	32	Natural rubber		

Figure 2.8: Triboelectric series of some commonly used materials from most electropositive ones at the top to most electronegative materials at the bottom. Reproduced from [51].

2.3.2 Working principle

In this work, we use a vertical contact-separation mode (VCSM) triboelectric nanogenerator with two dissimilar dielectric materials facing each other with electrodes at the top and bottom of their stacked structure. Dielectrics can be selected from the different ends of the triboseries to enhance the triboelectric charge density produced. Electrical outputs obtained from the working of this TENGs are open circuit voltage (V_{oc}), short-circuit current (I_{sc}) and short-circuit charge (Q_{sc}) which are explained in the following sections with the help of their working mechanisms in schematic diagrams.

2.3.3 Structures

Vertical contact-separation mode

The vertical contact-separation mode of TENG is the most basic form of TENG operation. In this stacked structure, two dielectric tribo-layers face each other with their respective electrodes at the top and bottom of the structure as shown in Figure 2.9a. One set of electrode-dielectric part comes in periodic contact and separation perpendicular to the remaining part.

Lateral sliding mode

This mode of TENG is also a double electrode TENG much like the previous one, but instead of the vertical contact and separation perpendicular to the triboelectric surfaces, they are moved parallel to the surfaces, sliding laterally as shown in Figure 2.9b. This creates charge generation in the sliding direction, causing electrons to flow between the electrodes to balance the potential. Structures of this TENG can be planar like in Figure 2.9b, cylindrical, disc rotations etc.

Single-electrode mode

Single electrode TENG structure consists of one dielectric material coming in contact-separation perpendicularly against a ground electrode like in Figure 2.9c. It is suitable in scenarios where the dielectric material is part of a mobile object and thus can not be physically connected to a load. Here, the grounded layer would work as the tribomaterial and the electrode. The triboelectric charge produced during contact with the dielectric material would be balanced by the charge flow between the electrode material and the ground.

Freestanding triboelectric layer mode

This mode of operation is also more suited for moving objects as they would get charged from the friction against the other object or air. Two electrodes are spaced to fit the sliding motion of the dielectric material on top and the asymmetric charge generation from this lateral movement causes charge flow between these two connected electrodes. The structure of a freestanding triboelectric layer mode is shown in Figure 2.9d.

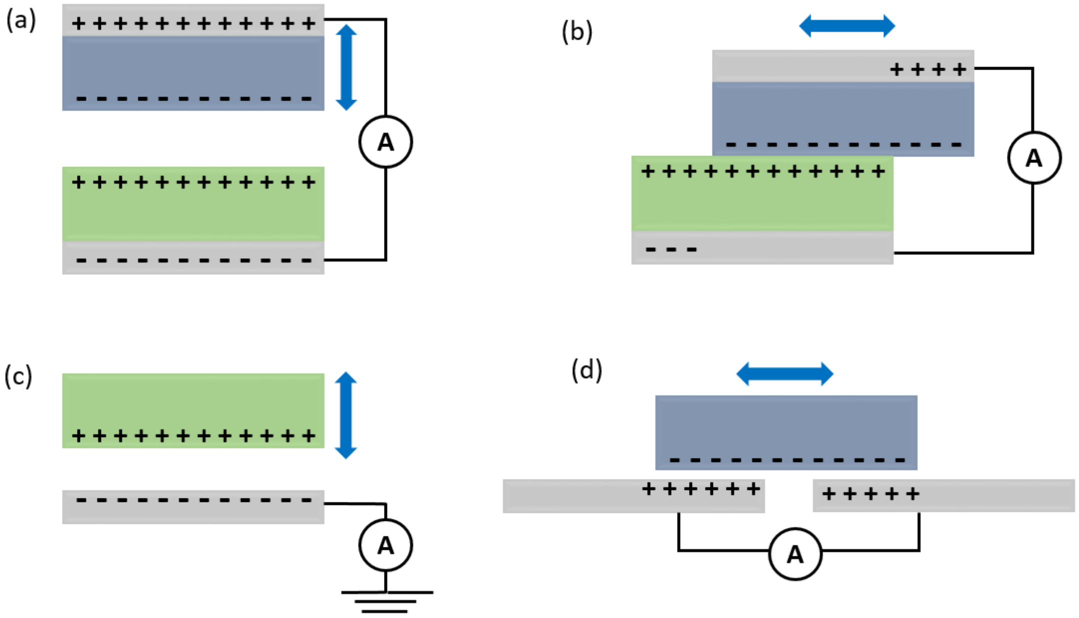

Figure 2.9: a) Vertical contact-separation mode, b) lateral sliding mode, c) single electrode mode, d) freestanding triboelectric layer mode.

2.3.4 TENG Outputs

Open circuit voltage

Figure 2.10 shows two dielectric materials (dielectric 1 and dielectric 2) with their top and bottom electrodes in the vertical contact-separation mode of TENG operation. When dielectrics 1 and 2 are in full contact (Figure 2.10a) triboelectric charges of opposite polarity are generated on each material depending on their ability to gain and lose electrons. In Figure 2.10a, dielectric 1 is negatively charged, gaining electrons from dielectric 2 which in turn is positively charged. As these two materials start to separate, these opposite charges are no longer in the same plane, creating a potential difference between them, which increases to reach a maximum value at a certain distance of separation (Figure 2.10c), beyond which the curve would remain a plateau unless followed by an immediate contact again. The open circuit voltage depends on the surface charge density and separation distance between the dielectrics.

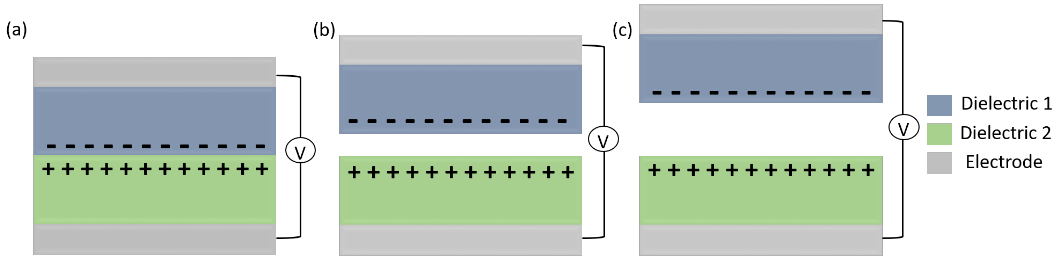

Figure 2.10: Schematic diagram showing generation of open circuit voltage in TENG characterisation. a) on contact between dielectric 1 and 2 opposite triboelectric charges are developed, b) dielectric 1 starts to move away from 2 developing an electric potential between the two, c) reaching a maximum value at a certain distance of separation.

The breakdown of a single peak of an open circuit voltage plot is shown below in Figure 2.11. As described before, voltage is produced at the separating and approaching stages of dielectrics, while there is no potential difference on full contact. On achieving the maximum distance of separation between the dielectrics, voltage is saturated as shown as a plateau in the plot. By repeating the cycle of contact and separation, several of such peaks can be recorded.

Short-circuit current

Here, both electrodes of the TENG are electrically connected to each other. As explained previously, charges are developed on the dielectric surfaces on contact between the two dielectric materials. But when the dielectrics are separated, the electric potential generated between them starts to get balanced by the electrodes by the flow of electrons between them as shown in Figure 2.12. Electrons flow from the top electrode connected to dielectric 1 to the bottom electrode with dielectric 2 until the charges are completely balanced at which point charge flow ends (Figure 2.12c). But when the dielectrics move to come back into contact, additional charges present in the bottom electrode flow back to the top electrode creating current in the opposite direction (Figure 2.12d)

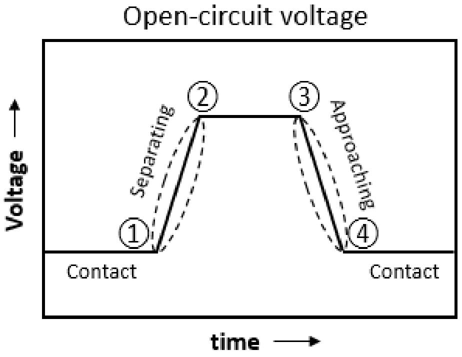

Figure 2.11: A single peak of open-circuit voltage from a single cycle of contact separation. Point 1 marks where the dielectrics in contact start separating, til it reaches a maximum value at 2 where it saturates forming a plateau. Voltage starts going down while the dielectrics begin approaching again, marked as 3, reaching zero on complete contact at 4.

until the dielectric surfaces are back into contact and the potential difference practically gets to zero. As it can be seen if the frequency of contact and separation cycles is increased, the flow rate of charge increases, enhancing the measured current output.

A breakdown of the short-circuit current plot from a single contact-separation cycle is shown in Figure 2.13. As discussed above, the process of approaching and separating produces current flow in the opposite direction, which can be seen from the plot, where the approaching part is in the negative and separation in the positive direction.

If the presence of dielectrics in this VCSM TENG structure is omitted, it is identical to a parallel plate capacitor with two metal plates facing each other holding -Q and +Q charge on each. If we consider the distance between the dielectrics as x, we can define the capacitance of this electrode capacitor structure as C(x) and the potential difference created is -Q/C(x) and the potential difference (V) within the VCSM TENG at any given distance x can be expressed as :

$$V = \frac{-Q}{C(x)} + V_{\mathrm{OC}}(x) \tag{2.3.4.1}$$

In short-circuit condition, Q = Q_{SC}, where potential created between the tribolayers is fully balanced by the induced charges on the electrodes, equation 2.3.4.1 simplifies to

$$0 = \frac{-Q_{\mathrm{SC}}(x)}{C(x)} + V_{\mathrm{OC}}(x) \tag{2.3.4.2}$$

$$Q_{\mathrm{SC}}(x) = C(x)V_{\mathrm{OC}}(x) \tag{2.3.4.3}$$

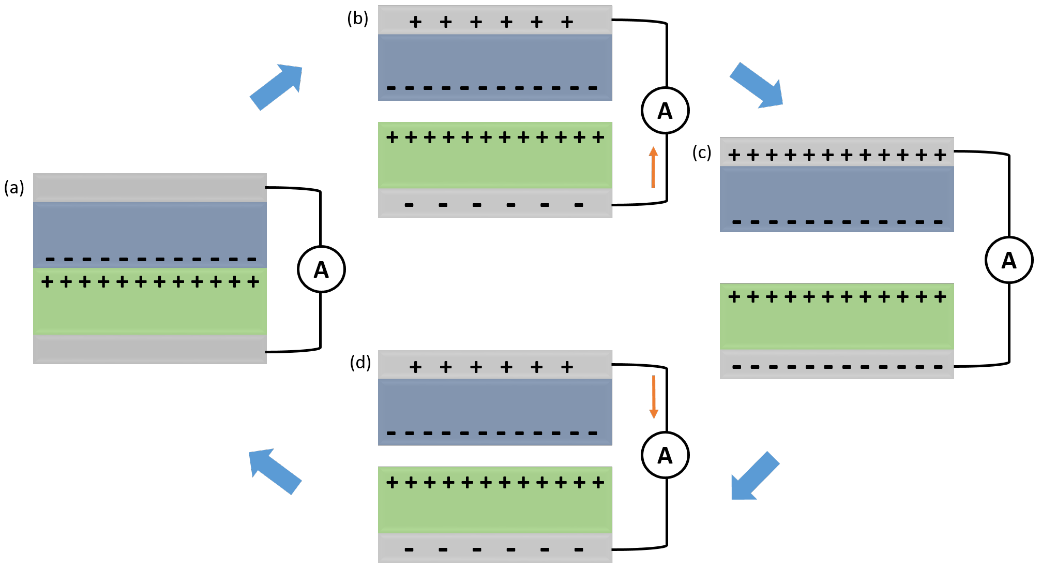

Figure 2.12: Schematic diagram of short-circuit current measurement in TENG characterisation. a) Triboelectric charges formed at the dielectric surfaces on contact, with dielectric 1 getting negatively charged and 2 getting positively charged, b) dielectric starts to separate from each other and their electrically connected electrodes start to flow electrons between them to obtain opposite polarity charges to their individual tribolayers. This is done to balance the potential created between the tribolayers and here current flow from the bottom electrode to the top. c) On reaching a certain value of separation distance, the potential between the tribolayers is completely balanced by the potential between electrodes and electron flow stops. d) When the dielectric begins to come back into contact, extra charges on the electrodes flow the other way, reaching zero potential.

connecting the short circuit charge Q_{SC} to the open circuit voltage V_{OC}. This inherent capacitive behaviour of TENG, with very low capacitance (in nF range) [52], results in high impedance of these devices (in MΩ range) and low power transmittance efficiency.

2.4 Experimental and characterisation tools for graphene and TENGs

2.4.1 Ultraviolet-ozone surface treatment of fabrics

The ultraviolet-ozone surface treatment makes use of a high-intensity, low-pressure, mercury vapour lamp to turn atmospheric oxygen into ozone molecules. These systems can be used for either cleaning the surface of a substrate of any organic contaminants or increasing the energy of the surface by attaching oxygen-containing functional groups.

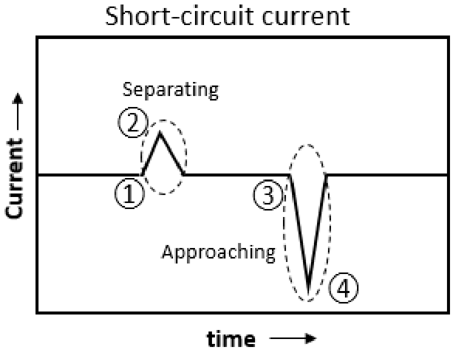

Figure 2.13: Short-circuit current plot of a TENG device showing the dielectric separation stage and approaching stage in the contact-separation mode of operation. Marker 1 corresponds to the point where the dielectrics start separating from each other from the previous contact position, reaching maximum separation distance at marker 2, where the current flow stops and goes to zero. When the dielectrics are approaching back again, current flow occurs in the opposite direction as shown from markers 3 to 4, falling back to zero once in contact.

The mercury vapour lamp has two high-intensity peaks in the ultra-violet region, at wavelengths 184 and 254 nm. Wavelengths under 200 nm can dissociate molecular oxygen into reactive oxygen radicals (Equation 2.4.1.1) which then react with another molecular oxygen to create an ozone molecule as shown in equation 2.4.1.2 below.

$$O_2 \xrightarrow{h\nu} O + O \tag{2.4.1.1}$$

$$O + O_2 \rightarrow O_3 \tag{2.4.1.2}$$

At a higher wavelength (254 nm) any organic species present on the surface can be excited, making them reactive towards ozone. In reaction with ozone, they are dissociated into smaller volatile molecules that will be carried away from the surface. It can also dissociate water molecules present in the atmosphere to hydroxyl groups and oxygen radicals (Equation 2.4.1.3). These hydroxyl groups, if present closer to the sample surface, can attach to the surface forming a hydroxyl functional group of high bonding energy on the surface, increasing the surface energy of the sample.

$$H_2O \rightarrow OH + O \tag{2.4.1.3}$$

2.4.2 Reactive ion etching

Reactive ion etching (RIE) is a dry etch process used to chemically or physically modify a material with the help of a chemically reactive plasma. The RIE system usually consists of a cylindrical steel chamber kept under low pressure and the process gas of choice is introduced from the top with a strong electromagnetic field of radio frequency. This causes the atoms/molecules to oscillate and break apart into electrons and corresponding ions. Ions, being heavier move slower than electrons, which collide with the walls of the cylinders and the electrically isolated metallic platter kept at the bottom of the cylinder. The electrons accumulated in the platter create a stronger negative potential for the ions to charge vertically downwards, which can cause both sputtering of material from the sample as well as chemical interaction with the plasma. This depends on the set parameters including RF power, pressure, gas flow rate, set time etc.

2.4.3 Contact angle goniometer

A goniometer is an instrument that can measure the contact angle made between a liquid droplet and a solid surface. In simple terms, it is a measure of the wettability of a substrate. For example, the shape of a water droplet on a surface can measure how hydrophobic or hydrophilic a surface is following various treatments (UV-Ozone surface treatment, polymer coating etc.) performed to tune the surface to the interaction required for the specific application.

Figure 2.14 shows a droplet of water on different types of substrates ranging from hydrophobic, hydrophilic to extremely hydrophilic substrates. A hydrophobic surface does not allow the droplet to wet the surface resulting in the spherical shape of the liquid on the surface as it is being repelled. However, a hydrophilic surface interacts with the droplet to spread on the surface resulting in a smaller contact angle while an extremely hydrophilic one immediately gets spread onto the surface.

The contact angle is quantitatively determined using the Young–Dupré equation (Equation 2.4.3.1). It states, at equilibrium the forces created by the surface tension between the interface of the three phases of solid(s), liquid(l) and gas(g) should balance each other. Surface tension is the force that tries to attain the minimum energy configuration for a liquid surface, higher surface tension

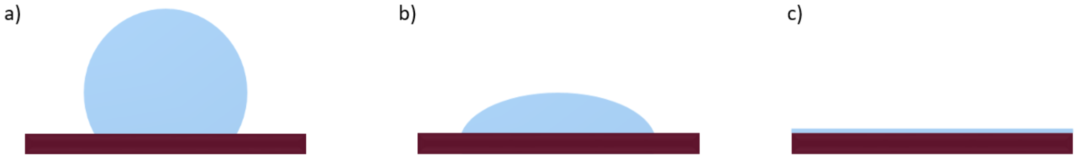

Figure 2.14: Shows the response of a water droplet on three different substrates of a)hydrophobic, b)hydrophilic and c) extremely hydrophilic nature.

leads to a spherical shape for the droplet thus lower surface energy. At the point where the liquid comes in contact with the solid, there are surface tension forces created between the liquid-solid (sl), liquid-gas (gl) and gas-solid (gs) interface as shown in Figure 2.15.

$$\gamma_{gs} = \gamma_{sl} + \gamma_{gl} cos(\theta) \tag{2.4.3.1}$$

i.e. :

$$cos(\theta) = \frac{\gamma_{gs} - \gamma_{sl}}{\gamma_{gl}} \tag{2.4.3.2}$$

From this equation it can be seen that the relation between γ_{gs} and γ_{sl} determines the contact angle between the surface and the liquid droplet.

$\gamma_{gs} < \gamma_{sl} \Rightarrow \theta > 90°$ i.e. liquid dewets the surface (in case of water, hydrophobic nature)

$\gamma_{gs} > \gamma_{sl} \Rightarrow \theta < 90°$ i.e. liquid wets the surface (in case of water, hydrophilic nature)

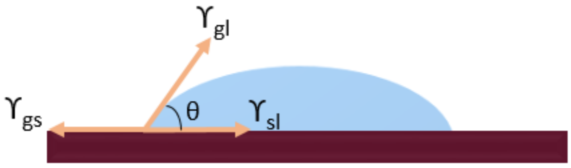

Figure 2.15: Three surface tension forces present between the gas-solid (gs), solid-liquid (sl) and gas-liquid (gl) interfaces at equilibrium.

2.4.4 Scanning electron microscopy

The ability of a microscope to distinguish between two very close points is called the resolving power or resolution of the microscope. It depends on the properties of the lenses as well as the wavelength of the illuminating beam used in the setup. So a high resolving power is required to view the features of the sample at much smaller nanometer scales. Since the wavelength of light limits the resolution of an optical microscope, smaller scales can be studied by shifting to electrons as their wavelength can be tuned to very small values.

In order to study the working of scanning electron microscopy (SEM), it is important to understand the concept of 'interaction volume'. Figure 2.16 shows the response of a sample to incoming radiation. The electrons interact with the surface and get scattered both elastically and in-elastically giving rise to different types of radiation, providing topography to the atomic constitution of the sample.

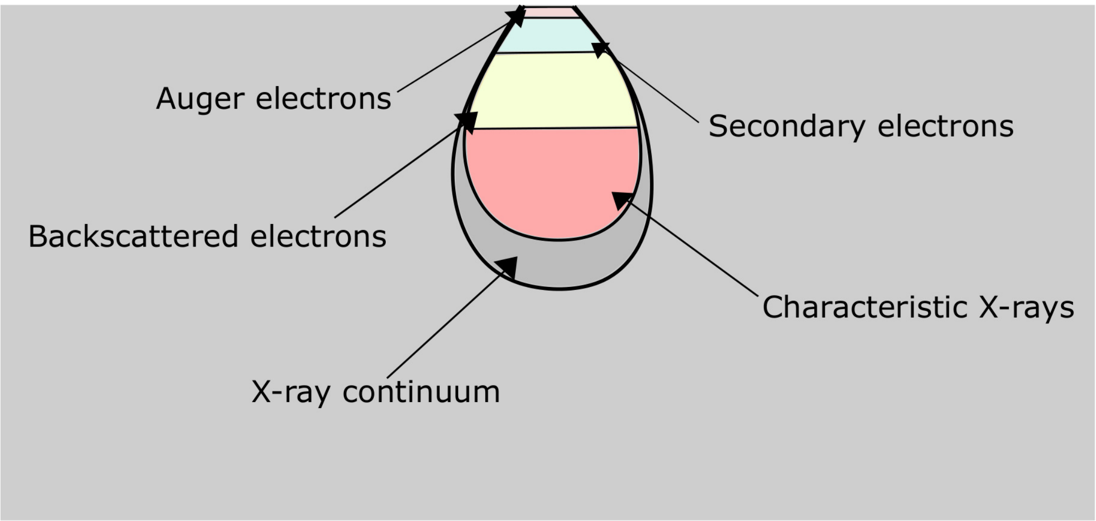

Figure 2.16: Schematic diagram of electron interaction volume showing types of radiation emitted from a sample surface in response to the incident electron beam. Electrons ejected close to the surface like secondary electrons are useful in surface topography while the emission of characteristic X-rays can be used to identify the elements present in the sample.

Electrons are released from a metal either by thermal or field emission and focused onto the sample with the help of electromagnetic lenses. These samples should be conductive, if not they must be coated with a thin conductive layer by sputtering. This is essential as the samples must be grounded to avoid the charge building up on the surface. The secondary electrons ejected from each point of the surface are mapped onto the surface topography at that point to generate the entire surface features of a sample. In order to get to the atomic composition of the sample, electron beams of higher energy are used to generate X-rays from the sample which are signature features of each element as each corresponds to the difference in energy levels of the inner orbits of an atom. This is generally called electron dispersive X-ray analysis (EDX).

2.4.5 Raman spectroscopy

Raman spectroscopy is a non-destructive technique used to study the chemical composition of a material through the inelastic interaction of light with its vibrational states. A monochromatic laser light is shone onto a sample, where it gets scattered both inelastically and elastically (Rayleigh scattering). The minute fraction of light that undergoes inelastic scattering can either lose (more commonly) or gain energy from the photons resulting in Stokes and anti-Stokes scattering respectively. These are filtered out to study the Raman effect. The change in the vibrational energy of molecules is then plotted as Raman shifts against the intensity of each peak (number of photons collected by the photodetector), providing a fingerprint match for identifying the composition of the material in terms of atoms and bonds present.

Raman spectroscopy is a powerful tool to study the properties of graphene [53], [54], [55]. In the case of graphite, there are 2 major peaks of Raman shifts obtained as shown in Figure 2.17 with a 514 nm laser. The G peak is generally observed at ca. 1600 cm^{-1}, corresponding to the in-plane vibrations of sp^2 C atoms. The 2D peak around 2700 cm^{-1} can give information about the stacking order. The 2D peak of graphite has a doublet structure, instead in few-layer graphene it has a multipeak structure differing from the sharp single peak present in graphene. A peak corresponding to any defects present such as vacancies, implanted atoms, sp^3 hybridisation or edge, grain boundaries in the scanned area is present at ca. 1350 cm^{-1}, and it is termed D peak. The Y axis of the Raman spectrum corresponds to the intensity of each peak and is expressed in arbitrary units as the value can vary based on the power of the laser applied. The area under the G peak, the ratio of intensities between 2D to G peak and D to G peak, full-width at half-maximum (FWHM) of 2D peak etc. are studied to obtain useful information such as the strength of Raman bands, number of graphene layers present, defect density etc. regarding the sample studied.

Since graphene samples typically do not have a uniform structure over a large area, it is useful to do a Raman mapping, instead of a single spot spectrum. This would provide details on local variation across the selected area, giving a better overview of the sample. The mapping of G peak and its shift in peak position indicates the presence of strain across the sp^2 structure and doping that can come from impurities introduced during the preparation/deposition method. The 2D peak mapping across the same area can help

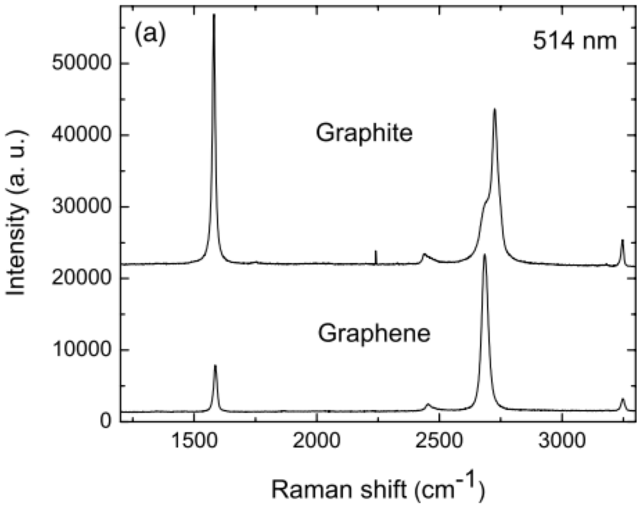

Figure 2.17: Raman spectra of graphite and graphene obtained with 514 nm laser showing the G peak at 1600 cm^{-1} corresponding to the amount of sp^2 C atoms and the 2D peak at 2700 cm^{-1} indicating the stacking order. Reproduced from [54].

distinguish between the strain and doping present.

2.4.6 van der Pauw method of Sheet resistance

Sheet resistance (R_s) is used to express the electrical resistance of thin films made of conductive and semi-conductive materials. It is the average resistance of a planar sample. It is expressed as resistance per square, i.e. the R_s is independent of the size of samples and can be compared easily between materials. Here van der Pauw method is used to calculate the sheet resistance [56]. This requires the measured sample to be isotropic, homogeneous of uniform thickness with no isolated holes. This method can generally be applied to any arbitrary shape that meets these requirements, but symmetric shapes can simplify these calculations. So they are usually made in square or clover shapes. From here onwards, only square-shaped samples are considered as it is the only shape followed in this work.

For sample preparation, contacts need to be placed at the periphery of the sample and the size of contacts should be significantly smaller than the distance between the contacts. Following this, Ohmic contacts can be placed at the four corners of the square shape as shown in Figure 2.18a. Corners are numbered from 1 to 4 in a counterclockwise direction as shown in Figure 2.18a. Then an electrical current is passed from corner 1 and taken out of corner 2, I_{12}, and the corresponding voltage is measured between 3 and 4, V_{34} (V_4 - V_3), shown in Figure 2.18b. Resistance, $R_{12,34}$ is then calculated by dividing V_{34} by I_{12}. Sides can be switched to obtain $R_{34,12}$, from reciprocity theorem, $R_{12,34} = R_{34,12}$. This value is then noted as horizontal resistance, R_h. Similarly, the vertical resistance value of R_v is calculated (Figure 2.18c). Van der Pauw proposed that these quantities are connected simply by equation 2.4.6.1 below,

$$e^{-\frac{R_h}{R_s}} + e^{-\frac{R_v}{R_s}} = 1 \tag{2.4.6.1}$$

Since the sample possesses a line of symmetry, in these cases $R_h = R_v$, noted as R. Then the equation is reduced to,

$$R_s = \frac{\pi R}{ln2} = 4.53R \tag{2.4.6.2}$$

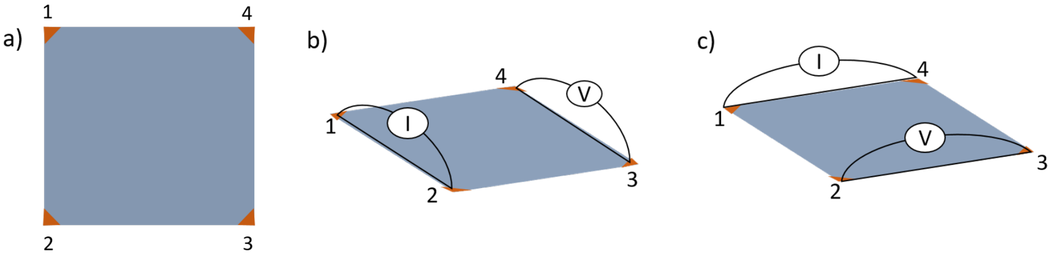

Figure 2.18: a) Schematic diagram of a square-shaped sample prepared with ohmic contacts at all four corners (copper colour); b) corners of the square are numbered from 1 to 4 counter-clockwise from the top left corner and current is applied between 1 to 2 while voltage response measured between 3 and 4 for vertical resistance R_v calculation; c) current applied from 1 to 4 and voltage sensed between 2 and 3 to calculate horizontal resistance R_h.

2.4.7 Tensile testing

The mechanical strength of materials can be tested by their response to controlled tension. For isotropic materials, uni-axial tensile testing can be adopted, where the sample is mounted between two cross heads and one of the heads can apply force to elongate the material along its length until it fractures. This process is generally expressed as a stress-strain curve. Stress is defined as

$$Stress(\sigma) = \frac{F}{A} \tag{2.4.7.1}$$

where F is the tensile force and A is the nominal cross-section area of the sample. Stress is expressed in units of N/m^2 or Pa. If we consider the initial length of the sample as L_0 and the final elongated length as L. The strain is defined as,

$$Strain(\epsilon) = \frac{L - L_0}{L_0} \tag{2.4.7.2}$$

Strain is a dimensionless quantity, measured in this thesis in mm/mm units. In general, stress-strain curves have (Figure 2.19) an elastic and a plastic region. In the beginning, where stress is proportional to the strain. The material can be brought back to its initial form, when stress is removed, in what is known as elastic deformation. The slope of this region is termed Young's modulus and the stress component of the endpoint is called the yield point. Beyond this point, the material goes through plastic deformation, passing through the ultimate tensile strength point of the highest stress value before reaching the breaking point. The stage between the ultimate tensile strength and breaking points is called necking as the cross-sectional area gets much smaller than the average and the heterogeneous nature of this process directs the stress to be concentrated on the smaller sections leading to the breaking of the material.

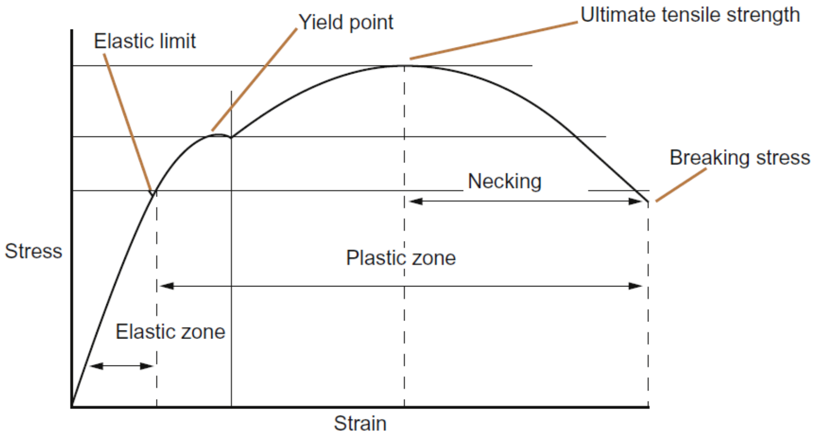

Figure 2.19: Stress vs strain curve showing the general parameters including elastic region, ultimate tensile strength and breaking point studied towards its mechanical strength. Reproduced from [57].

2.4.8 Non-contact surface profilometer

Surface topography can be quantified with the help of a physical probe (stylus) or using light (optical) to follow the roughness of the sample. Latter is a non-destructive tool as it does not come in contact with the sample's surface. The scans can be point, line or area based and either the sample stage or detector can be moved along the scan points. Light (eg: laser) from a source is directed towards the sample surface and the reflected rays are captured by a detector at each scanning point to recreate the surface morphology of the scanned area.

2.4.9 Spin coater

Spin coating is a method used to produce even thin films of a few nm to μm thickness. It is an easy and quick method and is much suited to produce coatings of controlled thickness for laboratory-scale fabrication. The solution containing the material to be spin coated is cast onto the substrate of choice which can be set to spin before the deposition of solution (dynamic spin coating) or after deposition (static spin coating). Rotations per minute (rpm) or rotations per second (rps) set for the spinning affect the thickness of the film formed as

$$t \propto \frac{1}{\sqrt{\omega}} \tag{2.4.9.1}$$

where t is the thickness of the spin-coated film and ω is the angular velocity corresponding to spin speed. They are inversely proportional to each other, i.e. the higher the rpm, the lower the film thickness.

2.4.10 TENG characterisation set-up

A custom set-up used to characterise the TENG device here is discussed in detail by Ishara et al. [7]. A motion controller is set up via Galil tool software to control the motion parameters of a voice coil (linear motor). A moving stage is connected to the voice coil and has a sample holder on the other end which can carry one side of the double-electrode TENG device. The amplitude, frequency and contact force of this moving stage can be controlled via the Galil tool. The opposite side of the TENG is mounted on a stationary sample holder connected to a load cell that can monitor the force applied upon contact between the two sides. Both metal sample holders are electrically isolated from the rest of the set-up with the help of thick nylon blocks. Two Keithley source meters are required, one monitoring the load cell and the other collecting the TENG outputs. GPIB cables are used to connect the Keithley to a computer and the outputs can be collected with Excelinx software. The working of this set-up is shown as a flow chart in Figure 2.20.

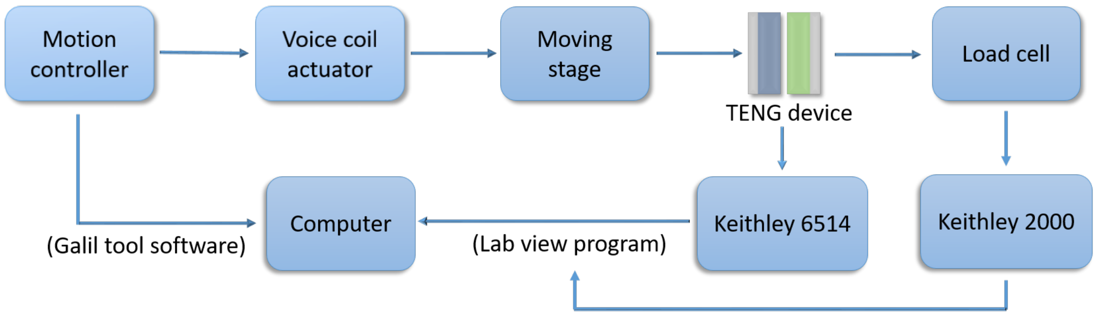

Figure 2.20: Shematic diagram of all components involved in TENG characterisation set-up. A motion controller is used to control a voice coil actuator. A moving stage with one part of a double electrode TENG is attached to the voice coil for its liner movement. The other half of the TENG remains stationary and a load cell is connected behind to monitor the contacting force applied by the moving part. Keithley source meters are used to monitor the contacting force and outputs of the TENG.

Chapter 3

Experimental methods

3.1 Introduction

This chapter discusses the experimental techniques used in fabricating and characterising textile electrodes and TENG devices made using these electrodes. The first part of this chapter talks about the fabrication procedures including preparation of graphene suspension, surface treatment of fabrics, graphene coating methods along with PDMS preparation and TENG fabrication. The second part of the chapter discusses characterisation tools used to study the surface topology, electrical conductivity and mechanical strength of these coated fabrics and the characterisation set-up used for TENGs developed with these textile electrodes.

3.2 Graphene coated textile electrodes

Fabrics provided by Heathcoat Ltd were used as substrates for electrode fabrication. Using a high-shear mixer, two types of graphene suspensions were prepared each from graphite flakes and graphene nanoplatelets (GNPs). Fabrics were treated with 5 minutes of UV-Ozone rays to raise their hydrophilic nature for better interaction with the water-based graphene suspension used to coat on top. Different methods were investigated to coat these graphene suspensions and it was concluded that the optimal method to fabricate wearable TENG devices is ultrasonic spray coating of GNPs.

3.2.1 Fabrics

Fabrics of polyester (M-09305-A01), nylon (G-60287-Q10) and meta-aramid (F-00910-Z01) studied and used as substrates in this work are provided by

Heathcoat Fabrics Ltd. Polyester fabrics used are 100% pure polyester material with 269 grams per square metre (gsm). Nylon fabric is described as 100% HT Nylon 6,6 of plain/calendered structure and 21 gsm. This fabric is very lightweight. Final meta-aramid fabric is a heat-resistant fabric. This is also 100% pure meta-aramid material but comes with a surface treatment described as primed and ready for adhesion. This fabric has a density of 110-140 gsm.

3.2.2 Preparation of few-layer graphene suspension

This few-layer graphene (FLG) suspension is produced from graphite flakes (shown in Figure 3.1a) based on the methodology described in [58]. 12 g of graphite flakes (purchased from Sigma Aldrich, 332461) were added to 800 ml of deionised (DI) water along with 4 g of NaC (Sigma Aldrich, C6445) as a surfactant. A high shear mixer (Silverson L5M) (Figure 3.1b) with a 32 mm diameter mixer head as shown in Figure 3.1c was used to exfoliate the graphite flakes in water at 4500 rpm for 60 minutes. These exfoliated flakes were suspended in water through the use of amphiphilic NaC molecules, preventing the exfoliated flakes from aggregating. Since this exfoliation process can lead to a wide distribution of flake thickness with a varying number of graphene layers, this exfoliated graphite suspension was allowed to stand overnight to settle heavier and unexfoliated flakes at the bottom to discard. The rest of the suspension was centrifuged at 1500 rpm for 100 minutes to discard further deposited flakes at the bottom. The supernatant was separated and used here as FLG suspension.

3.2.3 Preparation of graphene nanoplatelets suspension

Graphene nanoplatelets (GNPs, purchased from Cheap Tubes Inc) are ready to use in powder form as shown in Figure 3.2a. 1.4 g of these GNPs were weighed in a glass beaker and 800 ml of DI water was added. 32 mm diameter mixer head of Silverson L5M high shear mixer was then lowered into the beaker. The rotor component of the head as shown in Figure 3.1c was set to rotate at 5000 rpm for 120 minutes to produce a homogeneous GNPs suspension of 1.75 g/L concentration as shown in Figure 3.2b.

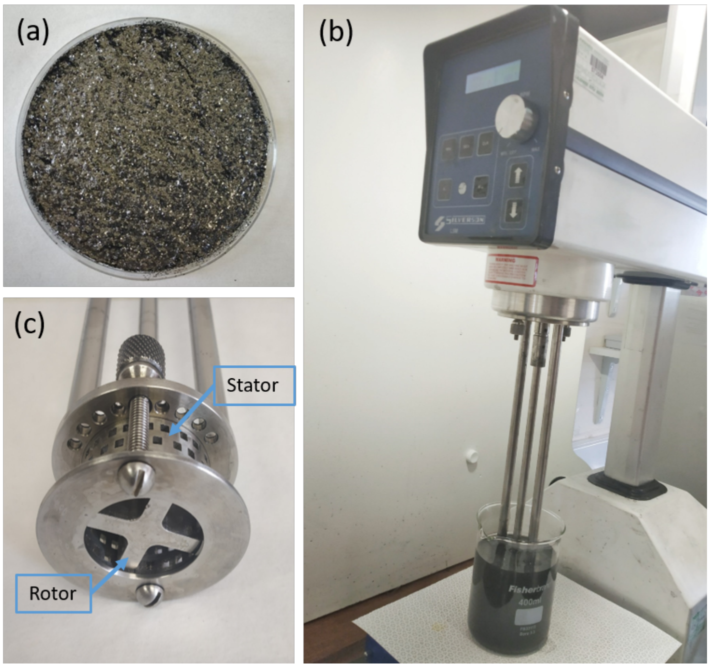

Figure 3.1: a) Graphite flakes used for exfoliation, b) Silverson L5 high shear mixer with mixer head immersed in graphite flakes, NaC and DI water mixture, set at 4500 rpm for 1 hour to produce FLG suspension, c) Shows 32 mm mixer head with its stator and rotor components.

3.2.4 UV-Ozone treatment of fabrics

Fabric substrates were cut into 5 cm × 5 cm dimensions and kept inside an Ossila UV Ozone cleaner for 5 minutes to clean the substrate of any organic impurities present as well as to add oxygen/hydroxyl groups to the surface of the fabric in order to make it more hydrophilic in nature. This helps the water-based graphene suspension to wet the fabric surface and coat on top.

3.2.5 Contact angle measurement

This measurement enables the study of any changes to the hydrophilicity of fabric surfaces due to UVO exposure. The contact angle made by water droplets on nylon, meta-aramid and polyester fabric substrates was measured before and after UVO surface treatment. The Ossila goniometer set-up used for this measurement is shown in Figure 3.3. It includes a monochromatic light source on one end, a camera on the opposite end and a sample stage in the middle. The light source is used to illuminate the sample droplet to aid in the edge detection of droplets for the PC software. The sample stage in the middle can be adjusted in height to fit the frame of the camera. It also has levelling screws

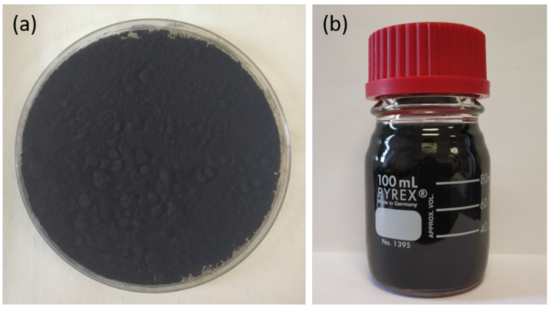

Figure 3.2: a) GNPs powder is shown in a Petri dish of 9 cm diameter and b) shows the prepared GNPs suspension from mixing the GNPs powder in water.

to keep it flat. A high-resolution camera is used to capture the image/video of the sample droplet. This image is then analysed with the help of the provided Ossila PC software.

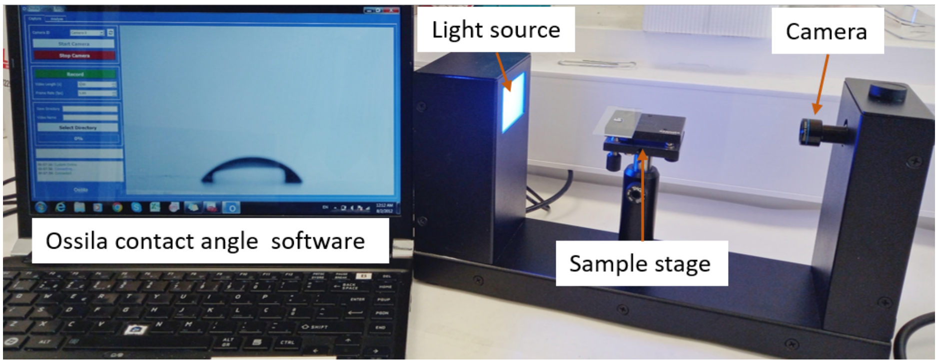

Figure 3.3: Ossila contact angle measurement set-up with monochromatic backlight source, high-resolution camera, height and surface level adjustable sample stage and a PC software to record and analyse the angle measurement.

For the measurement, a fabric substrate was placed on the flat stage in the camera's focal length. Water droplet was then placed on the substrate using a pipette and a 5 seconds video of its evolution was recorded at 30 frames per second rate. Taking a snapshot immediately after placing the droplet was avoided here as a video can capture the evolution of the droplet shape on the substrate which can also be analysed using the provided software and the contact angle at any desired frame can be calculated. Figure 3.4a shows a meta-aramid fabric with a water droplet (with added blue dye in order to distinguish it clearly from the fabric) on the surface and Figure 3.4b shows how the camera of the measurement set-up sees the image. In order to calculate the contact angle, the video was skipped to its last frame (149th frame) and the droplet image at that frame was selected. 4 guidelines were kept around the droplet image to mark the region of interest in the software as shown in Figure 3.4c. The bottom guideline defines the baseline of the droplet. The software fits a polymer function to the outline of this droplet and a tangent drawn at the base corners gave the contact angle between the droplet and the fabric surface. Left and right side angles were calculated this way and averaged out to obtain the contact angle for that sample. The same steps were followed for all the substrates studied for consistency and comparison between the materials.

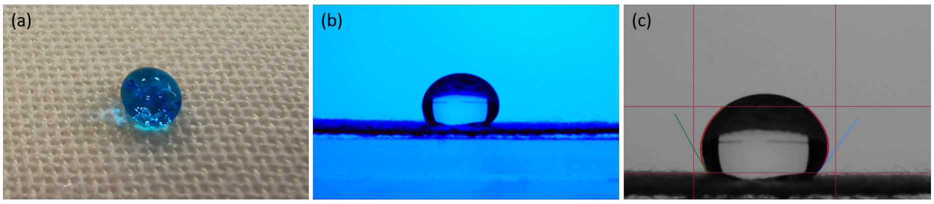

Figure 3.4: a) Picture of a water droplet on the meta-aramid surface showing the hydrophobic nature of the fabric, b) the same view recorded through the goniometer camera and c) image of the last frame of the video to calculate the contact angle. Red guidelines around the droplet image were used to mark the area of interest for the software. Green lines seen at both corners of the droplet are the tangent fit to the outline of the droplet to calculate the angle made with the fabric's surface.

3.2.6 Graphene coating methods

The FLG suspensions prepared as described in 3.2.3 were used to study different coating methods on nylon fabrics such as dip and dry and membrane dip coat as shown in Figure 3.5 to determine the best method to take forward. Optical, electron microscopy and conductivity studies done on these coated fabrics are discussed in Chapter 4.

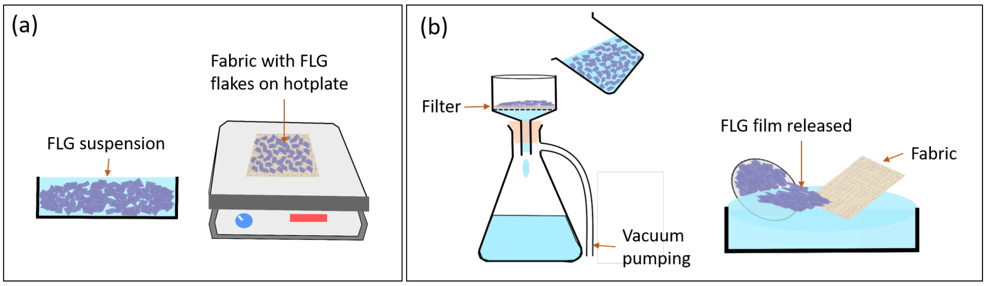

Figure 3.5: Schematic diagram of a) dip and dry and b) membrane dip coat followed for FLG coating on fabrics

Dip and dry coating

Fabric substrates were momentarily immersed in FLG suspension to coat the fibres with graphene flakes, followed by drying on a hotplate at a high temperature to evaporate water (Figure 3.5a). This cycle was repeated multiple times to increase the amount of graphene deposited on the fabric to improve the conductivity of the fabric.

Membrane dip coating

20 ml of FLG suspension was diluted with 30 ml of DI water and vacuum filtered through a 0.2 μm pore-size cellulose membrane. This filters out the solvent present in the suspension and forms a film of graphene flakes on top of the membrane. Once the filtration was done, the cellulose membrane with the FLG film on top was dipped in water at a shallow angle, gently releasing the FLG layer onto the water surface (Figure 3.5b). Nylon fabric immobilised on a glass slide was used to collect the film onto the fabric. It was then dried on the hotplate at 120°C to obtain FLG-coated nylon fabric.

Ultrasonic spray coating

Ultrasonic spraying, as introduced in Section 2.2.5, is used here to coat the fabric substrates with graphene. Ultrasonic spray coater, as shown in Figure 3.6, comprises a sonic syringe, an impact spray shaping nozzle of 48 kHz frequency to spray the suspension, a 30 cm × 30 cm hotplate at the base to keep the substrate on top, set to a temperature high enough to remove of the solvent, and a PC interface (portal software) to control different functions of the system. An exhaust fan is operational at all times during the working of the spray coater to exhaust any fumes and nanoparticles present inside the coater. Figure 3.6 shows the spray coater system used with its main components labelled.

Nozzle movements are controlled via a Cartesian robot with conveyor belt arms. Programs written are stored in a motion controller with specifications on the area of coating, number of cycles, nozzle speed etc. The supplied pathmaster interface within the portal software allows writing, editing and downloading programs into the coater. A 30 cm × 30 cm sized hotplate at the base of the coater is viewed as an x-y plane with the home position (0,0) at one corner of the plate. This helps to select the area to spray on the hotplate. The

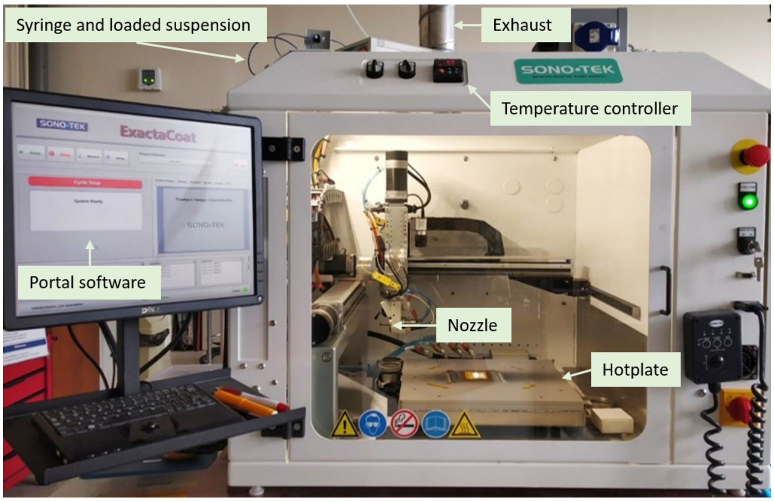

Figure 3.6: Sono-tek Exactacoat ultrasonic spray coater used for this study with an impact nozzle of 48 kHz. A 30 cm × 30 cm hotplate at the base holds the substrates during coating while an ultrasonic nozzle moves over and sprays the suspension onto the substrate. Suspension is loaded in a syringe outside the coater, controlling the pumping rate. All the parameters involved in spraying including the area on the hotplate, the velocity of the nozzle, and the number of passes over the samples can be programmed on the software connected to the system.

height of the nozzle from the hotplate is adjusted with the z coordinate. The temperature of the hot plate is set on a controller separately.

In order to spray the graphene suspension from the nozzle, the suspension was loaded into a syringe connected to Teflon tubes to carry the suspension to the nozzle. For repeated use of the system, the suspension was initially loaded into a reservoir bottle in the spray coater. The Teflon tubes carrying the suspension have two directions, between the reservoir and the syringe and between the syringe and the nozzle. Here, the flow direction was first set to the reservoir-syringe direction to fill a Hamilton 25 ml gastight syringe (model 1025 TLL, PTFE Luer Lock, part number - 82520). The suspension-filled syringe (in plunger pulled position) was then locked into the syringe holder of a syringe-pump system of the coater as shown in Figure 3.7. In order to supply a constant flow rate of loaded suspension, the diameter of the syringe used is provided through the user interface. This helps the pump to determine the appropriate rotation rate for the lead screw, which is connected to a pusher block as shown in Figure 3.7. This way lead screw rotation would move the pusher block forward, pushing the syringe plunger to dispense suspension at a constant rate from the syringe to the nozzle.

The flow rate for dispensing the suspension to the nozzle side was set at

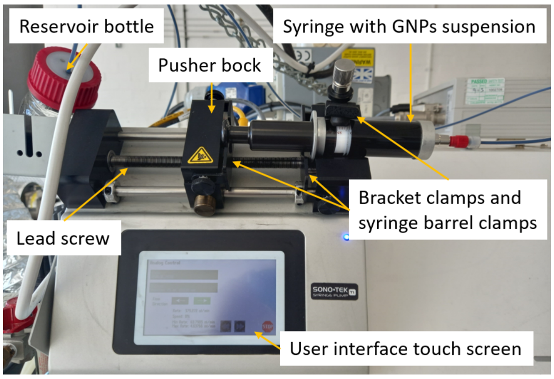

Figure 3.7: Syringe-pump system of the spray coater. It shows a reservoir bottle, syringe and Teflon tubes with loaded graphene suspension. The syringe is locked in place with the help of barrel and bracket clamps. The plunger end is connected to a pusher block which moves forward to push the plunger to dispense suspension from the syringe. The flow rate set by the user decides the rotation rate of the lead screw labelled, which moves the connected pusher block. This is set up to dispense the loaded suspension at a constant rate to the nozzle.

0.7 ml/min. The suspension is pumped into the nozzle where it forms an ultrasonic spray. The impact spray shaping nozzle used here as shown in Figure 3.8, is of fixed 48 kHz frequency and is suitable for large area coatings.

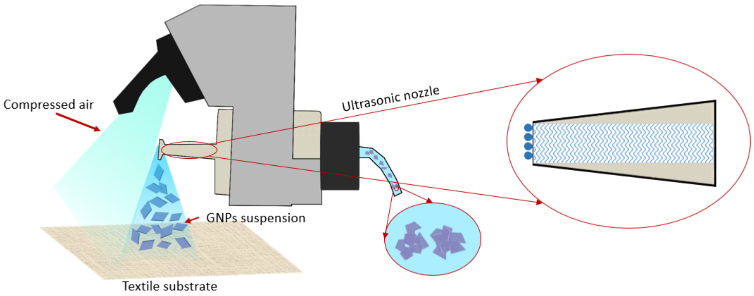

Figure 3.8: Schematic diagram of the working of an ultrasonic spray nozzle. The liquid suspension fed into the nozzle forms stationary waves inside due to the ultrasonic vibration created in the nozzle. This helps atomise the liquid at the tip of the nozzle thus forming the spray. Compressed air shapes and directs the spray onto the substrate. Reproduced from [59]

Fabric substrates are taped onto the hotplate with heat-resistant polyimide tape (Kapton tape) to hold them flat while spraying the suspension. A PET sheet with 3 cm × 3.5 cm area cut out is used as a mask to keep on top of the fabric substrate to get GNPs coating of 3 cm × 3.5 cm area. This is shown in Figure 3.9. The nozzle passes over this area in a raster scan pattern. This nozzle scan over the area is repeated 100 times to have a good conductive coating required for these textile electrodes. A typical program written to spray a 4 cm

× 4 cm area in the middle of the hot plate with 100 passes is given in Appendix A.

The operation steps of the spray coater are listed as simplified guidelines below.

Step 1. The exhaust connected to the inside of the spray coater is turned on

Step 2. The suspension flow direction is set from the reservoir bottle to the syringe and the graphene suspension is loaded into the Hamilton syringe. Flow direction is then changed from reservoir-syringe to syringe-nozzle path and suspension is pushed manually until it reaches the nozzle. Place and lock the syringe between the bracket clamps and secure it with the syringe barrel clamp.

Step 3. UVO-treated fabric substrate is taped onto the middle of the hotplate inside the spray coater with polyimide tape. A 3 cm × 3.5 cm cut-out PET mask is taped on top of the fabric. The hotplate is then switched on and set to 120°C

Step 4. Once the hotplate temperature reaches stable 120°C, the compressed air supply valve is turned on.

Step 5. In portal software, the required program is chosen and press 'cycle start' button is to begin spray coating.

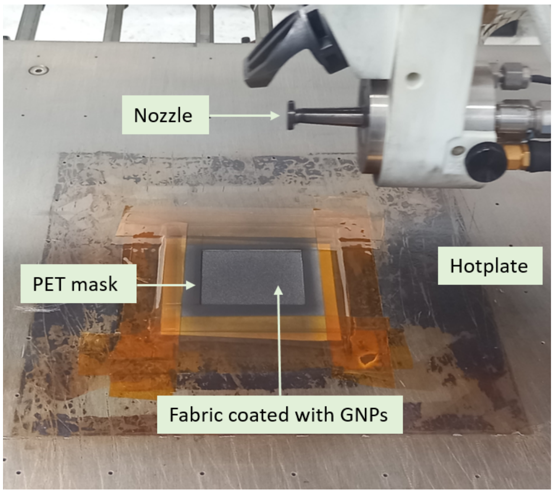

Figure 3.9: Polyester fabric taped down to the spray coater hotplate with a 3 cm × 3.5 cm PET mask on top. The fabric has been coated with a few rounds of graphene spraying, seen in black colour over the fabric and PET mask.

Nylon, polyester and meta-aramid fabrics spray coated with 100 passes of GNPs suspension are shown in Figure 3.10. These samples have GNPs coating of 3 cm × 3 cm dimension in the middle of the fabric seen in black colour.

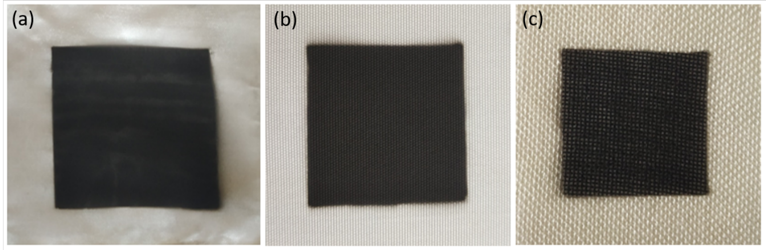

Figure 3.10: a) Nylon, b) polyester and c)meta-aramid fabrics spray coated with 100 passes of GNPs suspension. A 3 cm × 3 cm square-shaped PET mask is kept on top of these fabrics while spray coating to obtain a square-shaped coating (seen in black) with clean edges.

3.3 TENG device fabrication

GNPs spray-coated fabrics discussed above, are used here as electrodes for the fabrication of TENG devices. These double-electrode TENGs have two dielectric tribolayers with electrodes on either side, sandwiching the tribolayers. Their general structure is shown in Figure 3.11a. Fabric-based TENGs fabricated here have two sides. One side has the GNPs coating as electrode with PDMS polymer as tribolayer. PDMS is a highly electronegative material [60] which is non-toxic and inert in nature. The soft and elastic nature of this polymer can maximise the effective contact area with the opposite dielectric material, on contact. This would also help the material to be flexible to fit the body movements. Fabrication of this side from GNPs coated polyester fabric is explained below. This part would be referred to as PDMS side for simplicity. The other side of TENG is where different materials are tested for their performance as a tribolayer, along with a double-sided copper tape as the electrode. This side would be called as test side from here onwards. Hence a complete TENG would be the PDMS side against the test side, termed PDMS-test TENG. For example, a nitrile material used as test material would give a PDMS-nitrile TENG, a schematic diagram of such a device is shown in Figure 3.11b.

3.3.1 PDMS Side

Wiring of textile electrode

Polyester fabrics with ultrasonic spray-coated GNPs were used to prepare the PDMS side of the TENG device. The graphene electrode was connected to a copper wire using silver epoxy and covered with PDMS polymer. For this, one of the 3 cm edges of the 3 cm × 3.5 cm. GNPs coated fabric was connected to

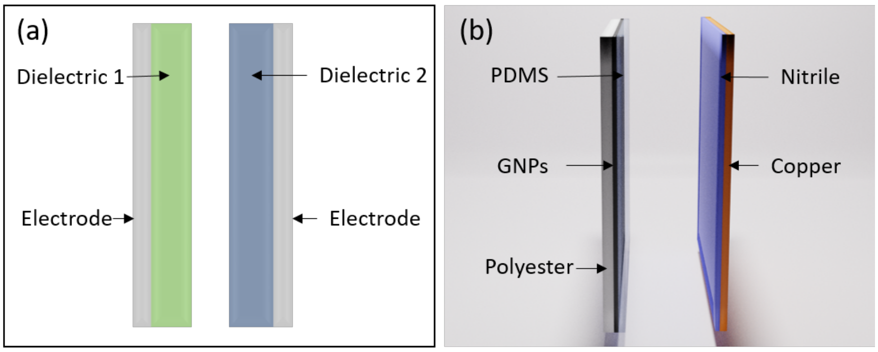

Figure 3.11: Shows a schematic diagram of a) general structure of a double electrode TENG, b) structure of PDMS-nitrile TENG fabricated here.

a 0.1 mm diameter copper wire (Block single core, CUL100/0.10) using silver epoxy (MG Chemicals) paste and dried on the hotplate at 65°C for 20 minutes. This is the electrode on the PDMS side.

PDMS coating

A 10:1 ratio of elastomer to cross polymer was mixed and degassed in a desiccator to make PDMS (SYLGARD 184) which is then spin-coated at 9 rps for 30 seconds on top of the electrode. It is kept in a convection oven at 70°C overnight to cure the polymer. This forms the PDMS side of TENG. Figure 3.12 shows the PDMS side in flat, bent and cross-section positions. Polyimide tapes can be seen at the edge of the device as they are taped down to a glass Petri dish to spin coat PDMS during its fabrication.

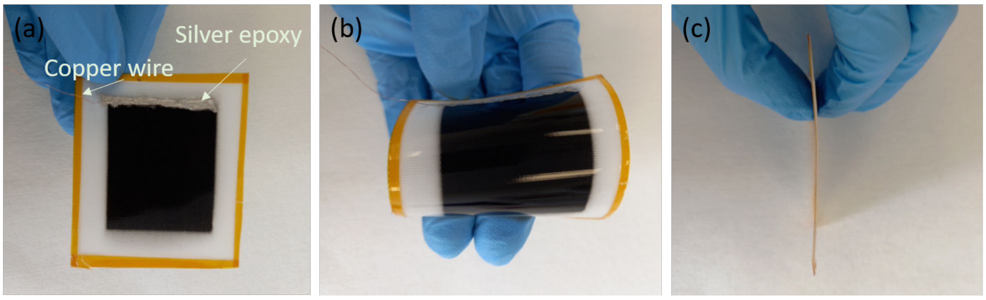

Figure 3.12: PDMS side of TENG fabricated is shown in a) flat, b) bent and c) cross-section positions.

PDMS fluorination by reactive ion etching

JLS Designs RIE 80 Etching System was used on the PDMS layer of the TENG device to chemically modify it with fluorine atoms and make it more electronegative in nature. For this, once the PDMS side is cured it was exposed to 60 seconds of SF_6 gas inside the RIE chamber at 30 sccm (standard cubic centimetres per minute) electrode set point, 100 W power, 30 s gas stabilisation, 60 s process time and 30 s pump time at a chamber pressure of 50 mTorr [58]. The as fluorinated PDMS side was then tested against nylon fabric with a copper electrode (PDMS-nylon TENG) to study the effects of the fluorination of PDMS on the output of this TENG device. SEM was used to assess any signs of microscale modifications, such as etching on the fluorinated PDMS surface.

3.3.2 Test side

For the test side of TENG, the test material of 3 cm × 3 cm dimension is stuck onto a double-sided copper tape which works as the electrode for this side. Materials tested on this side are provided here with their cross-section thickness (± 0.01 mm) along with their company of purchase. They are nylon (0.02 mm), meta-aramid (0.40 mm) and polyester (0.32 mm) fabrics (provided by Heathcoat Fabrics Ltd), nylon-spandex (0.56 mm, purchased from Fabrics King online), satin-silk (0.15 mm, Discover-Direct), cotton (0.25 mm, FT Fashion Track), paper (0.09 mm), aluminised mylar (0.02 mm, Umichen), faux leather (0.75 mm, A-Express), nitrile glove (0.13 mm, Kimtech purple nitrile gloves), neoprene rubber (0.56 mm, T&P Supplies), shoe insole (1.27 mm and 1.82 mm, Supertrade limited), Kapton tape (0.03 mm, Thorlabs), Teflon tape (0.08 mm, Essentials)

3.4 Characterisation

Fabricated GNPs coated fabrics were studied in detail for their conductivity, surface morphology, thickness and mechanical strength for their use as an electrode in wearable devices. The characterisation tools used for these studies are discussed below. The setup used to characterise TENG devices made using these fabric electrodes is explained towards the end sections of this chapter.

3.4.1 Optical microscope

A Nikon LV150 upright optical microscope was used here to study different FLG-coated fabrics to see how well FLG flakes adhere to the fabric surface. Coatings achieved through different techniques including dip and dry, membrane dip coat and ultrasonic spray coating were studied this way.

3.4.2 Scanning electron microscopy

The topology of samples at μm scale was studied with a TESCAN VEGA3 SEM. Samples of bare fabric, GNPs coated fabric, PDMS coating etc. were cut into 1 cm × 1 cm dimension to fit the SEM sample holder and sputtered with a 20 nm thick chromium layer to make them conductive in order to observe under SEM. This does not mask any surface features studied, as those would be at μm scale. Samples were then loaded under vacuum. Imaging was then done at an accelerating voltage of 20 kV and a working distance of 15 mm, with images captured from 1 mm to 5 μm scale magnification.

Cross-section views of the samples can also be studied under SEM by changing the sample holder design to one where the cross-section of the sample can be mounted facing the detector. Figure 3.13 shows the two types of sample holders used with samples mounted on them with double-sided carbon tape.

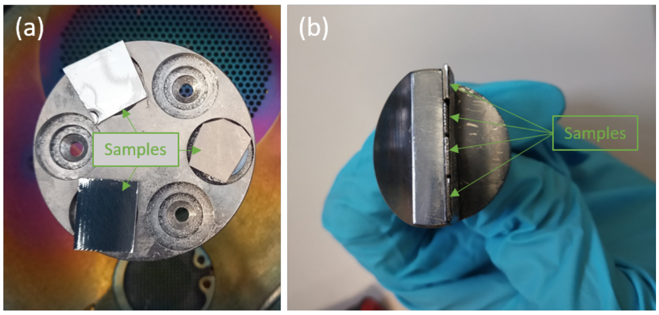

Figure 3.13: Sample holders used in SEM study with fabric and PET samples fixed on top for a) surface and b) cross-section analysis. They are coated with 20 nm chromium on top, seen as reflective silver colour in the picture.

3.4.3 Sheet resistance

It is important to characterise the resistance of the GNPs coated fabrics as they are used here as electrodes in fabricated TENG devices. The van der Pauw method was used to determine the sheet resistance of these coated fabrics. This method relies on obtaining an average resistance of the whole sample instead of its resistance in just one direction, which is obtained in a linear four-probe method. To use this method, the samples need to be homogeneous, of flat shape, isotropic with uniform thickness and should not contain any isolated holes. Then four ohmic contacts are placed at the perimeter (the size of the contacts should be much smaller than the distance between contacts) of any arbitrary shape sample to measure its sheet resistance.

Here square shaped GNPs coated samples of 2 cm × 2 cm dimensions were coated with silver ink at their four corners as their ohmic contacts. The van der Pauw set-up used is shown in Figure 3.14. GNPs coated fabric with silver contacts was placed flat on the set-up and gold pin probes were lowered to be in contact as shown in Figure 3.14a. Two Keithley 2400 are connected with a Lab View program to automatically switch the probes' different sensing directions to calculate the resistance in each direction. Average sheet resistance is determined by the program following the calculations discussed in section 2.4.6.

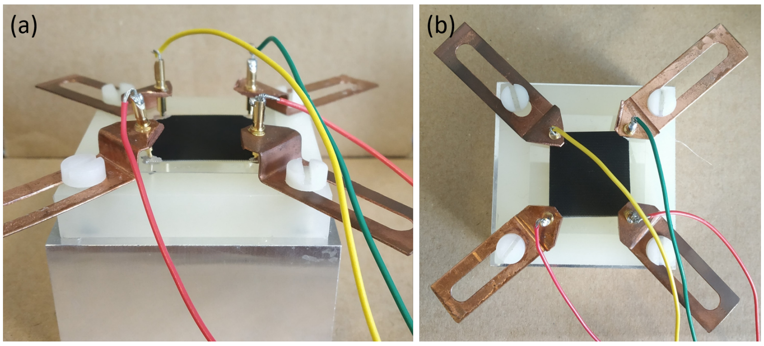

Figure 3.14: Van der Pauw sheet resistance set-up used with GNPs coated sample from a) side and b) top views. Four corners of the GNPs coated fabric were painted with silver ink and gold pins of the set-up were placed in contact. The current was then passed through each edge of the square shape and voltage along the opposite edge was recorded. Van der Pauw formula was applied to calculate the sheet resistance from these values obtained.

3.4.4 Non-contact surface profilometer

A Taylor Hobson TalyScan 150 non-contact scanning instrument was used to study the surface profile of GNPs coatings on PET sheets. Since the fabric surfaces themselves carry a surface roughness of 160 to 330 μm following the weaving pattern, the laser beam used to scan and follow the surface features would go out of focus. For this reason, flat PET sheets of 0.25 mm thickness were used as substrate instead of polyester fabric. GNPs suspension was spray coated onto a PET sheet of 3 cm × 3 cm keeping the same parameters of spray coating used for the fabrics. However, instead of coating the whole sample uniformly with 100 passes, coatings were made in steps of 25 passes. For this, 25 passes of coatings were done on the entire sample first, then one-third of this coated area was covered while the rest got coated with another 25 passes. Then half of this area was covered for the next 25 passes. This way PET substrate has one-third coated in 25 passes followed by a step to 50 passes and then to 75 passes of GNPs spray coated area. This was done in order to study and confirm the thickness made by each of the 25 passes of GNPs spray coating which can also be used to roughly calculate the thickness made by 100 passes of coating on the flat PET surface.

3.4.5 Tensile strength

An Instron 3367 static tensile tester was used to evaluate the tensile strength of fabric substrates of 15 cm × 2.5 cm dimensions. Figure 3.15 shows the tensile tester with pure polyester fabric of 15 cm × 2.5 cm area mounted to test. Fabrics were tested before and after coating with GNPs in order to study any change to their mechanical properties as a result of GNPs addition and spray coating process conditions. The fabric of the same dimension spray-coated with just water was also tested to isolate any effects of the coating process such as spraying and heating of the fabric at 120°C. The ends of the fabric samples

Figure 3.15: Instron 3367 static tensile tester loaded with the polyester fabric of 15 cm × 2.5 cm dimension, clamped tightly with 2716-015 manual wedge action grips.

were covered in Araldite epoxy adhesive and dried in order to have a better grip by the Instron clamps to avoid breakage at the grips. Each loaded sample was set to a displacement of 10 mm per minute and pulled in the vertical direction along the fabric length adding weight on one end while keeping the other end fixed, to determine the breaking point of the sample. Results were recorded as force (kN) Vs displacement (mm) plots for each sample tested. This is then converted to a stress Vs strain plot as this is independent of the size of the sample tested.

3.4.6 Bent/Compression tests

Textile electrodes made by the ultrasonic spray coating of graphene suspension were tested for their stability against various degrees of bending and compression. In case of bending, these electrodes were bent along the curved surface of cylinders of diameters ranging from 2 mm to 13 mm. Sheet resistance values measured after each bending were compared against the initial value of sheet resistance measured before any bending. The same procedures have been repeated for compression diameters as well. Finally, bending and compression cycles are repeated for a fixed diameter, up to 2000 times and sheet resistance values are recorded at different intervals. These measurements would be able to show the performance of these electrodes in terms of consistency and stability against different configurations.

3.4.7 TENG Characterisation

TENG devices fabricated using these textile electrodes were characterised by a motion control set-up made based on the one described in [7]. A voice coil linear actuator (Akribis AVM 90) is connected to a motion controller (Galil motion controller, DMC-30012) and set to move in sinusoidal motion. A guided moving stage connected to the voice coil can produce continuous contact and separation cycles with a stationary side on the other end. The moving left side stage has a metal sample holder. The PDMS side of the TENG device was mounted on this moving side. The other side of the TENG, i.e. the tested material with its copper electrode was then mounted onto the sample holder on the stationary right side of the set-up. These metal sample holders are isolated from the rest of the set-up with insulating nylon blocks (Figure 3.16).

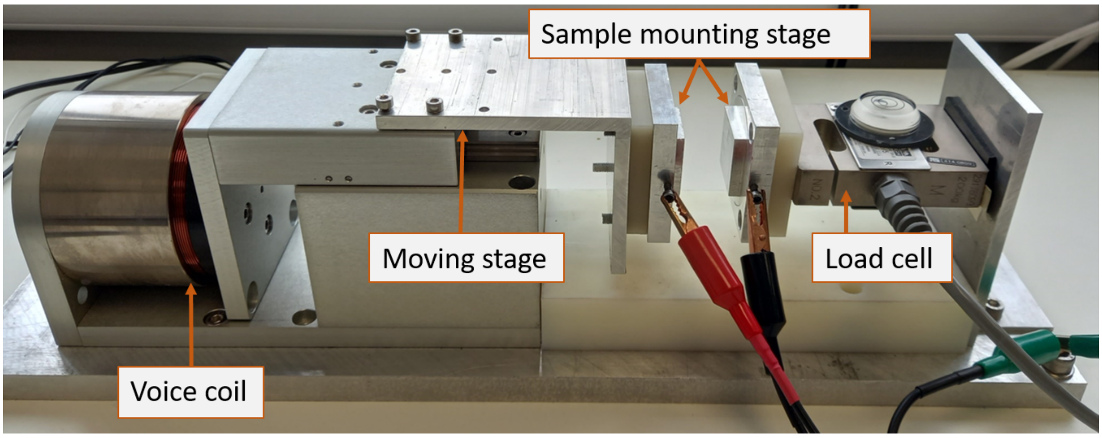

Figure 3.16: Set-up used to characterise TENG in vertical contact-separation mode, made based on [7]. It consists of a moving stage connected to a voice coil controlled via Galil motion control. A stationary right-hand side stage is connected with a load cell at the back to monitor the pressure applied by the moving stage at the contact position of the contact-separation cycle.

A Tedea Huntleigh S-type tension/compression load cell is connected behind the stationary sample holder to monitor the pressure applied by the moving stage on the stationary side, i.e. PDMS side on the test side. The short-circuit current and open circuit voltage generated by this repeated contact and separation between the TENG layers are collected by connectors attached to the metal sample holders and Keithley 6514 source meter of > 200 TΩ input impedance. Outputs are recorded with Excelinx software, owing to its high measurement and low noise characteristics. Figure 3.17 shows the sample holders mounted with TENG layers, moving stage with the PDMS side and right side stationary stage with tested material and copper electrode in separate and contact positions during the repeated contact and separation cycles.

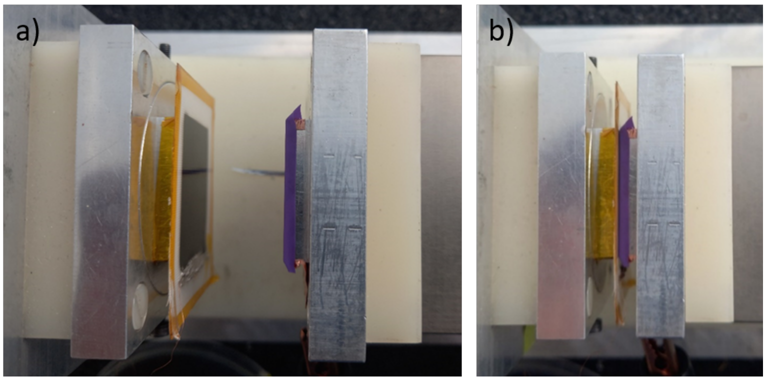

Figure 3.17: Sample mounting stages of the TENG characterisation set-up with PDMS side mounted on moving stage (left-hand side) and tested material (purple nitrile glove here) with its copper electrode on the stationary right-hand side in a) separation and b) contact position during repeated contact and separation mode.

Chapter 4

Characterisation of GNPs coated fabrics as textile electrodes

4.1 Introduction

The main aim of this work is to produce textile electrodes using graphene to pave the way for smart textile applications. For this, different fabrics and different types of graphene suspensions were chosen, since the goal was to use solution-based methods for easier integration with the textile industry.

In this chapter, the results of coating the chosen fabrics with two types of graphene using different coating methods are discussed. This will be done in the light of surface morphology studies, before and after coating, as well as electrical measurements to assess how conductive the coated fabrics are. Optimised coating strategies will be taken forward in the following chapters in the realisation of textile electronic devices in the shape of triboelectric nanogenerators.

4.2 Fabrics

Three types of fabrics were chosen here as a substrate for GNPs coating. They are meta-aramid, nylon and polyester fabrics. These fabrics are used in general for firefighting and clothing fields owing to their properties. Figure 4.1 shows the digital camera and optical microscopy images taken of these fabrics showing their surface and weaving pattern. From the figure, meta-aramid fabric (Figure 4.1a) is loosely weaved compared to nylon (Figure 4.1b) and polyester (Figure 4.1c) which are tightly weaved with no visible gaps at the millimetre scale. Optical microscopy images of the fabrics at 5 times magnification show the density and size of weaves compared to each other. The rough surface of meta-aramid (Figure 4.1d) can be seen with individual short fibrils present throughout. Gaps can be seen in nylon (Figure 4.1e) weaving in the 5× scale while polyester fabric (Figure 4.1f) still maintains tight weaving with no gaps.

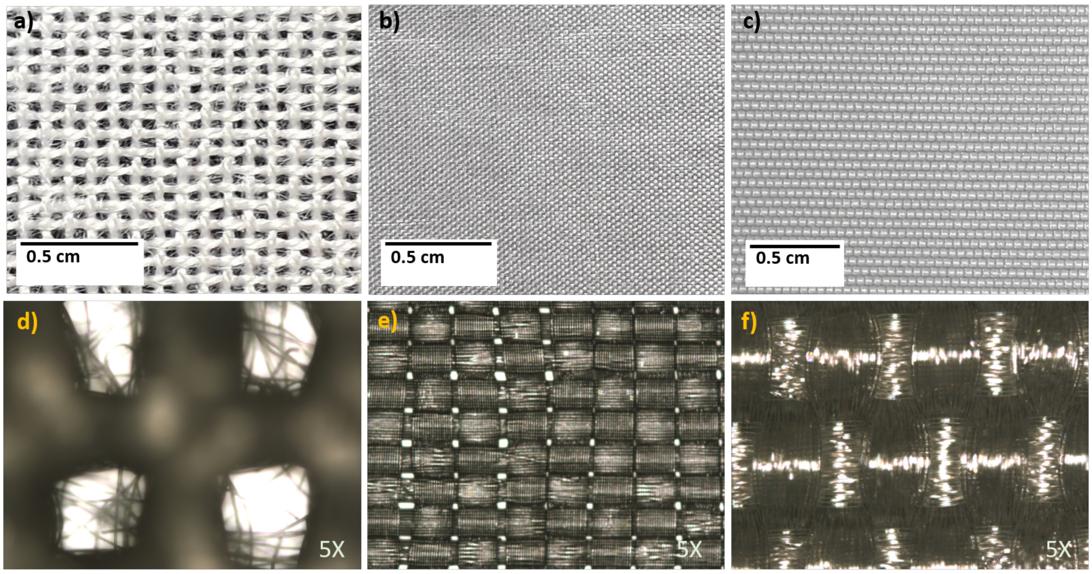

Figure 4.1: Shows camera images of a) meta-aramid, b) nylon and c) polyester fabrics on the top row. The bottom row shows optical microscopy images of d) meta-aramid, e) nylon and f) polyester fabrics. Meta-aramid can be seen loosely woven with rough surfaces while nylon and polyester fibres are more tightly woven with smoother fibres.

Aramids are aromatic polyamides where aromatic rings of six carbon atoms are connected via amide bonds (CO-NH). Depending on the position of these amide bonds, they can be classified into para (1,4) and meta (1,3) aramids. Their strict orientation along an axis provides high strength to the fibres and exhibits a melting point higher than 500°C [61]. These fabrics are highly heat resistant making them suitable for applications such as protective apparel, thermal and electrical insulation etc. They are resistant to a good level of abrasion, organic solvents and breakage and are widely used in aerospace and military sectors. Here we use a 100% meta-aramid fabric (F-00910-Z01, Heathcoat Fabrics Ltd) of 110 to 140 gsm. They were primed and ready for adhesion by the manufacturer.

Nylon fabrics are again synthetic polyamides generally produced from the condensation polymerisation reaction. Depending on the number of carbon atoms present in diamine and acid reactants they are named as nylon 6,6; nylon 6,12; nylon 4,6 etc. Other nomenclatures are followed if they are made from different chemicals. They are generally silky smooth in structure and are used in garments, carpets, food packaging etc. They are durable, strong and have good resistance to abrasion. Here we used superlight, calendered 100% HT Nylon 6,6 (G-60287-Q10, Heathcoat Fabrics Ltd) of 21 gsm.

Polyester, also known as polyethylene terephthalate is generally produced by reacting ethylene glycol and purified terephthalic acid. Polyesters are also widely applied in apparel. This material is used in fabric as well as flat plastic sheet form for graphene coating here. In order to distinguish the two, fabrics would be referred to as polyester and flat sheet form would be referred to as PET sheet. Here we use (M-09305-A01, Heathcoat Fabrics Ltd) 100% polyester fabric of 269 gsm.

4.2.1 SEM on fabrics

Fabric surfaces were further studied with the help of an SEM to look at their roughness and individual fibre structures at μm scale. Figure 4.2 shows the meta-aramid, nylon and polyester fabrics at mm scale along with their individual fibres at μm scale. Meta-aramid fibres display roughness down to the fibre scale here while the rest are seen smoother at this scale. Nylon fabric is the most densely packed, while meta-aramid is the least dense out of these three. It is important to study the surface properties of these fabrics as they could influence the adhesion of GNPs on top.

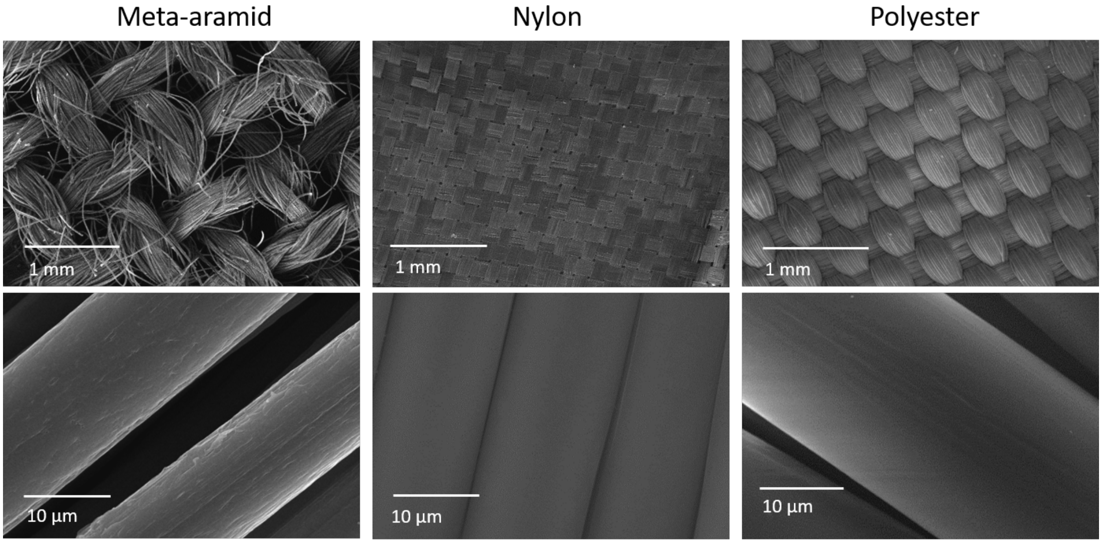

Figure 4.2: Left to right: SEM images of meta-aramid, nylon and polyester fabrics at mm on the top row and corresponding fibres in the bottom row.

4.2.2 Contact angle measurements

The contact angle made by a water droplet at each fabric surface was studied with the help of a contact angle goniometer. Measurements were done on pure and UVO-treated fabrics to understand the change in hydrophilicity of their surfaces as a result of UVO exposure and they were analysed as discussed in Section 3.2.5. Figure 4.3 shows the droplet (seen through the goniometer camera) on each fabric surface before (0′UVO) and after 5 minutes (5′UVO) of UVO treatment.

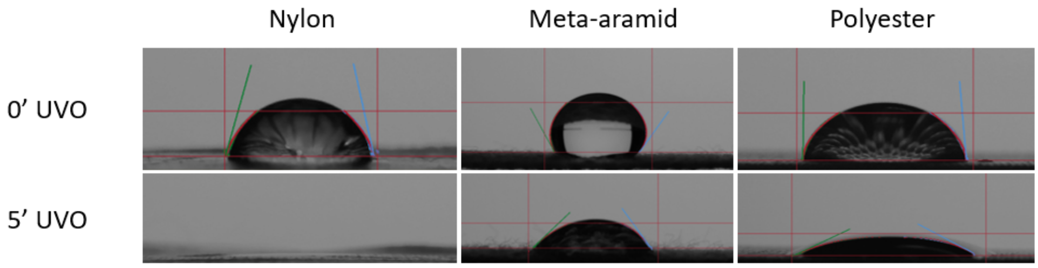

Figure 4.3: Contact angle images of water droplets on nylon, meta-aramid and polyester fabrics before (0′) and after 5 minutes of UVO (5′) treatments showing the clear increased hydrophilicity after UVO surface treatments. Red guidelines are used in the Ossila PC software to select the region of interest, green and blue line segments are tangents drawn to calculate the contact angle at the left and right corners respectively.

Meta-aramid fabrics are highly hydrophobic in nature, seen from the spherical shape formed by the water droplet on its surface before UVO treatment, forming a 122°contact angle. This is followed by polyester fabric with 87°and nylon with 76°. All three fabrics were then treated with 5 minutes of UVO and contact angle measurements were repeated on these. It resulted in a drastic change from their previous values with meta-aramid showing 48°, polyester 26°and nylon 0°. This enhanced hydrophilic nature of these fabrics benefits the spray coating of GNPs suspension on them as they are water-based suspensions, making it easier to wet and interact with the fabric surface. Figure 4.4a summarises the change in contact angle for each fabric before and after UVO treatment. Images of a water droplet with green dye on pure and 5 minutes UVO treated meta-aramid fabrics are shown in Figure 4.4b and 4.4c respectively, clearly showing the change to the water droplet as a result of the UVO surface treatment. The spherical nature of the droplet changes to the spreading of the droplet on the UVO-treated surface owing to the increased hydrophilicity.

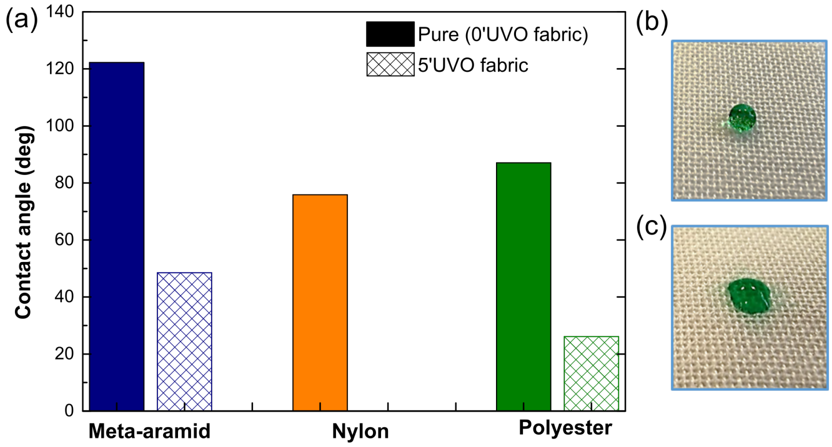

Figure 4.4: a) Contact angle made by a water droplet on pure and 5 minutes UVO treated fabrics of meta-aramid (blue), nylon (orange) and polyester (green). Images of water droplet (with green dye added to distinguish them from the substrate) on b) pure and c) UVO-treated meta-aramid fabrics are shown next to the plot.

4.3 Graphene

This study used two types of water-based graphene suspensions: FLG and GNPs. FLG is made from exfoliating graphite flakes while GNPs are purchased in powder form as discussed in Sections 3.2.2 and 3.2.3 of chapter 3. Different methods of graphene coating on fabrics were followed in order to select the best suspension and method for the fabrication of fabric-based electrodes.

4.3.1 FLG

Graphene is hydrophobic in nature, so dispersing graphene flakes in water would result in the re-aggregation of the flakes. A surfactant material can help with this owing to its amphiphilic nature, enabling it to bond with both hydrophobic and hydrophilic ends, suspending the graphene flakes in water. They are also useful in the exfoliation process. The main drawback of using a surfactant is that they are insulating in nature, which would reduce the conductivity of the samples made with this suspension and it is not always possible to remove the surfactant after the coating procedure.

FLG flakes obtained here have an average lateral dimension of around 110 nm, with 4 layers per flake on average as around 50% of the flakes contain one, two or three layers of graphene [58]. Any defects present in the basal plane of FLG flakes were studied by Shin et al. with the help of X-ray photoelectron spectroscopy in this paper. For this, a ratio of sp^3 hybridised carbon present to that of sp^2 is studied. Sp^3 hybridised carbon indicates the presence of a defect since graphene contains only sp^2 hybridised carbon atoms in its structure. They obtained a value of 0.17, lower than HOPG and graphite. This shows that a high-quality FLG is obtaied through this shear exfoliation process. A detailed study on these can be found in here [58]

4.3.2 GNPs

Since this is a commercially available product, it is important to characterise and understand its composition. In order to assess the elemental composition of these purchased GNPs, a minuscule amount of the powder is placed securely on an adhesive carbon tape to study under the energy-dispersive X-ray spectroscopy (EDS) part of SEM. A sample location is selected first and eight different rectangular areas distributed all over the selected area were scanned as shown in Figure 4.5 to calculate the average elemental composition of these commercially produced GNPs. They are labelled A to H. Composition of carbon (C) and oxygen (O) corresponding to each area in weight % are shown in the table of Figure 4.5. These data show an average oxygen content of 13.5% present in these GNPs which seems to indicate that chemical methods were used by the manufacturer. It should be noted that the production method is not disclosed by the manufacturer.

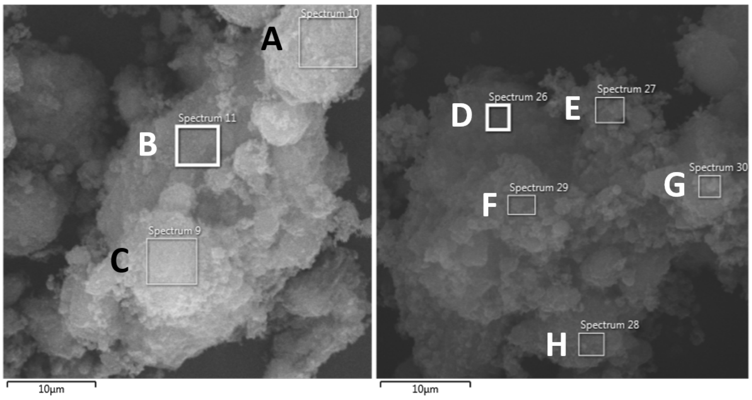

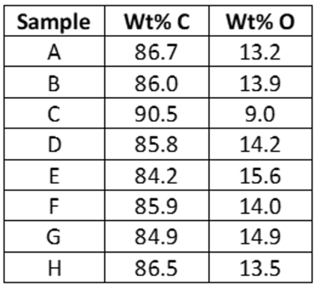

Sample	Wt% C	Wt% O
A	86.7	13.2
B	86.0	13.9
C	90.5	9.0
D	85.8	14.2
E	84.2	15.6
F	85.9	14.0
G	84.9	14.9
H	86.5	13.5

Figure 4.5: SEM image of GNPs powder used for EDS studies. Locations marked from A to H are the rectangular areas selected for elemental analysis through EDS. The table to the right shows the percentage of carbon (C) and oxygen (O) content present in the corresponding A to H areas by weight.

GNPs suspension prepared as described in Chapter 3, was ultrasonically spray coated on a glass slide to study under Raman spectroscopy. A glass substrate was chosen here for this study as fabrics have their own peaks at the G peak region of graphene which would interfere with this study. A 10 μm × 10 μm area was selected within the sample for G and 2D peak (discussed in Section 2.4.5) mapping as shown in Figure 4.6. A 1 μm radius laser beam is moved by 1 μm in each x and y direction to collect data points to map out the entire 10 μm × 10 μm area. Mapping gives a better representation of the sample, covering a larger area, providing more data points for an average value, compared to a single spot Raman spectrum. Here, on average, the G peak position varied between 1578 to 1592 cm^{-1} while the 2D peak showed a position variation of 2693 to 2710 cm^{-1}. In general, change in G peak positions indicate the presence of strain [62] and doping [63] in graphene and the two can be distinguished by studying the ratio of the shift in 2D peak to that of G peak [64].

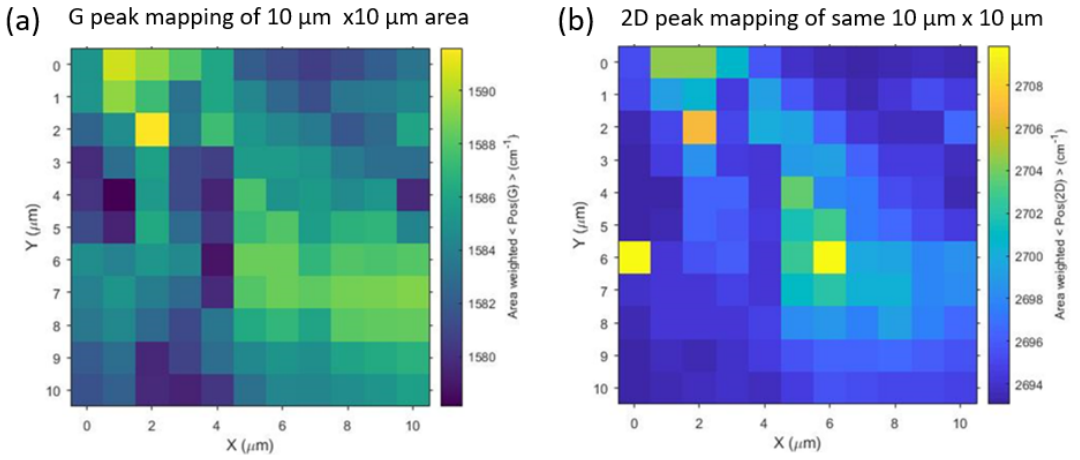

Figure 4.6: Raman mapping of a) G peak and b) 2D peak positions of selected 10 μm × 10 μm area of GNPs spray coated on glass substrate

A detailed Raman study was done by Dimov et al.[65] on these GNPs to understand any sp^3, vacancy and boundary defects present. This was done by fabricating a GNPs film by vacuum filtration and transferring the film onto a SiO_2 substrate by membrane dip coat method discussed in Section 3.2.6. 2D peak comparison of GNPs Raman spectrum to that of graphite gave an average of 11 layers present in a GNP flake. Plotting intensity ratios of D to G peak against D to D′ (shoulder peak present in G peak) indicated no sp^3, vacancy and boundary defects present in these samples and no defects were introduced to the basal plane by the shear exfoliation involved in the production of GNPs suspension.

4.4 FLG coating

Different methods were explored to coat FLG on the surface of nylon fabric, including dip and dry, membrane dip coat and ultrasonic spray coat, as described in Section 3.2.6. Fabrics coated this way were observed under optical and SEM to study the graphene adhesion on nylon by each method. As these graphene-coated fabrics are intended for use as electrodes, it is important that they exhibit low resistance. For this, graphene flakes present on the fabric surface should be closely packed, connecting each other to have a conductive pathway. SEM studies conducted were helpful here in showing the distribution of FLG flakes on the fabric surface all the way down to the fibre level.

4.4.1 Dip and dry method

The first solution coating method tested was the industry scalable dip and dry method. Here nylon fabric was coated with FLG flakes by simply dipping the fabric in FLG suspension and drying it on a hotplate. This process was repeated until the fabric looks saturated with dark colour, indicating the amount of FLG flakes coated. The digital camera image of the coated fabric obtained is shown in Figure 4.7, it does not show an even colour across the fabric with some parts appearing darker than others. This shows the uneven distribution of the graphene flakes on the fabric. Uncoated fabric areas can be seen through the FLG coating (in white colour).

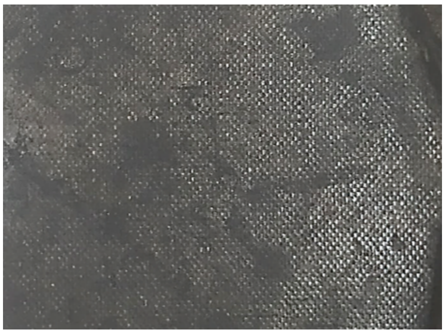

Figure 4.7: Digital camera image of nylon fabric coated with FLG flakes, following the dip and dry method.

This was further studied on μm level using SEM, which was able to show the graphene flakes on nylon fibres. SEM images of FLG-coated nylon fabric are shown in Figure 4.8, from 200 μm fabric level to 10 μm fibre scale. This shows poor flake density obtained through the dip and dry method. Flakes lay disconnected on the surface, clearly indicating this method would not be able to produce a conductive sample as the flakes need to be in contact for conduction across the fabric.

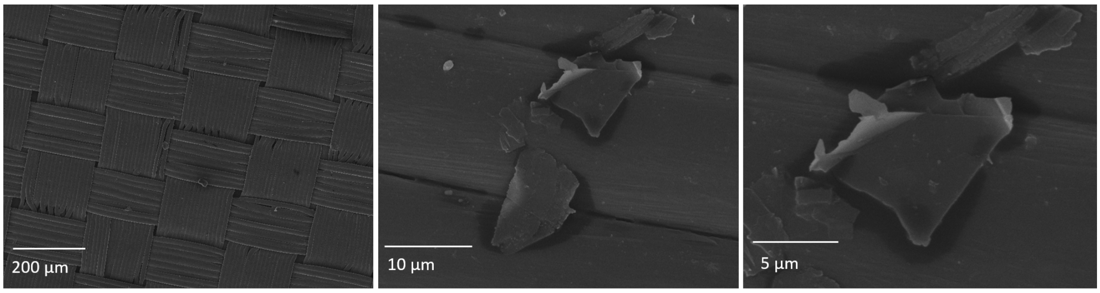

Figure 4.8: SEM images of nylon fabric coated with FLG flakes following the dip and dry method with increasing magnification. Loose graphene flakes can be seen down to the fibre level.

4.4.2 Membrane dip coat

In this method, FLG suspension was filtered through a 0.2 μm cellulose filter under vacuum to form a thin film of graphene flakes on the membrane which is carefully transferred onto the nylon fabric to complete the coating. This method is explained in detail in Section 3.2.6. The fragility of thin films produced this way makes them prone to cracks as seen in the digital camera image shown in Figure 4.9. The sample obtained here looks much more uniform in coating compared to the previous method, as apart from the cracks present, the sample looks uniformly covered in FLG flakes.

Figure 4.9: Digital camera image of nylon fabric coated with FLG flakes, following membrane dip coat method.

SEM image corresponding to this membrane dip coat process is shown in Figure 4.10. FLG coating can be easily distinguished as nylon fibres are smoother in nature as seen in earlier SEM images in Figure 4.2. From fabric to individual fibre level, better surface coverage with better flake density is observed compared to the dip and dry method.

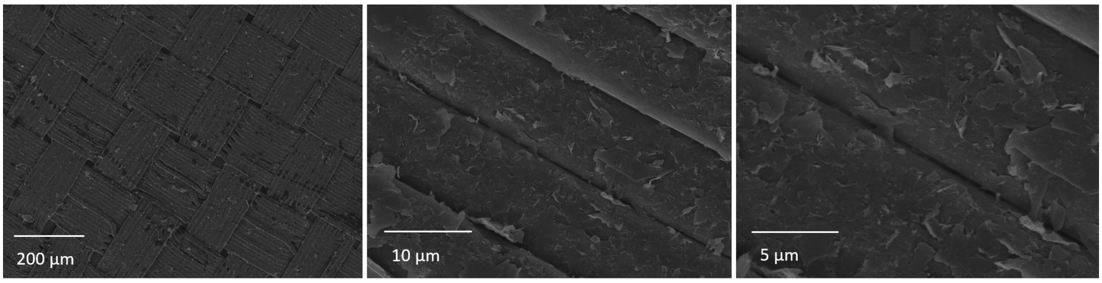

Figure 4.10: SEM images obtained for membrane dip coated nylon fabric to individual fibres. FLG flakes can be seen covering the fibres as adding roughness to otherwise smooth fibres

Optical microscopy images were also taken for the membrane dip-coated fabric at different magnifications, shown in Figure 4.11. Graphene flakes can be seen in shiny gold colour on the fabric surface. Due to the inherent roughness present on the fabric scale, the entire viewed area does not appear in focus as seen in the images.

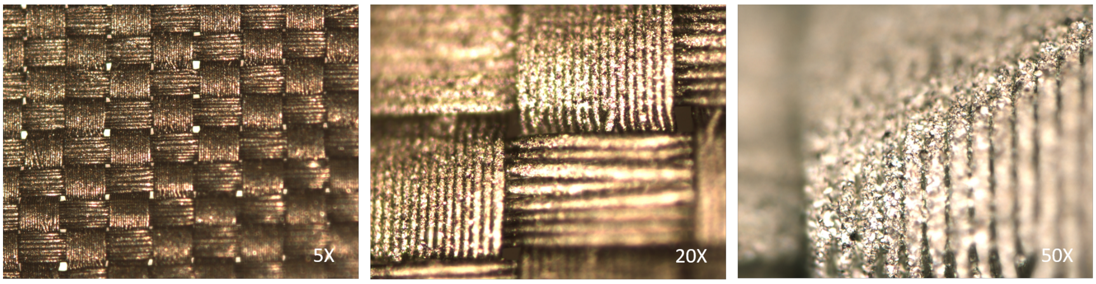

Figure 4.11: Optical microscopy images obtained for membrane dip coated nylon fabric. FLG flakes can be seen as shiny particles at 5, 20 and 50 times magnification.

4.4.3 Ultrasonic spray coating method

Finally, the method of ultrasonic spray coating of FLG suspension was used with the same nylon fabric. FLG suspension was loaded and sprayed onto the nylon fabric kept on a hotplate at 120°C. It shows a uniform and smoother coating of FLG on the fabric compared to the previously mentioned methods followed, shown in the digital camera image of Figure 4.12.

SEM images of the spray-coated nylon sample in Figure 4.13 show fibres with a much smoother coating as seen in 50 and 10 μm while the intersection of yarns of opposite direction shows the accumulation of flakes. Among the

Figure 4.12: Digital camera image of nylon fabric coated with FLG flakes, following ultrasonic spray coating method.

different methods of FLG coating studied on nylon fabric, the ultrasonic spray coating method shows seamless continuous coverage over the fabric surface.

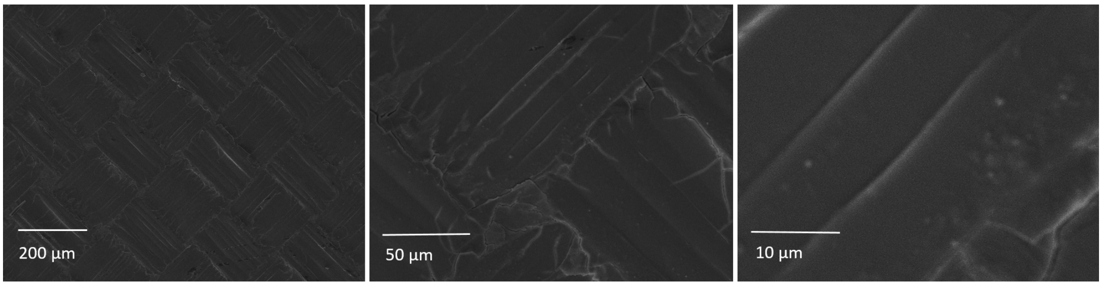

Figure 4.13: SEM images nylon fabric spray-coated with FLG suspension. It shows a much smoother coating of flakes from 200 μm scale to fibres on 10 μm.

4.4.4 Electrical resistance study on FLG coated fabrics

FLG-coated fabrics prepared by the methods discussed above were studied for their electrical conductivity as the goal is to use them as electrodes in TENG devices. Sample electrical conductivity was tested with a multi-meter first and if they show resistance in the kΩ range, the van der Pauw sheet resistance method is used to characterise it more precisely. But here, all the FLG-coated nylon fabric samples were found to be insulating in nature even for the smoother spray-coated fabric, where a much higher quantity of graphene flakes was present compared to the dip and dry and membrane dip coat process. This comes from the amount of insulating surfactant material used in the production of FLG suspension. Removing surfactant from coated surface involves dipping the sample in water as described in [58]. But this process on FLG spray-coated fabrics lifts off FLG flakes and leaves the insulating fabric behind. This surfactant must be used in the preparation of FLG suspension as they are essential in dispersing the exfoliated FLG flakes in water and avoiding re-aggregation. Considering the conductivity and density of graphene flakes present on coated surfaces, FLG suspension does not suit well for the fabrication of textile electrodes.

4.5 GNPs coating

GNPs suspension prepared by mixing the purchased GNPs powder in DI water was used here to coat the fabrics. From the previous section on FLG coating, ultrasonic spray coater was chosen as the best method of coating as they produce a uniform coating over the fabric surface. GNPs suspension was loaded into the coater and spray coated onto all three meta-aramid, nylon and polyester fabrics kept on the hotplate at 120°C, they are then studied for their morphology, conductivity, thickness and mechanical strength.

4.5.1 Ultrasonic spray coated fabrics

GNPs spray-coated fabrics were prepared based on Section 3.2.6. They were cut into less than 1 cm × 1 cm size and sputter coated with chromium to observe under SEM to study the adhesion of the GNPs to the fabric features. Figure 4.14 shows the SEM images obtained for a) meta-aramid, b) nylon and c) polyester fabrics used in this study. All three fabrics were spray-coated with the same parameter settings. GNPs suspension prepared following Section 3.2.3 were loaded onto spray coater, fabrics were taped down to the hotplate inside at 120°C and 100 passes of suspensions were then sprayed onto each fabric. They were studied under SEM on fabric at 200 μm all the way down to the magnified fibre level. Well-coated GNPs on fibre level and following the rough features of each fabric are visible in Figure 4.14 compared with the insulating FLG-coated fabrics. This contributes to the overall better conductivity of the coated fabric, making it the optimal method and type of suspension here for the fabrication of textile electrodes.

4.5.2 Sheet resistance study

GNPs spray-coated fabrics tested simply with multimeter probes were found to be conductive in kΩ range, so they were studied systematically to understand their conductivity. As discussed in Section 4.2.2, the UVO treatment of

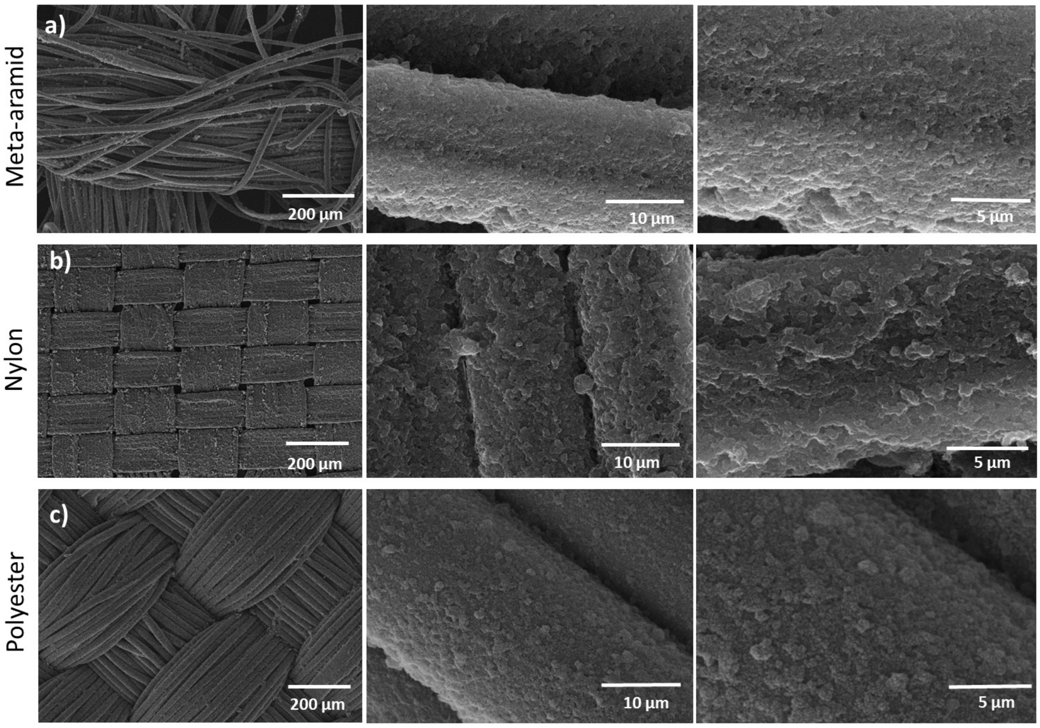

Figure 4.14: SEM images of GNPs coated a) meta-aramid, b) nylon and c) polyester at fabric level to individual fibre level magnification. It shows GNPs adhering well to the fabric surface following the roughness of the fabric. Reproduced from [59].

fabrics makes them more hydrophilic, which should improve the ultrasonic spray coating with water-based GNPs suspensions. To test this, UVO-treated fabrics and the corresponding untreated fabrics were spray-coated with GNPs under the same conditions. The van der Paw method was used here to calculate the average sheet resistance of each of the GNPs coated fabrics and these measurements were done with the help of Dr Agnes Bacon during her PhD. Figure 4.15 shows the results for the three fabrics, with (5 min UVO - GNPs coated) and without (no UVO - GNPs coated) UVO treatment prior to the spray-coating.

The lowest resistance value achieved here was 45 kΩ/sq for both nylon and meta-aramid after UVO treatment. Surface treatment has negligible to no effect on polyester and nylon fabrics respectively while meta-aramid sheet resistance value went down by an order of magnitude to reach the lowest of 45 kΩ/sq same as nylon. This behaviour of nylon and polyester can be explained in terms of their surface morphology. Nylon fabric as seen from the SEM images of Figure 4.2 already has the least surface roughness to begin with, so it is already optimal for the GNPs coating. Compared to nylon, polyester fabrics

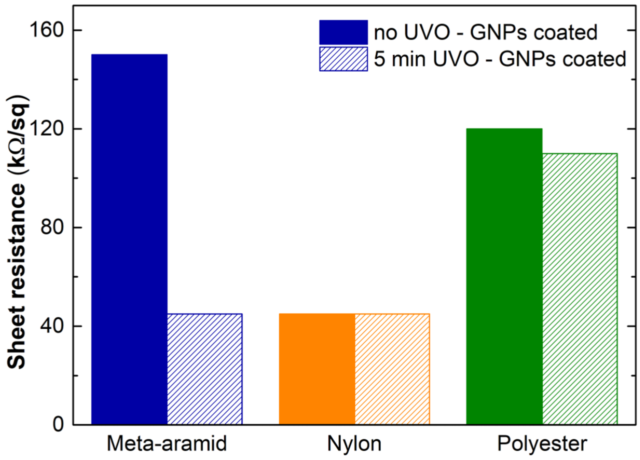

Figure 4.15: Sheet resistance values of GNPs coated meta-aramid (blue), nylon (orange) and polyester (green) fabrics obtained by van der Pauw method. Each fabric type prepared with and without UVO surface treatments is labelled as 5 min UVO and no UVO in the graph.

carry a bit more roughness, but their fibres are very closely packed for a continuous coating on their surface, hence the smaller difference in sheet resistance before and after UVO exposure.

4.5.3 Raman spectra of GNPs spray coated on fabrics

Compared to meta-aramid and nylon fabrics, polyester has fewer Raman peaks within the same 1200 to 2800 cm^{-1} wave number range that studies for graphene / graphite focus on. Figure 4.16 shows the Raman spectra corresponding to each fabric. Therefore, polyester was chosen here to study the Raman characteristics of the GNPs coated fabric as both fabric and graphene peaks can be clearly distinguished.

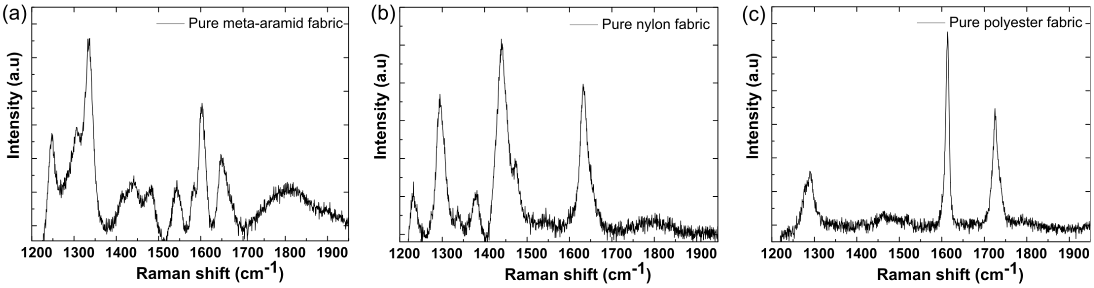

Figure 4.16: Raman spectra of pure a) meta-aramid, b) nylon and c) polyester fabrics in 1200 to 1900 cm^{-1} wavenumber range.

Pure and GNPs spray-coated polyester fabrics were studied with a 514 nm laser as shown in Figure 4.17. Pure polyester fabrics have peaks around 1300, 1610 and 1750 cm^{-1}. The first two peak positions are close to graphene's D and G peak positions. The Raman spectrum of GNPs coated polyester fabric (4.17b) has the D and G peaks of graphene (labelled) along with shoulder peaks from the underlying polyester fabric. The polyester fabric peak around 1750 cm^{-1} can be seen at the same position in GNPs coated polyester as well at a lower intensity, as GNPs peaks show higher intensity peaks. This is followed by the 2D graphene peak around 2700 cm^{-1} (labelled) with no interference from the polyester substrate as there are no peaks in that region. i.e. GNPs coated polyester plot shows the peaks corresponding to both graphene material and polyester fabric, confirming the coating on top.

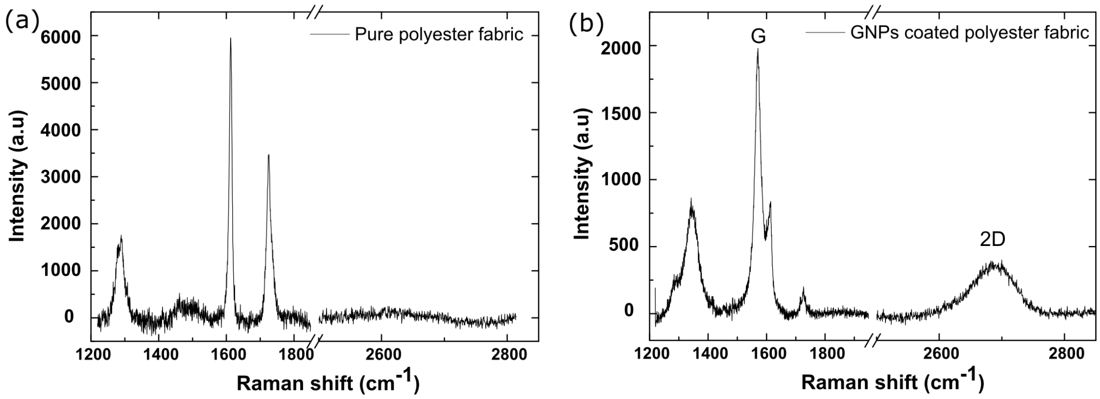

Figure 4.17: Raman spectra of polyester fabric a) before and b) after spray coating with GNPs. Peaks present for pure polyester fabric can be seen at the same locations for GNPs coated polyester at lower intensities along with graphene peaks.

4.5.4 Optical profilometer

A Taylor Hobson TalyScan 150 non-contact scanning instrument was used to study the thickness and surface roughness of spray-coated GNPs on a PET sheet. Here PET sheet was used instead of fabrics as the inherent surface roughness of fabrics takes the scanning laser beam out of focus. A 3 cm × 3 cm sample was prepared with 3 different thickness planes within the same sample by varying the number of passes by 25, 50 and 75 as described in Section 3.4.4.

A 1.5 mm × 24 mm area of this sample was selected to scan across the steps with a laser beam and the results are shown in Figure 4.18. Colour codes show the variation in thickness ranging from around 20 μm in blue all the way to 140 μm in red. Here, the 25 passes coated area, labelled as step 1, shows an average thickness of 20 μm while step 2, in bluish green colour, corresponds to a thickness of 70 μm. This indicates a difference in 50 μm from step 1 to 2 of 25 passes difference. The same calculations are repeated from step 2 to step 3 of orange colour corresponding to 120 μm, confirming the 50 μm step size for every 25 passes. This translates to a thickness of 200 μm for 100 passes of GNPs coating, which is the one followed for all the electrodes fabricated. However, this value is likely to be lower for the same amount of coating followed on a fabric surface since part of the GNPs would get absorbed or sinked into the fabric roughness as opposed to flat plastic PET sheets. A similar study on PDMS coating on polyester fabric and PET sheet and the corresponding difference in thickness values are discussed in Section 5.3

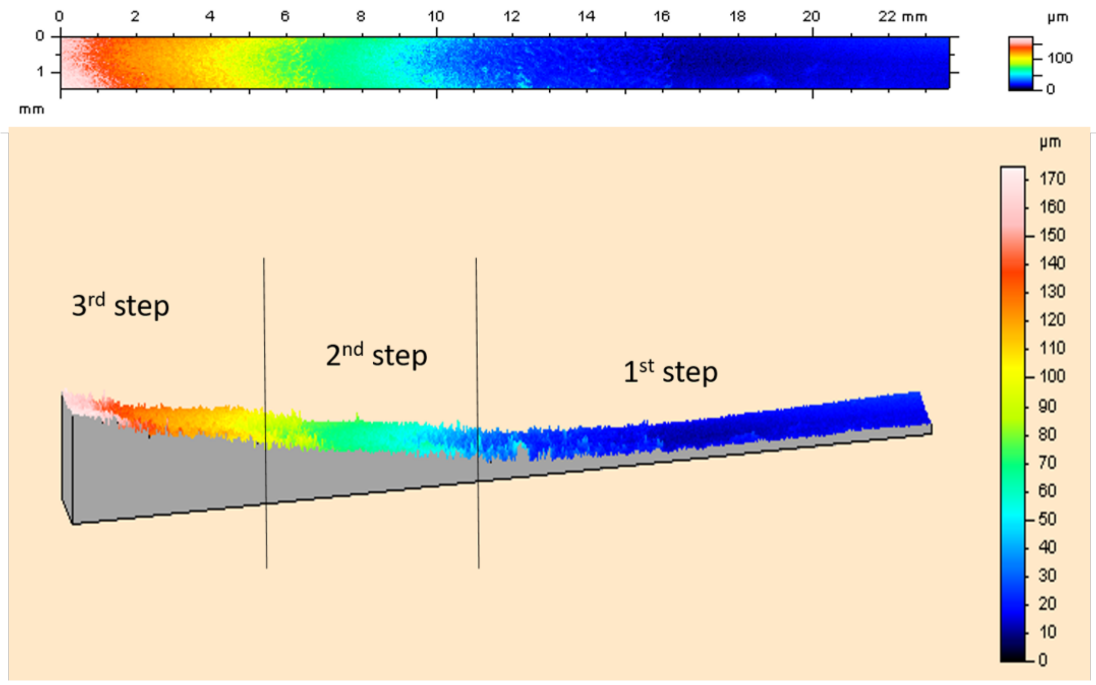

Figure 4.18: Talyscan image of GNPs coated PET sheet of 3 cm × 3 cm dimension showing different steps produced on the substrate. Each step corresponds to 25 passes of GNPs spray coating with 1st step of 25 passes to 3rd step of 75 passes clearly showing the increase in thickness. Each step roughly corresponds to 50 μm in thickness.

Figure 4.19 shows a surface roughness study conducted on the same sample by scanning along the same step area to understand the range of roughness encountered on each. For the first one, a length of 14.4 mm was chosen to scan (dotted line segment in 4.19a) in the step 1 region (blue) of 25 passes. The corresponding roughness plot in 4.19b shows a roughness variation of around 12 μm for the 25 pass area. The same measurements were repeated for step 3 region of 75 passes (dotted line segment in the red colour region of 4.19c) shows a higher fluctuation in roughness amounting to a total roughness range of around 30 μm.

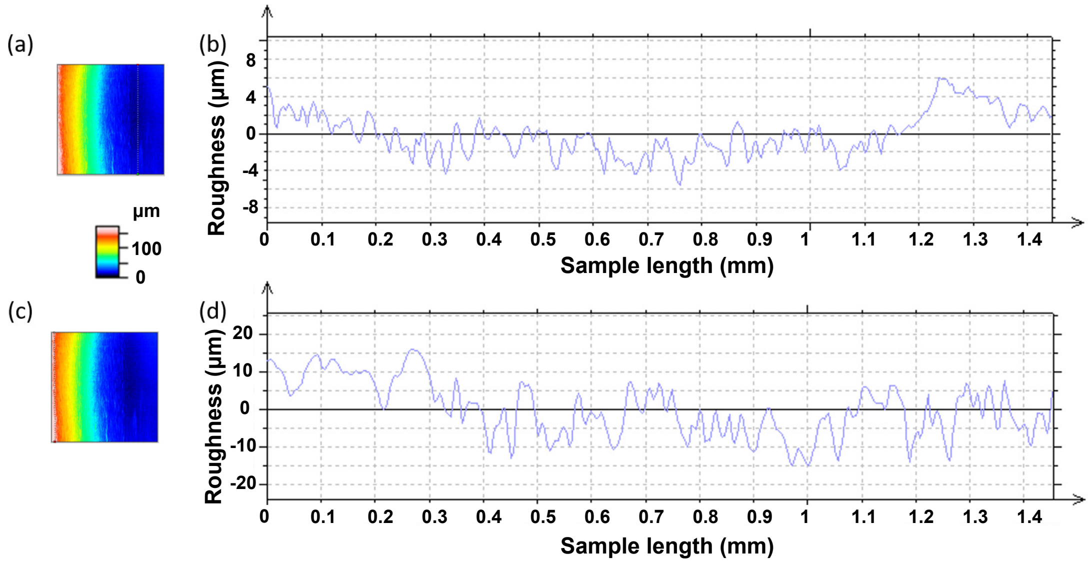

Figure 4.19: Roughness of GNPs coated PET surface along the a) 25 (blue colour region) and c) 75 pass (red colour region) steps of coating showing the range of roughness obtained for each. 25 pass coated area shows roughness range of 12 μm while 75 pass area shows 30 μm of fluctuation.

4.5.5 Mechanical strength of textile electrodes

Since the goal of this work is for these GNPs coated fabrics to be a part of a wearable device, it is important to study their response to continuous cycles of stress, strain and tensile strength. This is done to emulate the mechanical deformations made on the wearable device such as bending or stretching caused by human motions. Two types of tests were done here to study this, bend and compression cycles of the textile electrodes around a curved surface and tensile tests to figure out the breaking point of the fabric from stretching it.

Bending and compression cycles

Here textile electrodes were bent around cylinders of various diameters to see any change to their sheet resistance values. This was done for nylon and polyester fabrics with no UVO treatment, as they do not respond considerably to this surface treatment while meta-aramid does. Even though both electrode samples are tested within the same range of 2 to 13 mm bending and compression diameters, they are not always tested for the exact diameter values. These samples are individually tested at different diameters of < 13 mm and shown in the same plot for better comparison. Figure 4.20a shows sheet resistance values (in log scale) of nylon (orange) and polyester (green) electrodes after bending around cylinders of diameters ranging from 2 to 12 mm and 4.14b shows a polyester electrode in a bent position for reference. The first data point, referred to as flat, indicates the sheet resistance value measured for the electrode with no bending, so the rest of the data points obtained from bending can be compared with this base value. A similar study was done for compression, where nylon and polyester fabrics were compressed as shown in Figure 4.20d to different diameters to record their response as sheet resistance values (Figure 4.20c). Values of sheet resistance calculated after each diameter of bend and compression cycles still remained within the same order of magnitude with only slight variations, showing the stability of the device. Compression tests show the best consistent response as compression of the electrode (4.20d) involves the GNPs flakes to overlap more while bending would stretch out the flakes from each other which would affect the conductivity.

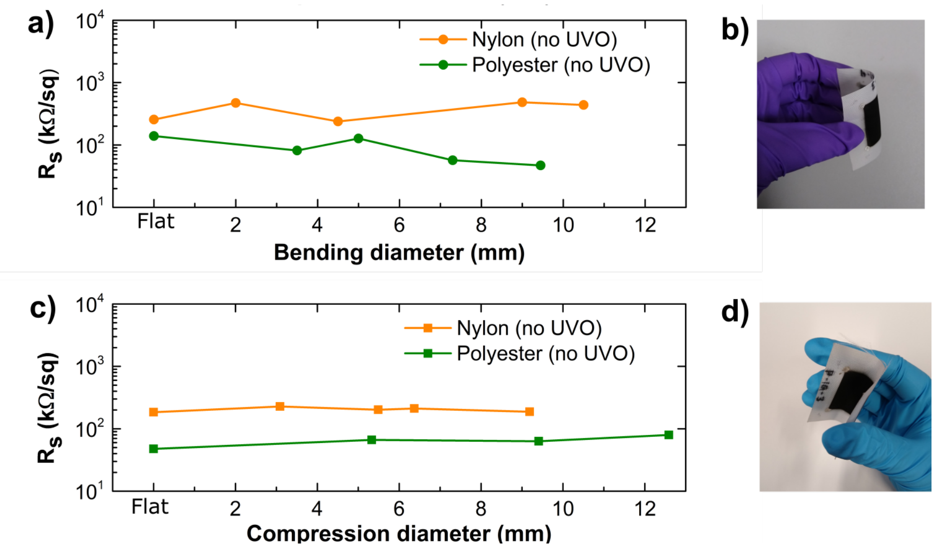

Figure 4.20: Sheet resistance of nylon (orange) and polyester (green) fabrics measured for varying degrees of a) bending (circle) and c) compression (square). The data point corresponding to ’flat’ is the value obtained for no bending/compression. Figure b) shows GNPs coated polyester fabric in a bent position and d) in a compressed position.

Meta-aramid fabrics owing to their rough fabric structure, respond well to UVO surface treatments. Therefore, they were studied further with 5 and 15 minutes of UVO exposure as well (prior to GNPs spray coating). Different bending and compression diameters are followed for each meta-aramid sample and corresponding sheet resistance values are recorded in Figure 4.21.

This shows a stable performance in resistance for meta-aramid fabrics as the resistance stays within the same order of magnitude to different degrees of bending and compression. The slight variation in values can be attributed to the GNPs flakes moving around during the tests. This can be solved by mechanical treatments on the GNPs coated fabrics and also encapsulating them to preserve their properties. In general, a device made of this electrode would have another layer coming on top of these electrodes which can also act as the encapsulation layer. In this work, as these electrodes are used for the fabrication of TENGs with PDMS polymer as a dielectric layer, PDMS will function as the encapsulation for the GNPs coated fabrics.

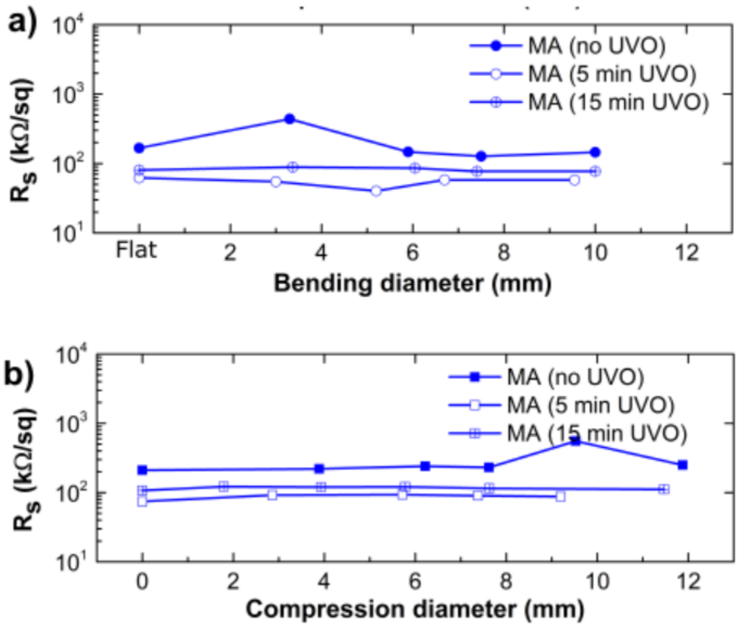

Figure 4.21: Sheet resistance of meta-aramid (blue) fabrics measured for varying degrees of bending (circle) and compression (square). UVO surface treatments are also varied from 0 (no UVO) to 15 minutes of UVO for any possible dependency on their resistance values.

The durability of these textile electrodes was tested by exposing the textile electrodes to continuous cycles of stress and strain by increasing the number of bending and compression cycles. For this, first, nylon and polyester electrodes were tested for their resistance after every 500 cycles of bending and compression cycles up to 2000 cycles, at a fixed diameter of 7 mm (Figure 4.22a). The same study has been extended for meta-aramid fabrics (no UVO, 5 min UVO) repeated bending and compression of electrodes up to 2000 cycles around a 7 mm diameter cylinder (Figure 4.22b). The results obtained for all three fabric electrodes tested this way show consistent performance, indicating the high stability of these textile electrodes towards mechanical deformations of this scale.

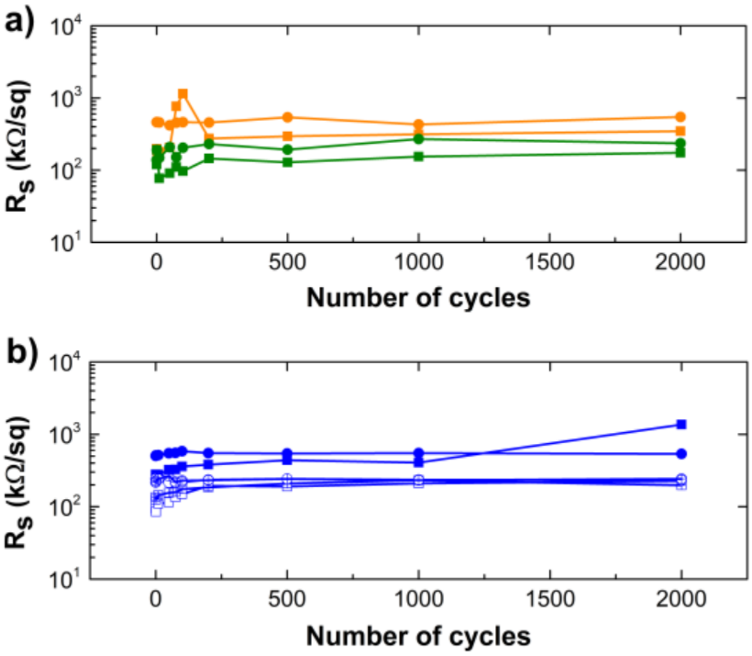

Figure 4.22: a) Nylon (orange) and polyester (green) electrodes bend (solid circle) and compressed (solid square) around a cylinder of 7 mm diameter up to 2000 times and sheet resistance values are recorded after to see their durability as a textile electrode. b) same has been done for meta-aramid fabric and corresponding sheet resistance values are recorded.

Tensile testing

Tensile testing of fabrics involves stretching a fixed dimension of each at a controlled rate and the results are plotted as the force applied to stretch Vs increased stretching in the fabric (in mm). Uncoated, as-received fabrics of 15 cm × 2.5 cm dimension were tested for their tensile strength. To assess if the heat treatment the fabrics endure on a hotplate at 120°C influences their mechanical properties, fabrics were spray coated with just deionised water, in addition to GNPs spray coated fabrics. Figure 4.23 shows the plot of these tested samples until it breaks from the increased tension in both force (kN) Vs displacement (Figure 4.23a) as well as stress Vs strain curve (Figure 4.23b). Stress is calculated by dividing the applied force by the cross-sectional area of the fabric and for strain, the displacement obtained is divided by the initial length of the sample as described in Section 2.4.7. All three samples follow a similar trajectory, with the pure polyester samples following a slightly higher slope towards the end. Pure polyester fabric sample reaches a maximum stress (breaking stress) of 203 MPa before the breaking point at a strain of 0.34, followed by GNPs spray-coated polyester with 181 MPa at a strain of 0.30 and water spray-coated polyester fabric with a breaking stress of 176 MPa at 0.28 strain. This implies that the heating of the fabric at 120°C as a part of the spray coating process does have a slight effect on the tensile strength of the fabric as expected and so does the addition of GNPs on top. A similar tensile strength study conducted by Samanta et al. on pure and rGO-coated polyester fabrics along with their thermal annealing also had similar findings [44].

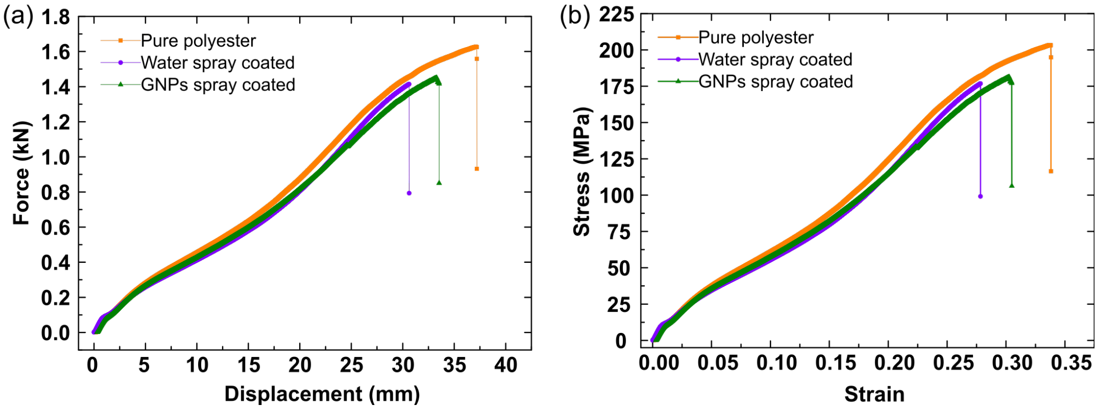

Figure 4.23: Pure (orange, square), water spray coated (purple, circle) and GNPs spray coated (green, triangle) polyester fabrics are tested for their tensile strength with Instron static tensile tester. a) Plot of force applied Vs displacement corresponding to the elongation of the fabric. b) Stress Vs strain plot corresponding to the previous data.

Even though the breaking points of pure, water-spray-coated and GNP-spray-coated polyester are different, they still lie very close. This indicates that the process of spray coating and adhesion of GNPs on the fabric does not significantly alter the mechanical properties of the fabric and most importantly, it does not damage/deteriorate the fabric properties.

4.6 Summary

The aim of this chapter was to fabricate the optimal textile electrode for wearable devices. This includes better adhesion of graphene to fabric substrates and a good range of conductivity without damaging the mechanical strength of fabrics. Two types of graphene suspensions using FLG (few-layer graphene made by liquid phase exfoliation of graphite) and GNPs (graphene nanoplatelets purchased in powder form) were coated on fabrics, following different coating methods such as dip and dry, membrane dip coat and ultrasonic spray coat to select the best graphene suspension and the coating method. This was done based on the surface morphology and conductivity of the coated fabrics. GNPs suspension and ultrasonic spray coating were selected to be the optimal ones for this purpose. Van der Pauw method of sheet resistance test on these coated fabrics gave the resistance to be in the kΩ range. These GNPs-coated fabrics were further analysed with Raman spectroscopy to study the coating on fabrics. An optical profilometer was used to study the thickness produced by the same amount of coating on a flat PET sheet. This study concluded by testing the mechanical properties of the coated fabrics. Being part of a wearable device would introduce a certain level of stress and strain and it is important to test if these devices could withstand it. Various diameters of bending and compression tests were done on these coated fabrics and were able to give a consistent performance along with good tensile strength without deteriorating the inherent fabric properties.

Chapter 5

Characterisation of textile TENGs

5.1 Introduction

In this chapter, the structure and electrical characterisation of triboelectric nanogenerators (TENGs) made from the previously explained textile electrodes are discussed. Different parameters affecting the TENG outputs such as frequency, the distance of separation, contact area, contact force and chemical modifications of tribolayers are studied in detail along with different tests to study the stability of these devices under different conditions. The work discussed in this chapter is in preparation towards publication.

5.2 Architecture of TENG device

TENG devices fabricated here are of the double electrode structure, they comprise two sides, each with a dielectric tribolayer and an electrode layer as illustrated in Figure 5.1a. They are characterised by the vertical contact separation mode of operation, where the tribolayers face each other with the electrode layers behind them. In this work, each TENG is referred to as two parts, the PDMS side and the test side, making a PDMS-test TENG device. The architecture of the PDMS side and structure of PDMS-nitrile TENG is shown in Figure 5.1. PDMS side (Figure 5.1b) has PDMS acting as the dielectric tribolayer and GNPs coated fabric as the electrode. The other side is named the test side, as the testing material was varied (eg: nylon fabric, nitrile rubber etc.) with double-sided copper tape as the electrode.

These TENG devices are tested by mounting the PDMS side on the moving stage of the characterisation set-up (as shown in Section 3.4.7) while the test side is mounted on the stationary right side stage. The PDMS side is made to come in successive contact and separation cycles with the test side (nitrile in

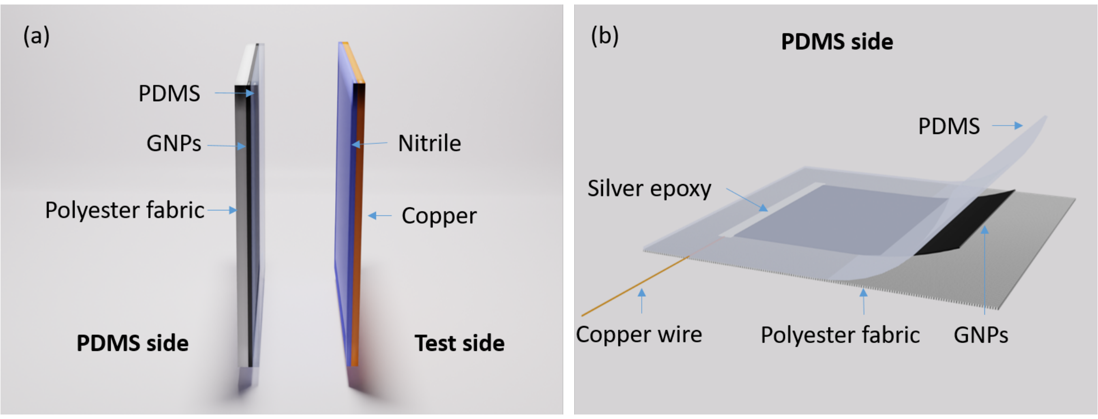

Figure 5.1: Schematic diagrams showing the structure of a) complete double electrode TENG with PDMS side facing test side of nitrile and copper electrode in vertical contact separation mode of characterisation and b) PDMS side of TENG demonstrating different layers.

Figure 5.1a) to generate an electrical response. The factors studied in this mode are contacting force (force produced by the moving PDMS side on the test side upon contact), maximum separation distance (maximum distance achieved between the two tribolayers during the separation stage of the cycle), frequency of contact and separation (number of contacts and separation cycles occurring per second), contact area (area of contact between the two tribolayers) and the effect of chemical modification on the PDMS surface towards enhancing the TENG outputs generated.

5.3 PDMS side morphology

The PDMS side of the TENGs was fabricated using the GNPs-coated polyester textile electrodes following the steps discussed in Section 3.3.1. This PDMS side was studied under SEM at each step of its fabrication (shown in Figure 5.2) starting from pure polyester fabric, GNPs coated fabric to final PDMS spin coating on top. Changes to their surface morphology, as well as cross-section at each stage, are studied. It can be noted that the GNPs coating on top of the polyester fabric (Figure 5.2b) did not alter the surface structure of the fabric as it still preserves the same morphology as pure polyester shown in Figure 5.2a. PDMS spin coating on top of this GNPs coating has made the surface of the fabric homogeneous covering its roughness (Figure 5.2c, 5.2f). The lines seen on the plane of PDMS surface (Figure 5.2c) occur as a result of the curing process required to dry the wet PDMS polymer. They arise mainly from the shrinkage of PDMS after curing due to the thermal contractions occurring in the material and it depends mainly on the curing temperature followed [66]. Factors including mixing ratio of polymers, interaction with the substrate, stiffness and thickness of the substrate can also induce stress in the polymer films to form cracks as seen in the case of PDMS here [67].

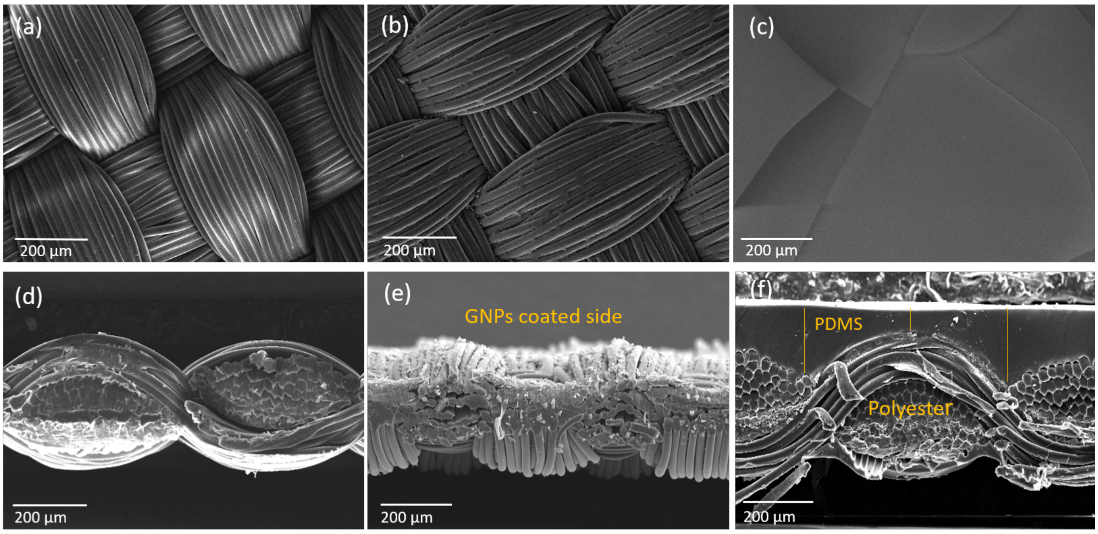

Figure 5.2: SEM images of PDMS side of TENG at each step of fabrication with a) pure polyester, b) GNPs spray coated stage and c) PDMS polymer spin-coated on top. Cross-section views of each stage are also shown in d), e) and f) respectively.

Cross-section images of these stages can be seen on the bottom row of Figure 5.2, with pure polyester fabric (Figure 5.2d), GNPs spray coated fabric (Figure 5.2e) and PDMS spin-coated on top (Figure 5.2f). It is also clear from the cross-section images that the GNPs coating is thin and it closely follows the fabric roughness. The thicker PDMS layer on top of this structure results in a planar surface at the top, leaving the thickness to vary from 43 to 170 μm following the weaving pattern of fabric (Figure 5.3a). This thickness range corresponds to PDMS spin coating at 9 rps rotation for 30 seconds. However, the PDMS spin coating step involved measuring the weight of elastomer to cross polymer in a 10:1 ratio, pouring the degassed PDMS on top of the fabric to cover the entire surface before the spinning (static spin coating), timing the spinning at 9rps for 30 seconds manually etc., all these factors can affect the thickness of PDMS coating produced. Two fabrics spin-coated with PDMS polymer following the same procedures including 10:1 mixing ratio and 9 rps, 30 seconds spinning speed are shown in Appendix C. They showed a variation of 103 μm in minimum and 46 μm in maximum thickness of the PDMS layer, following the features of the fabric surface. This is really significant change as the thickness of the PDMS tribolayer affects the output produced by the TENG device [68]. The same parameters were tested for PDMS spin coating on PET sheets as well to compare the thickness of PDMS coating obtained on a planar substrate. The same rotation speed and time repeated for PDMS on top of PET sheet gives an average consistent thickness of 435 μm as shown in Figure 5.3. This shows the difference in thickness produced for the same spinning speed due to the roughness of the substrate and the interaction of PDMS with the substrate as well. Therefore one of the main factors affecting the consistency in response from similar TENG devices is going to be the variation in PDMS layer thickness.

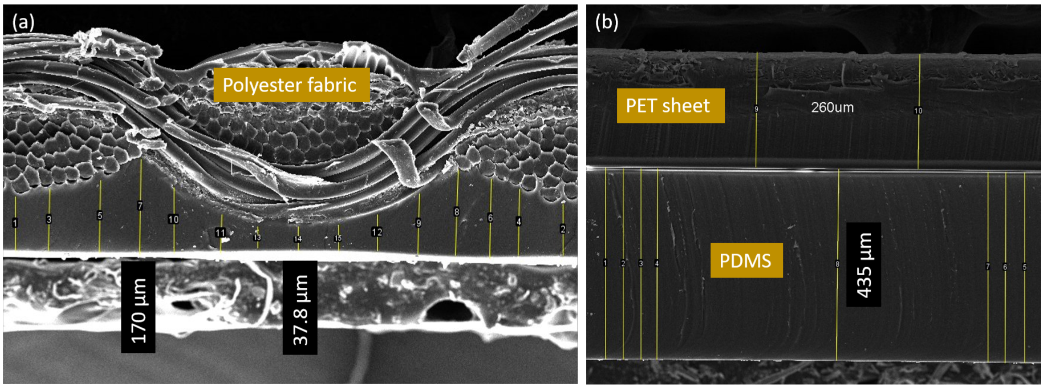

Figure 5.3: SEM images of PDMS spin coated at 9 rps for 30 s on a) polyester fabric and b) PET sheet. PDMS coating on polyester follows the roughness of the fabric surface (shown with the yellow lines of PDMS thickness) with a minimum of 38 μm to maximum of 170 μm. PET sheet with a thickness of 0.25 mm, has a uniform PDMS thickness of 435 μm.

5.4 TENG Output

The typical outputs recorded for TENG characterisation are open circuit voltage (V_{OC}), short-circuit current (I_{SC}) and short-circuit charge (Q_{SC}), described in detail in Section 2.3.4. For different parameters and stability tests conducted on these TENG devices, responses are generally recorded in terms of voltage and current outputs after running the contact-separation cycles for 3000 times. This is done as the surface charge density takes several contact-separation cycles to saturate and reach a stable value [69]. So every TENG measurement studied here is taken after saturating the device with a high number of contact-separation cycles (3000 here), to obtain stable and comparable results. They are recorded with the help of Excelinx software and each measurement was timed for 20 seconds manually. 10 consecutive peak points of this AC outputs from a stable part are then considered for each plot to obtain the average value for that measurement. Different factors involved in this measurement which can affect/enhance the output such as chemical modification of tribolayer, frequency of their contact and separation, area in contact and the maximum distance of separation between them are studied separately. Figure 5.4 shows a typical TENG output for a 3 cm × 3 cm, PDMS-nitrile TENG at a fixed frequency of 3 Hz, contacting force of 35 N and maximum separation distance of 4 mm. This output shows an average V_{OC} of 140 V, I_{SC} of 2.5 μA and Q_{SC} of 62 nC.

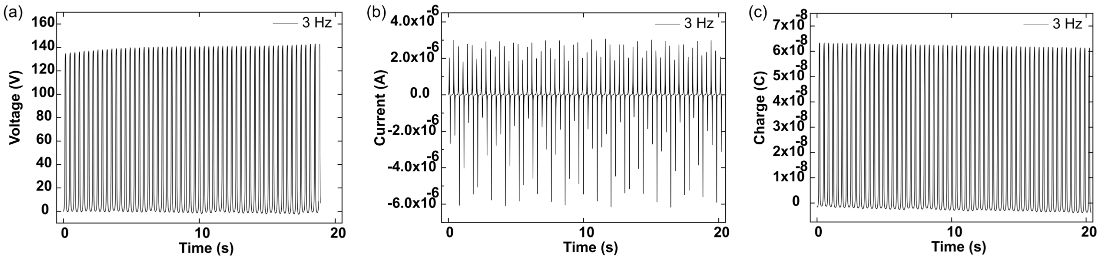

Figure 5.4: Typical TENG outputs of a) V_{OC}, b) I_{SC} and c) Q_{SC} obtained from PDMS-nitrile TENG measured at 3 Hz frequency, 2 mm amplitude of separation distance and 35 N contacting force.

As a part of experimental error analysis, the PDMS-nylon TENG was tested on 5 different days which had a humidity ranging between 26 to 44% and room temperature ranging from 20.4 to 24.3 °C. This produced an average open circuit voltage of 151 ±7 V and a short circuit current of 3.7 ±0.3 μA. This shows the variation in output that can be expected from these TENG devices depending on the ambient conditions at the time of measurement. This can also be contributed by the slight variation in angular position between the left and right-hand side sample holders carrying the PDMS and test sides of the TENG. As seen in the TENG characterisation set-up in Figure 3.16, the right side sample holder is connected to the load cell which is positioned on a vertical metal plate with a screw at the back. Tightening or loosening the screw slightly can change the load cell (and connected right-hand side sample holder) angle relative to the left-side sample holder. This slight change in the angle of contact between the two sides can affect the output generation significantly. The dependency of the angle of contact on TENG outputs studied in detail can be found here [70]. This study showed that even a change of 0.5° in angle of contact can change the voltage and current outputs by 33% and 56% respectively.

5.5 Triboseries

In a triboseries, materials are listed from ones with more tendency to lose electrons at the top to ones with more tendency to gain electrons at the bottom. i.e. materials at the top of the series are more electropositive than ones at the bottom which are more electronegative in nature. In order to enhance the output of a TENG, materials should be chosen from the far ends of the triboseries, which would create a high charge transfer between them on contact.

The PDMS polymer used as one of the dielectrics here is a strong electronegative material, listed at the bottom of the triboseries. This PDMS side fabricated here is tested against a variety of materials, including different types of fabrics, with a copper electrode as the test side. All the TENGs tested are of 3 cm × 3 cm dimension. Based on the short-circuit charge outputs obtained by their pairing, all tested materials are ordered in the form of a triboseries in Figure 5.5. The triboelectric charge density obtained for each pairing is listed on the left side of the figure in $\mu C/m^2$. Out of the outputs obtained from all the tested materials, nylon fabric and nitrile rubber produced the maximum values of 94 and 66 $\mu C/m^2$ respectively against PDMS. This can be explained in terms of the electron affinity of these materials as they are highly electropositive in nature. Here the tested materials can not be compared directly as they are not all of the same thickness. From here onwards for different studies we will be using nylon and nitrile materials on the test side. Nylon material has a similar electron affinity as the skin [71] which would provide a good comparison for the PDMS side against the skin in a wearable device. The TENG devices with nylon and nitrile test sides would be mentioned as PDMS-nylon TENG and PDMS-nitrile TENG respectively.

5.6 Power characterisation

The internal resistance of a TENG device can be characterised by connecting loads of varying resistance as shown in the schematic circuit of Figure 5.6a. The resistance (Z_{load}) at which the TENG device produces the optimum power output matches the internal impedance (Z_{i}) of the TENG device. In order to calculate the optimum power output of a PDMS-nylon TENG, this device was connected with resistors of 2 MΩ to 10 GΩ range in series between the TENG probes and Keithley 6514 source meter, and current outputs corresponding to each value of resistance were recorded. For this, resistors were arranged on

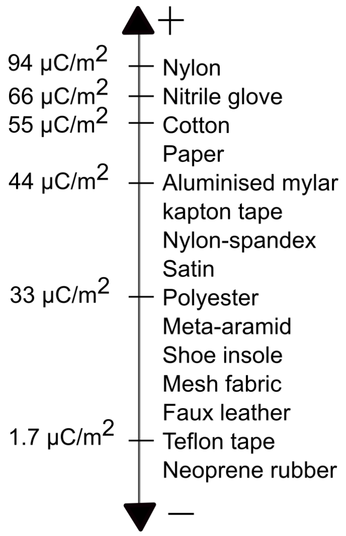

Figure 5.5: Different materials tested against the PDMS side are listed on the basis of their triboelectric charge density. Test side materials are shown from most electropositive at the top to most electronegative at the bottom.

a breadboard and TENG and Keithley probes were connected to each end of the resistor and the corresponding current output was recorded for 10 seconds before moving the probes to the next resistor. The process is repeated for all resistors, up to 10 GΩ. The average current output corresponding to each resistor was then calculated and plotted in Figure 5.6b (black, solid square). As the resistance increases, the current decreases giving the highest current response for the lowest 2 MΩ resistance and then decreasing all the way down as resistance increased to 10 GΩ. These current (I) and resistance (R) values corresponding to each data point were used to calculate the instant power by calculating I^2R to obtain the power curve shown in Figure 5.6b (green, solid circles). The power reaches its maximum at 330 mW/m^2 at 60 MΩ resistance which would be the internal resistance of the PDMS-nylon TENG device tested here.

5.7 Parameters of TENG output

In this section, different parameters affecting the TENG outputs are studied in detail with the aim of enhancing the TENG performance. These parameters include chemical modification of the PDMS side, frequency of contact and separation cycle, area of contact, maximum separation distance and contacting force between the tribolayers. Their responses are recorded in terms of voltage and current outputs.

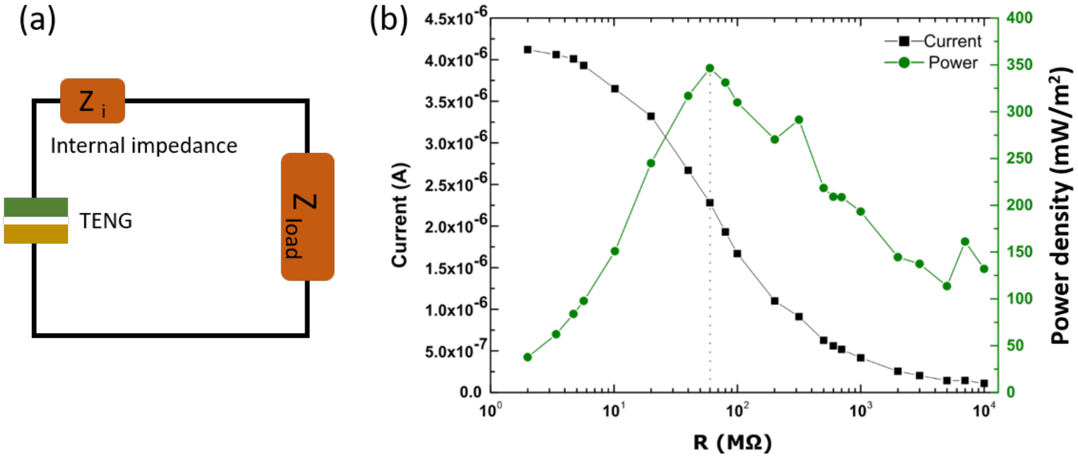

Figure 5.6: A PDMS nylon TENG is connected to varying load resistors of values ranging from 2 MΩ to 10 GΩ and corresponding current outputs are recorded. a) Schematic diagram of the circuit. b) Black (solid square) curve shows the average current value obtained for each resistor value and instant power corresponding to the values is calculated and plotted as the green (solid circle) curve in the figure giving a maximum power output of 330 mW/m^2 at 60 MΩ resistance.

5.7.1 Fluorination study

It is known that the fluorination process of the PDMS surface can enhance the electron affinity of the PDMS material [72]. The PDMS side of a PDMS-nylon TENG was fluorinated with an SF_6 gas plasma to enhance the electron affinity of the PDMS layer. In this way, by creating a larger gap in electron affinity between the two tribolayers, the charge generation on contact will be enhanced, producing larger voltage and current outputs. The effect of this chemical modification is studied at both 1 Hz and 3 Hz frequencies and the outputs are recorded before and after the fluorination process for comparison. SEM was used to study the PDMS surface for any changes, such as etching, occurring as a result of the SF_6 exposure at the μm scale. Figure 5.7 shows the SEM images before and after fluorination at two different scales with no physical changes observed. Lines seen on the PDMS surface occur as a result of thermal contractions as explained in Section 5.3 of this chapter.

Figure 5.8 shows the voltage and current outputs obtained for PDMS-nylon TENG before (a,b) and after fluorinating (c,d) the PDMS layer. The voltage is raised from an average of 140 before RIE to 356 V after RIE, by 154%. The current output increased from 1.1 to 2.5 μA, by 127%.

The same study was repeated at 3 Hz frequency as well as shown in Figure 5.9 to confirm the effects of fluorination. Here as well, the voltage output has been raised from 140 to 355 V, the same as in the abovementioned 1 Hz

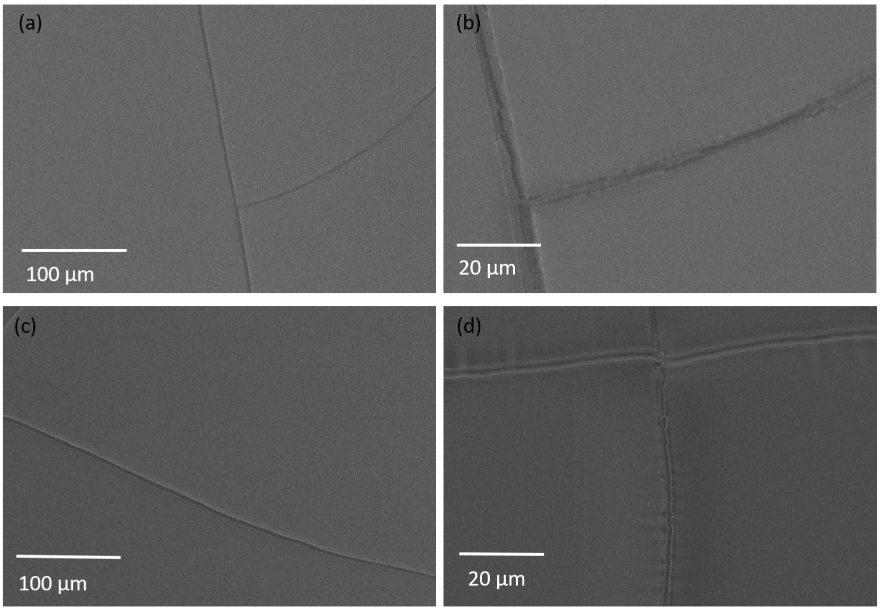

Figure 5.7: SEM images of PDMS surface before and after SF_6 fluorination. a) and b) show the surface before fluorination at two different magnifications while c) and d) show the same after. No physical changes can be seen on the micrometre scale.

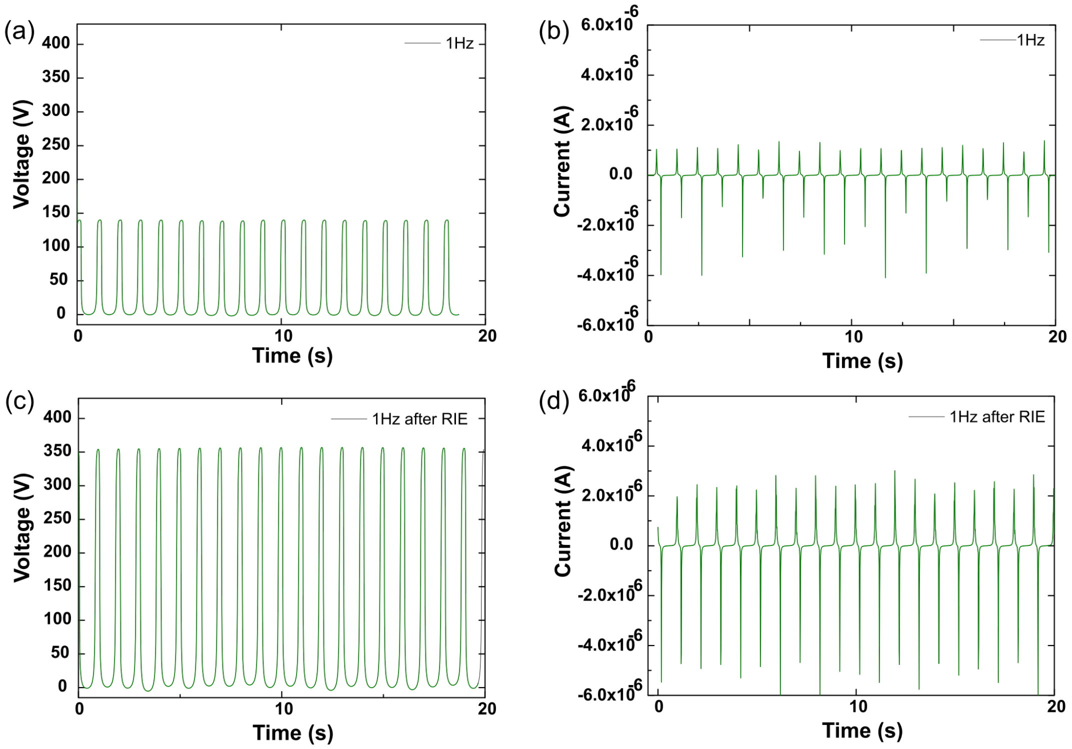

Figure 5.8: PDMS-Nylon TENG measured at 1 Hz frequency before and after fluorinating the PDMS layer with SF_6 gas plasma.

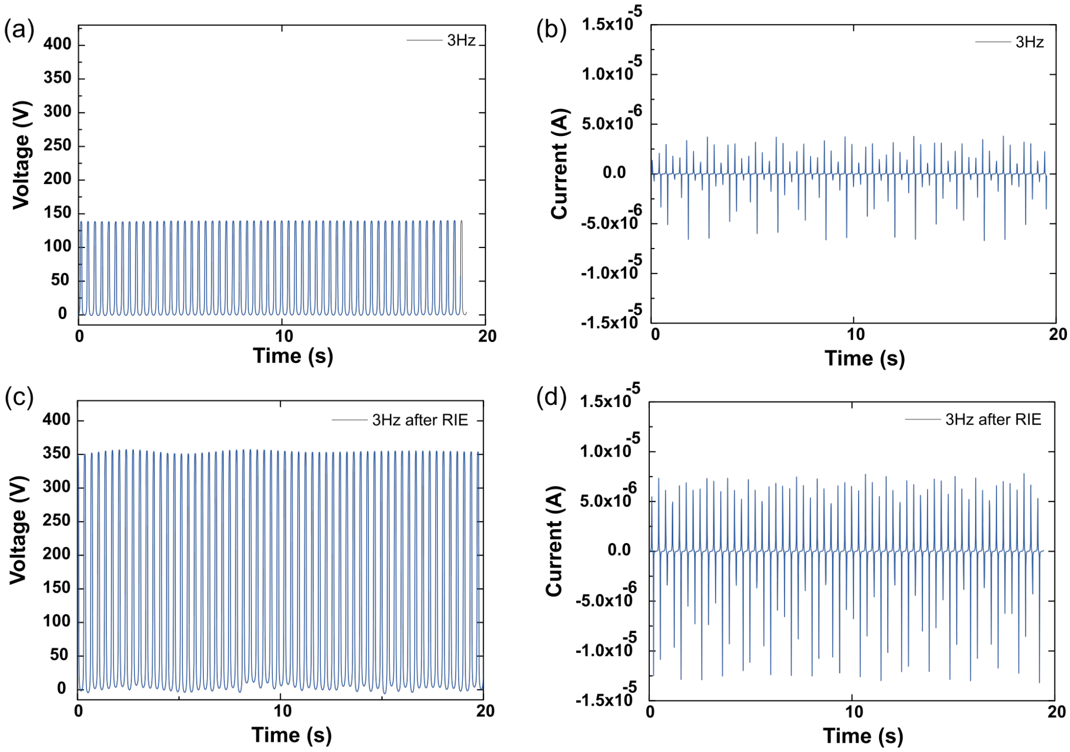

Figure 5.9: PDMS-Nylon TENG measured at 3 Hz frequency before and after fluorinating the PDMS layer with SF_6 gas plasma.

study, while the current increased from an average of 2.4 before RIE to 6.5 μA after RIE, by 170%. This study also shows that the current output depends on frequency, while voltage remains unaffected by it. This current-frequency dependency is studied in detail separately in the next section. This result verifies the effect of the difference in electron affinity between dielectric materials on the TENG output.

5.7.2 Frequency study

Mechanical energy harvesting from human body movements is going to be of low, irregular frequencies. Therefore, it is important to study the dependency of TENG outputs on a varied range of frequencies. Here, the frequency of contact and separation between the two tribolayers of the TENG was varied from 0.5 to 4 Hz at an increment of 0.5 Hz in order to study the effect of frequency on current output. Voltage outputs are not recorded as they do not change with frequency, as discussed in the previous section. The measurement of TENG output at each frequency was timed for 20 seconds manually. Here a PDMS-nitrile TENG is used at a fixed contacting force of 35 N and maximum separation distance of 4 mm. Figure 5.10 shows the corresponding plots obtained for each increment in frequency and the average values are shown in table 5.1. These results show a clear increase in current output obtained corresponding to the increased frequency with a maximum of 7.3 μA at 4 Hz frequency. This occurs due to the increased charge generation per time as a result of the increased frequency of contact. Values above 4 Hz are not followed, as they lie outside the range of wearable applications intended for this study. For context, the average human walking frequency ranges from 1.8 to 2Hz [73] while exercising could reach up to 3.5 Hz [74].

Table 5.1: Shows the average value of current output obtained for each frequency increment.

Frequency (Hz)	0.5	1	1.5	2	2.5	3	3.5	4
Current (μA)	1.6	2.8	3.7	4.4	4.5	4.8	5.9	7.3

5.7.3 Separation distance study

The separation step in the contact-separation mode of TENG operation is what causes the charge flow between the electrodes. Therefore it is important to understand and quantify this process. In one cycle of contact and separation, the separation distance varies from zero (in contact) and gradually increases up to the set maximum distance of separation before approaching contact again. Here, this set maximum separation distance between the two tribolayers of a PDMS-nylon TENG was increased from 4 mm (2 mm amplitude of separation distance) to 8 and 10 mm, as shown in Figure 5.11. Voltage and current outputs corresponding to each measurement were recorded (Figure 5.12). This shows the direct proportionality of TENG outputs to the increased maximum separation distance. The average values obtained for each measurement were calculated from this plot and are shown in table 5.2. It can be seen that the outputs have still not reached their maximum throughout the measurements, as setting the separation distance to 12 mm went above the voltage limit of -210 to 210 V range available to the Keithley 6514 source meter used.

5.7.4 Contact area study

The area of contact between the two tribolayers directly relates to the charge transfer between the sides. In order to quantify this, a PDMS-nitrile TENG

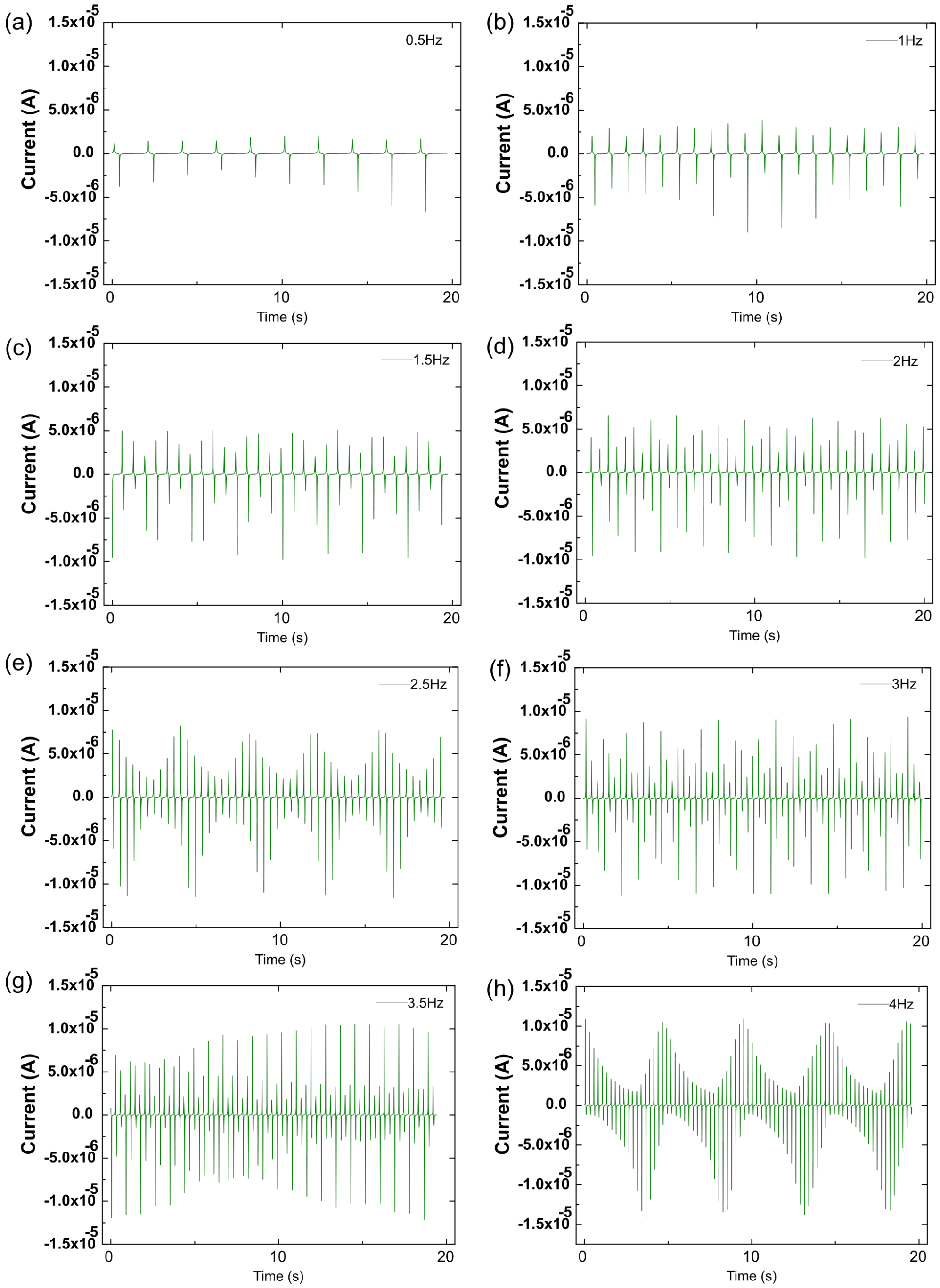

Figure 5.10: Current output as a function of time for increasing contact-separation frequency for a PDMS-nitrile TENG: a) 0.5 Hz, b) 1 Hz, c) 1.5 Hz, d) 2 Hz, e) 2.5 Hz, f) 3 Hz, g) 3.5 Hz, h) 4 Hz.

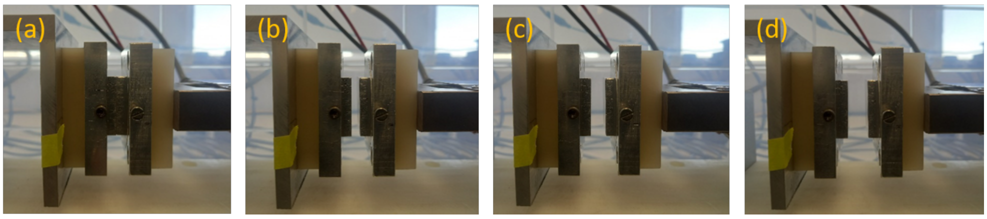

Figure 5.11: Pictures of sample holders at different separation distances of a) 0 mm (in contact), b) 4 mm, c) 8 mm and d) 10 mm. Sample holders are shown without the PDMS and test side mounted.

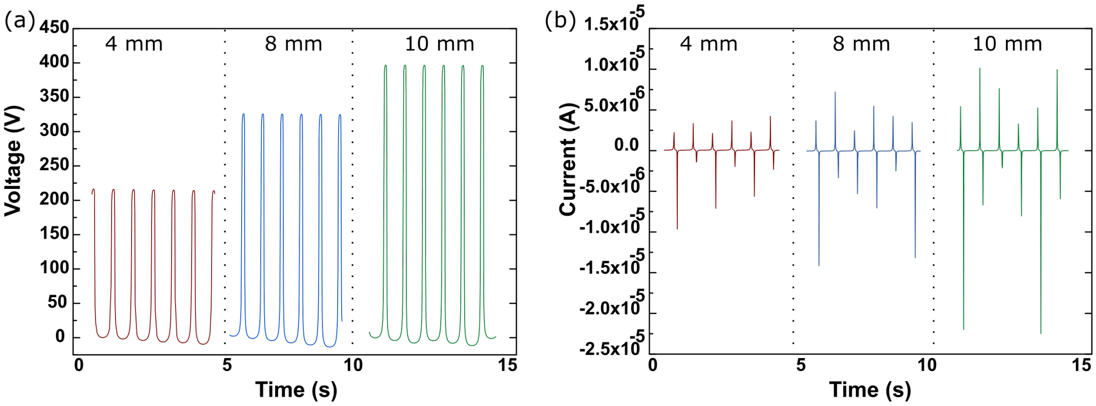

Figure 5.12: Voltage (left) and current (right) outputs of a PDMS-nylon TENG at increasing distances from 4 to 10 mm.

Table 5.2: Shows the average voltage and current output obtained for a PDMS-nylon TENG at varying maximum separation distances from 4 to 12 mm.

Separation distance (mm)	Voltage(V)	Current(μA)
4	215.65	3.09
8	325.34	4.57
10	396.66	6.84
12	above 420V	7.66

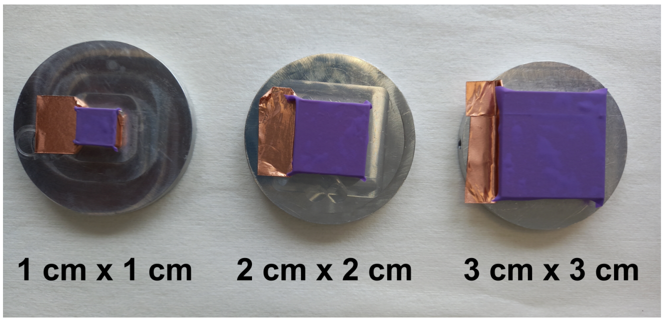

Figure 5.13: Sample holders of different dimensions with test side of copper electrode and nitrile rubber on top to quantify the effect of contact area on the output of PDMS-nitrile TENG.

was characterised by varying the area of nitrile material that comes in contact with the PDMS side. For this, the PDMS side was kept at the same 3 cm × 3 cm dimension, while the nitrile side was cut in 1 cm × 1 cm, 2 cm × 2 cm and 3 cm × 3 cm dimensions for each measurement to fit the sample holders of the same size, as shown in Figure 5.13. The measurements were done at a fixed contacting force, separation distance and frequency. The results obtained are shown in Figure 5.14, showing the clear increase in the response of voltage and current outputs to the increased area of contact. On average, 23 V, 0.36 μA outputs obtained for 1 cm × 1 cm area of contact were raised to 41 V, 0.72 μA for twice the area of 2 cm × 2 cm dimension, increase of 78% in V_{OC} and 100% in I_{SC}. Area of contact of 3 cm × 3 cm followed for all other studies throughout this chapter were measured to obtain an average voltage of 123 V and a current of 1.9 μA, 435% increase in V_{SC} and 428% in I_{SC} compared to the 1 cm × 1cm area of contact.

For applications where the dimension of the device needs to be kept a certain size, an increase in contact area can be achieved by physical modifications to the tribolayer such as micro / nano-patterning. Adding geometrical patterns by lithography [75], nanostructures by plasma etching [72] etc. to the tribolayer can enhance the effective contact area between the tribolayers, thus enhancing the TENG output.

5.7.5 Contacting force study

The final parameter studied for understanding the TENG output generation is the force applied between the tribolayers on contact. Since the PDMS side of TENG is mounted on a moving stage and the test side is kept stationary, a

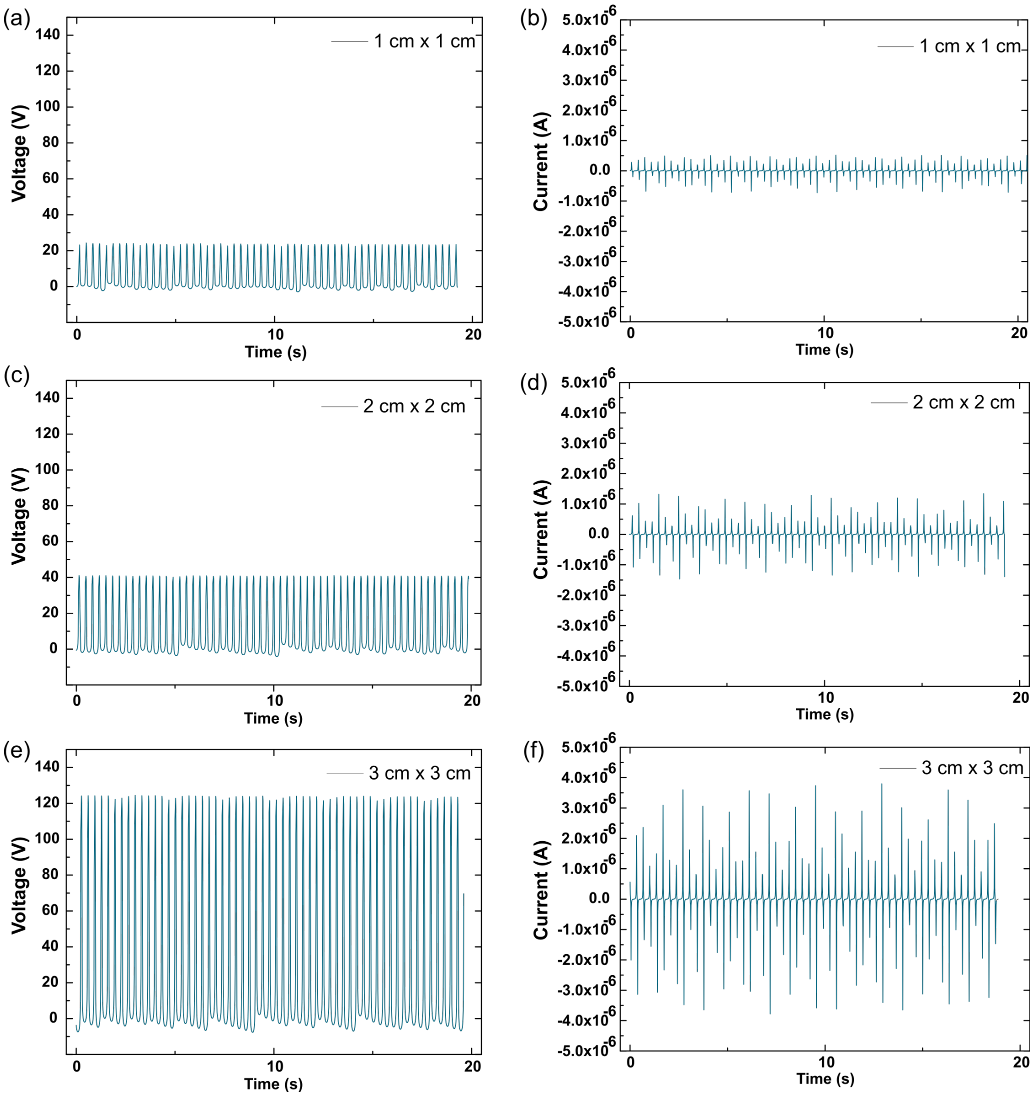

Figure 5.14: Votage (left) and current (right) outputs for 1 cm × 1 cm (a and b); 2 cm × 2 cm (c and d); and 3 cm × 3 cm nitrile area on the test side of a PDMS-nitrile TENG.

load cell equipped behind the test side can be used to monitor the force on contact between the two sides. This setup is shown in Figure 5.15. This applied force was changed from approximately 30 N to 60 N in increments, and the corresponding voltage and current outputs from a PDMS-nitrile TENG were recorded. Figure 5.16 shows the increased outputs obtained for increased contacting force at a fixed separation distance of 4 mm and 3 Hz frequency. This occurs as lower contacting forces have reduced the area of contact between the tribolayers. As contacting force is increased, the elasticity of PDMS material would allow more deformation, enhancing the area of contact with the tribolayer on the test side (nitrile). As discussed in Section 5.7.4, this would lead to increased output. It is seen from Figure 5.17 that the average current value calculated had a linear response to contacting force. This suggests that these TENG devices can also be used as self-powered pressure sensors in addition to their application as energy harvesting devices.

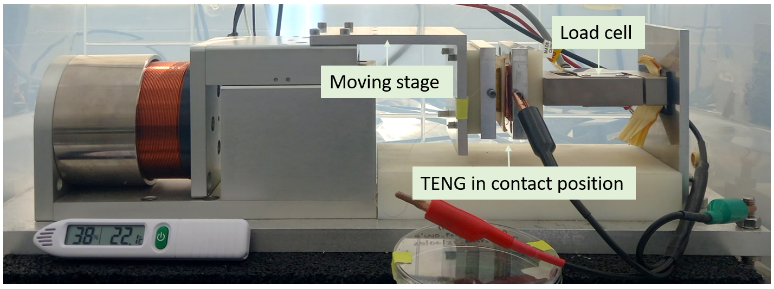

Figure 5.15: TENG characterisation set-up to measure the contacting force between the tribolayers. The moving stage carries the PDMS side which comes in contact with the stationary test side on the right-hand side. Here they are shown in the contact position of the contact-separation cycle. The load cell shown behind the test side measures the force applied on contact. Parameters in the Galil software corresponding to 30 to 60 N force applied are then set to measure the TENG outputs at each applied force.

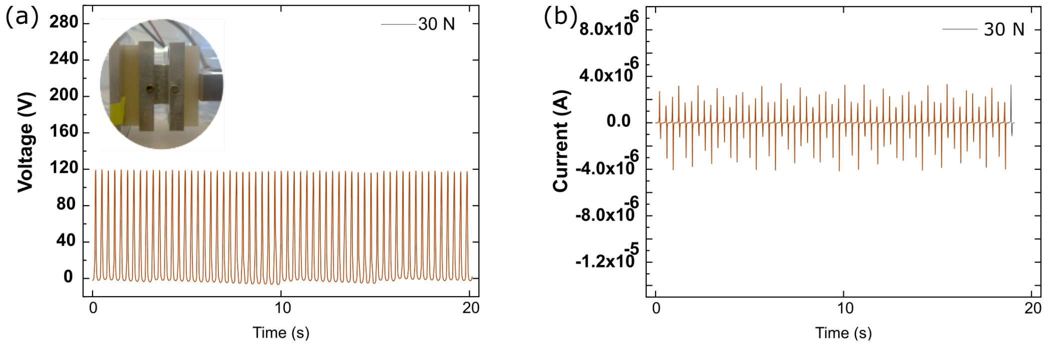

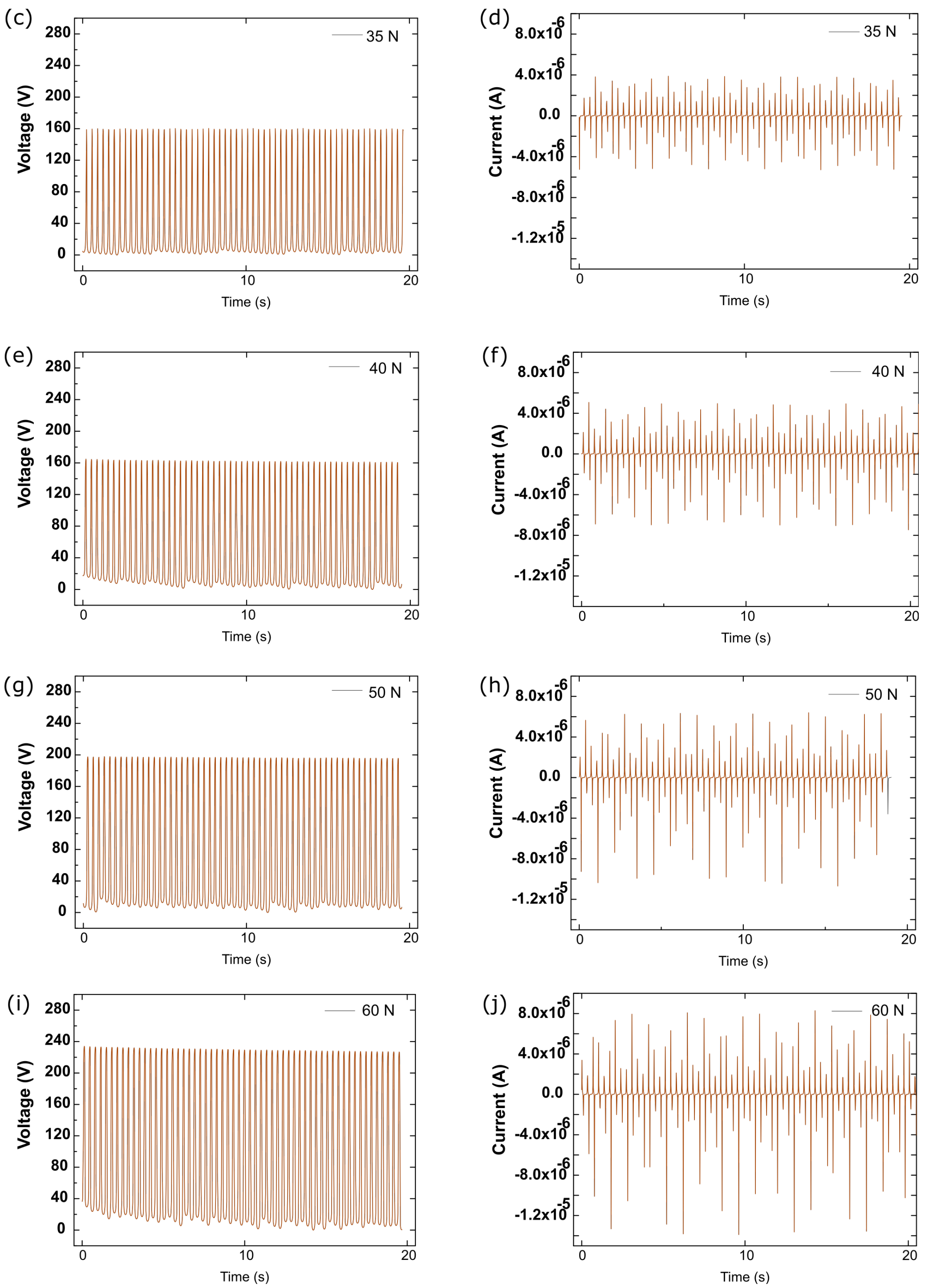

Figure 5.16: Voltage (left) and current (right) as a function of time for increasing applied force for a PDMS-nitrile TENG device in contact-separation: a) and b) 30 N; c) and d) 35 N; e) and f) 40 N; g) and h) 50 N; i) and j) 60 N.

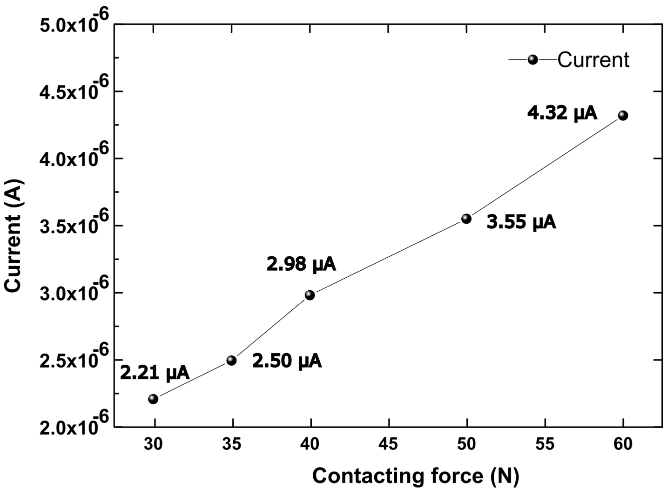

Figure 5.17: Average current value of a PDMS-nitrile TENG plotted against corresponding contacting force showing their linear relation.

5.8 Stability of TENG devices

Keeping in mind that these textile TENG devices are intended for wearable applications where they could be part of clothing, depending on the location of the device, such as elbows, knees etc., they would undergo different degrees of mechanical deformations such as bending, stretching etc. as well as exposure to sweat and rain. This means these devices need to be tested for conditions outside the standard and ambient conditions as before. Textile electrodes used for TENG fabrication were already characterised separately for their mechanical strength with various bent and compression cycles as well as for tensile strength in Section 4.5.5. They demonstrated good resilience to different degrees of stress and strain.

In this section, the TENG devices were tested outside ambient conditions of humidity and with ionised air as well as the device response once the exposure is removed and brought back to ambient conditions. They were also tested for their response to various bending tests. Some of the TENG devices fabricated here were repeatedly used for over a year to study different factors involved in TENG outputs as discussed in the sections above. This is an additional measure of the durability of these devices.

5.8.1 Humidity

Water compatibility of these TENG devices was tested here in a high-humidity environment. For this, the TENG characterisation set-up was enclosed in an

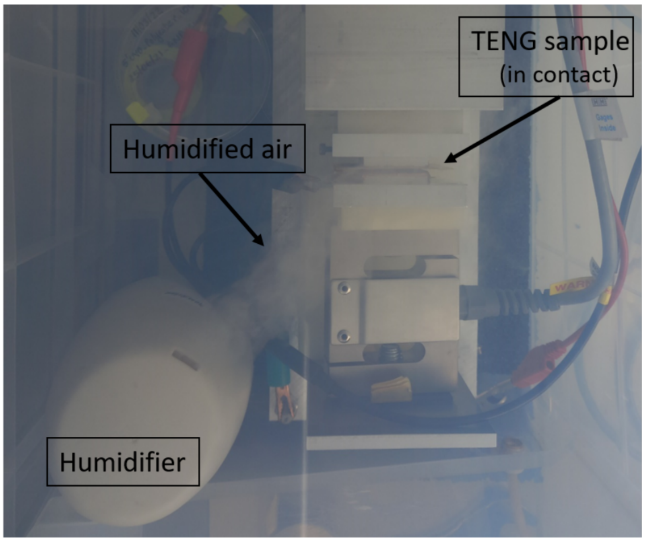

Figure 5.18: Experimental set-up used to measure the response of TENG devices to humidity. A room humidifier is kept on next to the TENG characterisation set-up enclosed inside an air-tight box. A humidity sensor is kept inside the box to monitor the humidity levels.

airtight box with a room humidifier and a humidity sensor inside. This enclosure also has nitrogen gas flow fitted to bring the humidity levels down. Figure 5.18 shows the experimental set-up used for the humidity study. A PDMS-nitrile TENG was tested at contact separation cycles of 3 Hz frequency and 4 mm maximum separation distance inside this set-up. For the first part, humidity inside the box was raised to 70% and gradually reduced in steps of 10% down to around 20% and measurements were made at each step. It should be noted that the humidity percentage mentioned is variable by $\pm$ 3% (For example, 50% would be 50% $\pm$ 3%) as it is difficult to maintain the exact humidity by manually controlling the nitrogen flow to the enclosure. Results obtained from this study are shown in Figure 5.19. It is seen from the results that the TENG device had a stable performance throughout the range of 20 to 60% and displayed a drop in performance at 70% humidity. This shows the ability of these devices to withstand a wide range of humidity conditions.

For the second part, the humidifier was kept switched on for 30 minutes facing the TENG device as shown in Figure 5.18. This resulted in more than 90% humidity recorded inside the box and water mists was seen to be settling onto the PDMS surface. Outputs recorded at this stage of high humidity significantly reduced the electrical outputs from the PDMS-nitrile TENG much like the 70% study recorded previously. This is due to the formation of a thin layer of water between the dielectric surfaces inhibiting the charge generation

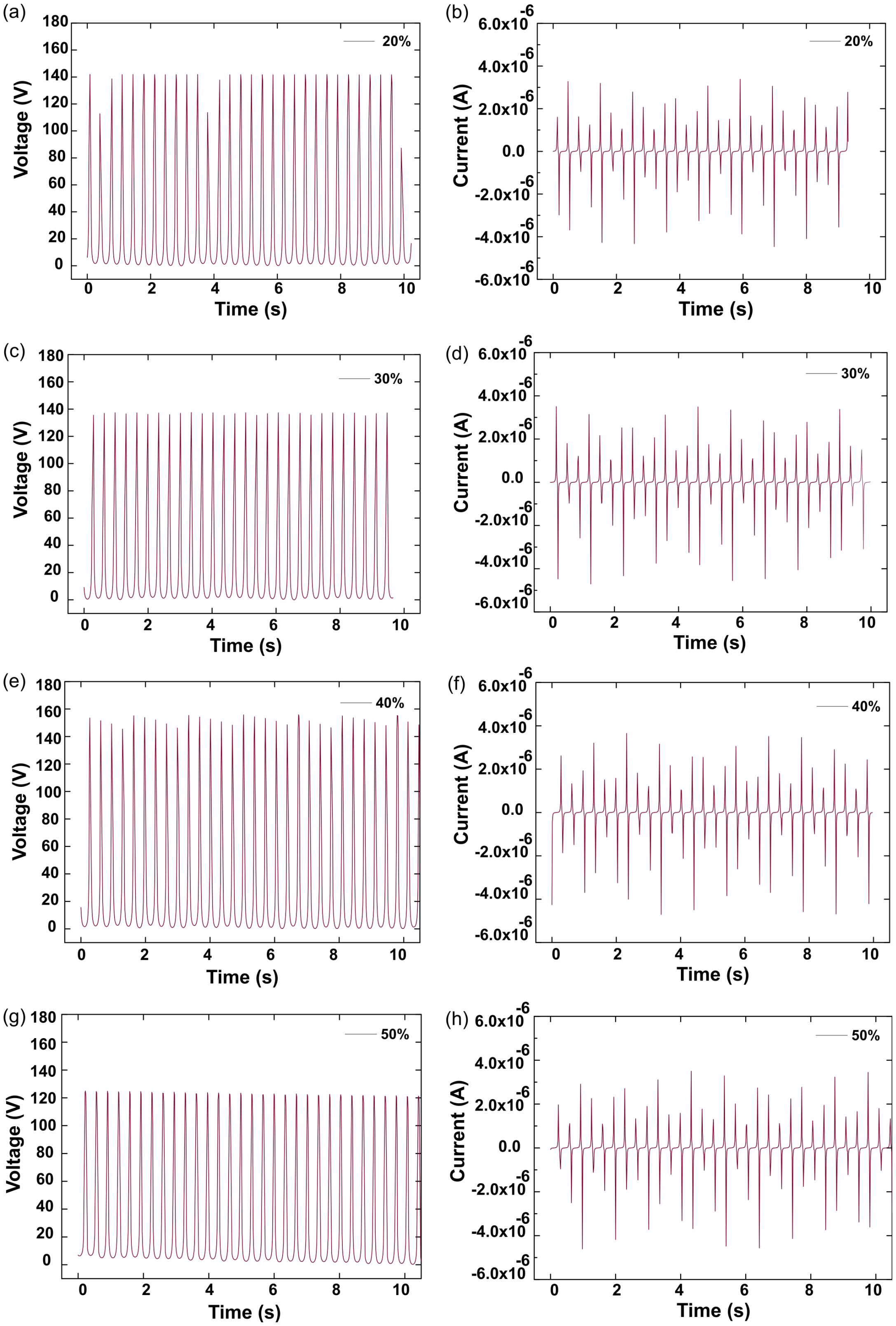
(a)
Voltage (V)
0, 20, 40, 60, 80, 100, 120, 140, 160, 180
Time (s)
0, 2, 4, 6, 8, 10
20%
(b)
Current (A)
-6.0x10^-6, -4.0x10^-6, -2.0x10^-6, 0.0, 2.0x10^-6, 4.0x10^-6, 6.0x10^-6
Time (s)
20%
(c)
Voltage (V)
Time (s)
30%
(d)
Current (A)
Time (s)
30%
(e)
Voltage (V)
Time (s)
40%
(f)
Current (A)
Time (s)
40%
(g)
Voltage (V)
Time (s)
50%
(h)
Current (A)
Time (s)
50%

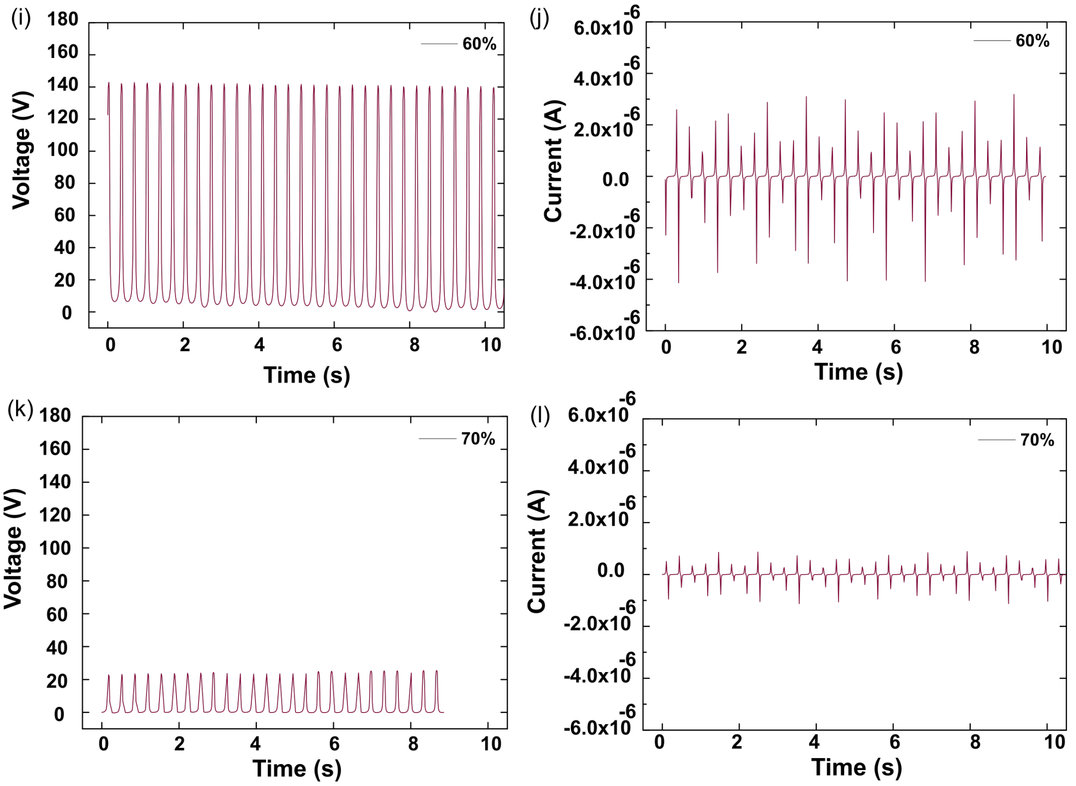

Figure 5.19: Voltage and current outputs of PDMS-nitrile TENG under humidity levels ranging from a),b) 20%, c),d) 30%, e),f) 40%, g),h) 50%, i),j) 60% and k),l) 70%.

process of TENG. After 30 minutes, the humidifier was switched off and the humidity levels were allowed to fall back to the ambient level. The device was then tested again to see if the output after this high level of humidity would match up with the response from before, i.e. the ability of the TENG to recover from a highly humid environment. Figure 5.20 shows the PDMS-nitrile TENG outputs before and after this prolonged exposure. Even though the outputs recorded after the humidity test gives a slightly higher response of 140 V and 2.6 μA compared to the previous 119 V and 2.2 μA, it is still within the experimental error range recorded for the TENG characterisation.

5.8.2 Ionised air

The response of a PDMS-nitrile TENG device to an ionised atmosphere was also tested here to study its effect on the charge generation process of the TENG. For this, a local air ioniser device was kept switched on near (8 cm away) the TENG device as shown in Figure 5.21a and TENG outputs were recorded at different intervals of time. Figure 5.21b shows the average voltage

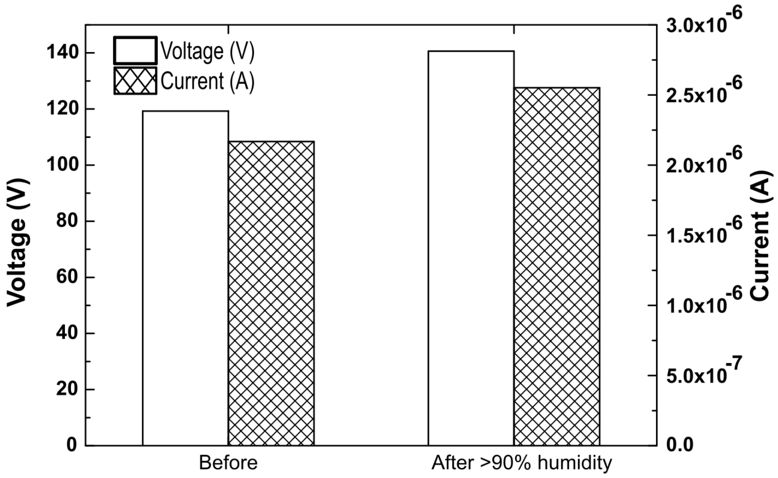

Figure 5.20: Voltage and current outputs of a PDMS-nitrile TENG before and after exposure to 90% humidity.

and current response of the TENG before and after 30 minutes of exposure to ionised air. The average voltage value had a slight change of 2 V from 141 to 143 V while the current remained at 2.5 μA, indicating good stability in performance under these conditions.

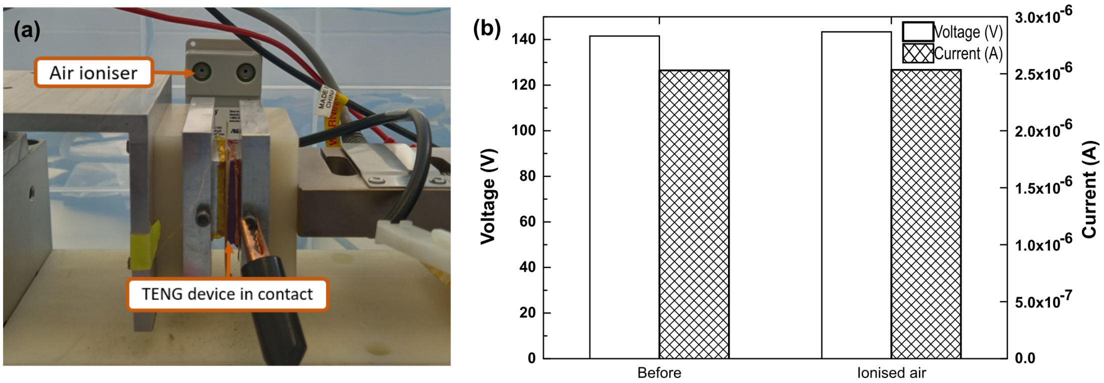

Figure 5.21: A lab air ioniser is kept switched on next to the PDMS-nitrile TENG device for 30 minutes and voltage and current outputs are recorded before and after air ionisation. a) shows the characterisation set-up used and b) shows the average voltage and current output values as bar diagrams

5.8.3 Mechanical deformation

PDMS-nitrile TENG device was subjected to bending around a curved surface of a cylinder of 1.5 cm radius in order to study its effect on the performance of the TENG device. This was done to replicate how the device would perform under body movements as a wearable device. They were tested while they are in a bent position as well as after repeated bending cycles to study their

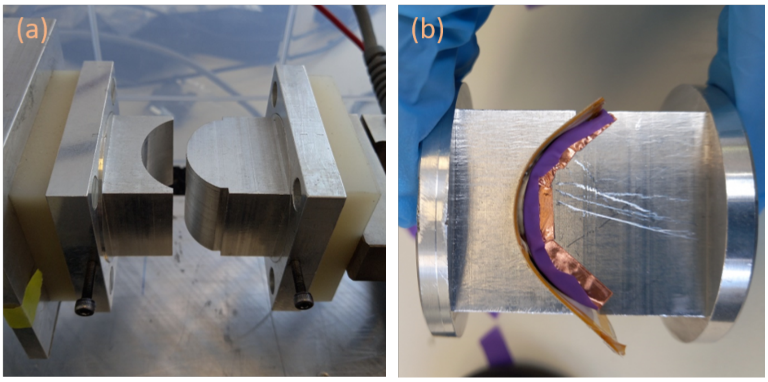

Figure 5.22: a) Curved sample holders were used to testing the performance of TENG devices in a bent position. b) sample holders in contact position (taken out of the characterisation set-up) with PDMS-nitrile TENG mounted on them.

recovery. For the first part, the PDMS-nitrile TENG were tested while it was in a compressed/bent position with the help of the curved sample holders as shown in Figure 5.22. The test side of the TENG (nitrile side) was mounted on the outward bent holder and the PDMS side on the inward bent holder. They were then mounted onto the stage and tested at contact and separation mode as usual to record the voltage and current outputs. Figure 5.23 shows the outputs obtained from the TENG in a bent position compared to the usual flat position. It shows a significant reduction in performance. The average voltage and current outputs of 140 V, 3.4 μA recorded at the normal flat position of the PDMS-nitrile TENG are reduced to 92 V, 1.1 μA while the device is in a bent position. This arises mainly from the reduced area of contact between the two sides here, as the bent structure of sample holders prevents full contact between the two sides (shown in Figure 5.22b), affecting the TENG output as discussed in Section 5.7.4. Even though, the PDMS layer encapsulates the GNPs coating on the PDMS side of TENG, stretching/compression produced on this can also affect the conductivity of GNPs coating as discussed in Section 4.5.5, contributing to reduced TENG output.

Voltage and current outputs of a PDMS-nitrile TENG were also recorded before and after 1000 bending cycles of the PDMS side. This is done to see if the device would be able to recover from the repeated bend/compressed positions. Figure 5.24a shows the PDMS side during the bent cycle and Figure 5.24b shows the average voltage and current responses plotted as bar diagrams. Before bending an average TENG output of 143 V and 2.2 μA were recorded. After bending the PDMS side 1000 times, the average output of 138 V and 2.5 μA were recorded. This study shows the resilience of these TENG

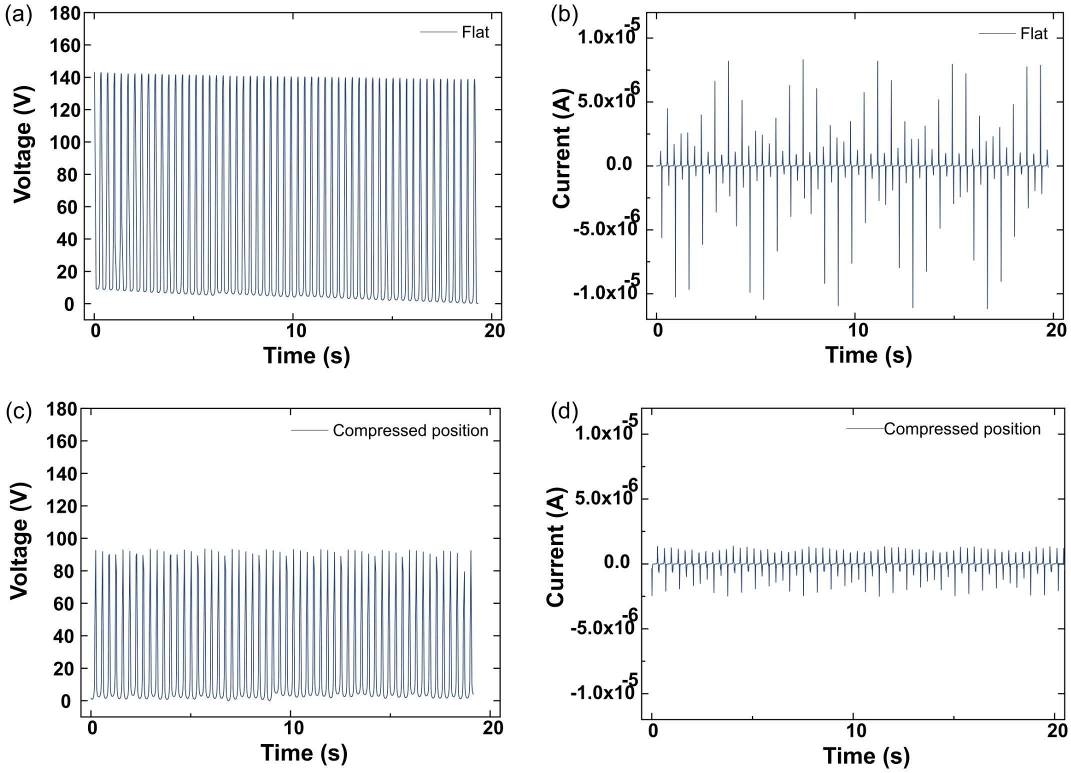

Figure 5.23: Voltage and current outputs of PDMS-nitrile TENG tested in normal flat position (a,b) and tested while in bent positions (c,d) with PDMS side in bent inward (compressed) and nitrile side on bent outwards position.

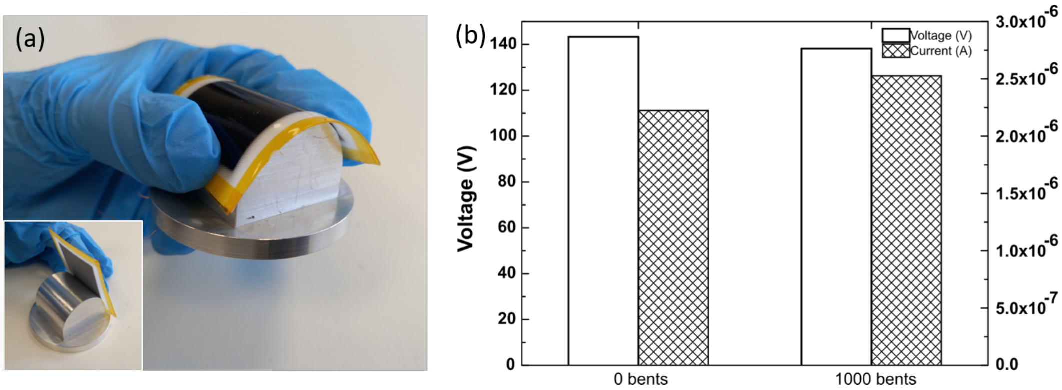

Figure 5.24: a) PDMS side of TENG bent around a curved surface of a cylinder of 1.5 cm radius for 1000 times at a fixed separation distance of 4 mm and 35 N contacting force. The inset figure at the bottom left shows the device before bending. b) Average values of voltage and current outputs recorded before and after 1000 bent cycles are shown as bar diagrams.

devices in still producing voltage and current outputs while in bend positions and their ability to recover fully to the original state of outputs once back to the flat position.

5.8.4 Durability

One of the fabricated PDMS sides used for the studies was tested in contact-separation mode against the nylon test side for more than 100,000 cycles as a part of 3000 cycles done for saturating the device before measurement. This TENG device was fabricated and in use for 20 months and it still functions properly without any damage. This TENG device shows the durability of these fabricated devices as it is important for a wearable device to have a long life span as it is not practical to replace the device/clothes often.

5.9 Summary

In this chapter, the characterisation of the TENG devices made out of the textile electrodes was discussed starting from their fabrication steps to the stability of these devices. The structure and materials used on both the PDMS side and the test side were introduced first along with their surface morphology. Typical TENG outputs of voltage, current and charge obtained from their vertical contact-separation mode of operation and their range of values in hundreds, microampere and nanocoulomb respectively were discussed. Fabricated TENG devices were characterised against various test materials to opt for nylon and nitrile as the best materials to study. The PDMS-nylon TENG displayed an optimal power of 330 $\mathrm{mW/m^2}$ at 60 $\mathrm{M\Omega}$ resistance.

Different parameters affecting the TENG outputs including chemical modification of the PDMS side, frequency of contact, separation distance, the area in contact and contacting force between the two tribolayers were studied in detail. The PDMS-nylon TENG produced a maximum of around 397 V, 6.8 μA at just 1 Hz frequency, 5mm amplitude of separation and 35 N contact force. Based on these tests, potential applications of these TENGs as pressure sensors were introduced.

In order to be part of a wearable device, these TENGs need to perform well under ambient conditions of humidity and endure a certain degree of mechanical deformations. The TENGs were tested at humidity ranging from 20 to 90%, where they gave a consistent performance from 20 to 60% and dropped in output values past 70% humidity. However even after prolonged exposure to the high humidity of $>$90%, once the humidity was brought back to the ambient range, they were able to pick up their initial range of output values. A similar study was done in the mechanical deformation tests, where TENGs were tested in compressed positions, and after 1000 bending cycles, devices maintained stable results. The durability of these fabricated TENG devices was shown by their performance even after 100,000 cycles of contact and separation.

Chapter 6

Applications & future direction

6.1 Introduction

In this chapter, applications of the fabricated GNPs spray-coated fabrics and TENG devices are discussed. The applications demonstrated here include powering up commercial light-emitting diodes (LEDs), lab-made organic LEDs (OLEDs) and a TENG device working as a pressure sensor. The TENGs developed in this thesis are also explored for their potential applications in fields of emergency services, health, seismology, human-machine interfacing etc.

6.2 Energy harvesting device

TENGs are primarily studied as energy harvesting devices. The contact-separation mode of TENG operation produces AC outputs as discussed in detail in Section 5.4. In order to demonstrate the capability of these devices to operate low-power electronics, their AC outputs need to be converted to DC. For this a circuit was used, shown in Figure 6.1, consisting of a rectifier, capacitors, switch and a 12 Ω resistor. The AC output from the TENG device is fed to a single-phase bridge rectifier of 400 V, 1 A (DF04M-E3/45). The DC outputs from the rectifier are then used to charge two electrolytic capacitors of 47 μF, 200 V. A switch connected between the capacitors and load can be used to discharge the capacitor to power up the load. It should be noted that these are not effective way of power management as there is a high difference in impedance values of the TENG device and the capacitor lowering the charging efficiency. For demonstration purposes, using these circuits is common. Wearable fabric and fibre-based TENG devices have been shown to power up LEDs [76], scientific calculators [77] etc. by connecting via such circuits.

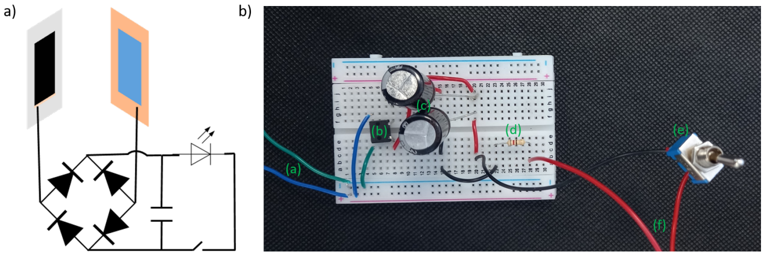

Figure 6.1: Electronic circuit used to convert the AC TENG output to DC. a) Schematic diagram of the circuit and b) circuit used with components labelled as (a) TENG output probes, (b) rectifier for AC to DC conversion, (c) two electrolytic capacitors to store the charge, (d) 12 Ω resistance, e) two-way switch which can discharge the stored charge to the load via f) copper wires to the load.

Conventional hard electric components were used for the circuit here, to demonstrate the potential of these TENGs for a wearable device. For actual integration of these TENG devices into garments, these circuit components need to be replaced with their wearable equivalents. For example, multiple yarn-based [78] or fabric/fibre-based supercapacitors [79], [80] can be integrated with these TENG devices along with graphene or carbon nanotubes (CNTs) coated fibres as charge carriers [81], [23], [82] to complete the self-charging power textile.

The ability of these TENGs as power sources are demonstrated here by choosing two types of loads. The first one is an OLED made in our lab by Dr Conor Murphy during his PhD [83]. The OLED structure was, ITO/PEDOT:PSS(30-40 nm)/TFB(30-40 nm)/F8:F8BT(60-80 nm)/Liq(5-10 nm)/Al(100 nm) [83]. F8BT polymer is used as an emission layer in this structure, producing green light on activation. A PDMS-nitrile TENG is connected to this 20 V, 1 mA OLED strip via the rectifier-capacitor circuit described above. Figure 6.2 shows the OLED strip lit from the TENG output with a luminosity of 793 cd/m^2 recorded with the help of a handheld luminance meter.

For the second demonstration load, commercial LEDs are chosen. 120 red LEDs of 1.6 V, 1 mA drop were arranged in series on a breadboard. This corresponds to a total potential drop of 192 V. This set-up was kept inside a black box to clearly see the intensity of these LEDs when lit up from the TENG output. A PDMS-nylon TENG output at 3 Hz frequency, 35 N contacting force and 8 mm maximum separation distance was fed to these LEDs via the rectifier-capacitor circuit of Figure 6.1b. Figure 6.3a shows the set-up in the switch-off position and Figure 6.3b shows the LEDs brightly lit in switched on position.

As discussed before, the PDMS-nylon TENG developed in this work, was

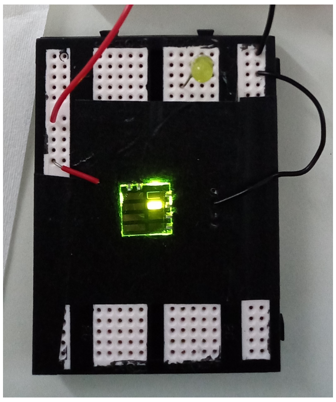

Figure 6.2: Lab-made OLED of 20 V, 1 mA, lit (bright green colour) from a PDMS-nitrile TENG output at 3 Hz frequency, 4 mm maximum separation distance and 35 N contacting force. OLED displayed a luminosity of 793 cd/m^2.

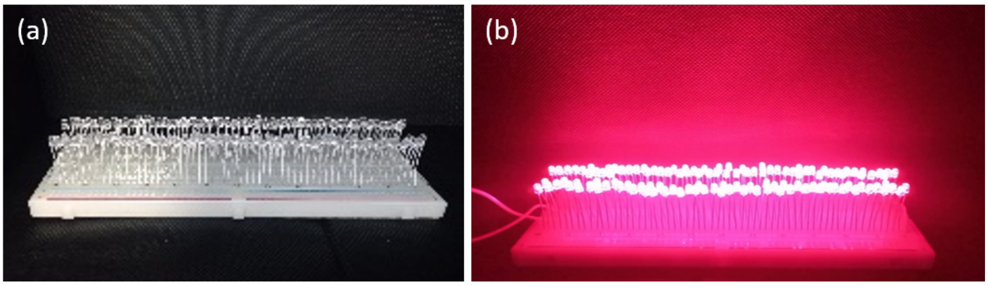

Figure 6.3: Output of a PDMS-nylon TENG at 3 Hz frequency, 35 N contacting force and 8 mm maximum separation distance is fed to 120 commercial red LEDs of 1.6 V, 1 mA power connected in series. a) Shows the LEDs in the switch-off position and b) in the switch-on position.

able to produce a maximum output of 397 V and 6.8 μA with a power density of 0.3 W/m^2 at 60 MΩ. Similar work on single electrode TENG with GO and PDMS compound layer and a conductive fabric as electrode were shown to generate 140 V and 2.6 μA output after SF$_6$ fluorination [84]. This was enough to generate 180 green LEDs and was able to send a signal to a mobile phone through a wireless Bluetooth module. Another study on wearable TENG made of nylon fabric with graphene paste as the electrode and blade-coated PDMS as the triboelectric layer against the skin has been applied in the field of human-machine interfacing. This was done by using the TENG as a motion controller for remotely controlling a tele-car [28]. Since these devices have similar electrical outputs to ours, it demonstrates the potential of our PDMS-nylon TENG device towards similar low-power electronics.

6.3 Potential applications

In this section, the potential applications of the GNPs-coated fabrics and TENG devices are discussed based on continuing work and published works on graphene and TENGs. As this project mainly concentrated on the understanding and engineering aspect of these coatings and devices, there is room open for the demonstration of their potential in other sectors.

6.3.1 Vibration study

Natural rubber is widely studied and applied as a means to isolate buildings from ground-born vibrations. Rubber is combined with steel to form composite in bearing shapes which are used between the building and its foundation. This act as a buffer between them to protect the structure from earthquakes, by reducing the intensity transferred to the building [85].

Here, the ability of GNPs to reinforce rubber pads to improve their mechanical properties is explored. This was done by spray coating the water-based GNPs suspension onto these rubber pads as shown in Figure 6.4. These coated rubber pads were then stacked onto layered structures to study their response to vibrations of certain frequencies. A part of this study was done on 50% recycled rubber from tyres to 50% natural rubber substrates. The resulting graphene-coated rubber structure showed an improved performance of up to 500% elongation and more than 300% ability to withstand high tensile forces compared to the sample with no graphene reinforcing [86].

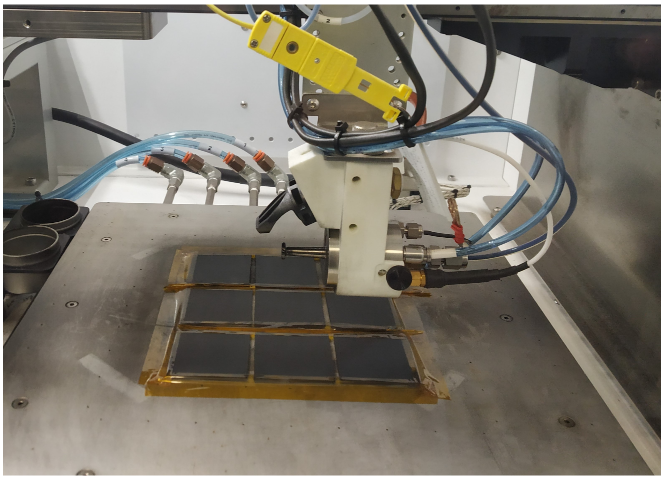

Figure 6.4: Spray coating of GNPs onto 9 rubber pads arranged on the hotplate of the spray coater.

6.3.2 Pressure sensor

As demonstrated in the previous section, these textile TENGs would be able to perform as a power source for wearable electronics. Here, the ability of a PDMS-nitrile TENG device to perform as a pressure sensor is explored. A wearable pressure sensor can find applications in the fields of healthcare, sports science etc.[87],[88].

The response of a PDMS-nitrile TENG to an increased range of contacting force between the TENG dielectric layers is discussed in detail in Section 5.7.5. The contacting force was raised from 30 to 60 N and the average current obtained for each applied force was plotted. This shows a linear average response of current output to the force applied, as shown in Figure 6.5, showing its ability to work as a pressure sensor.

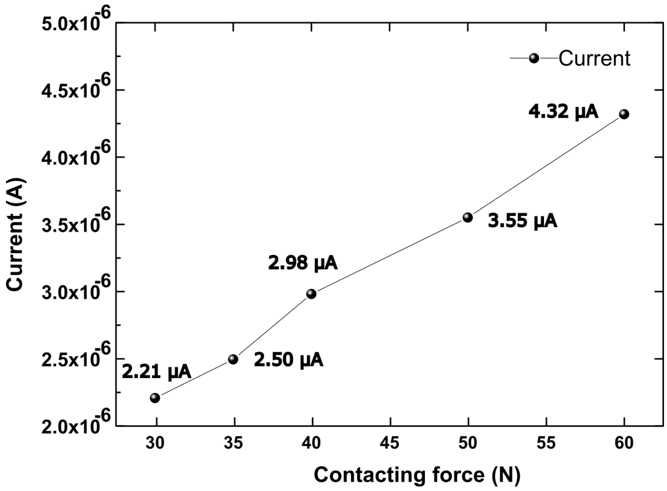

Figure 6.5: Average current outputs obtained for increased contacting force between the tribolayers of a PDMS-nitrile TENG gives a linear response, showing its potential as a self-powered pressure sensor.

This wearable sensor could be placed under the foot to map the pressure distribution on foot placement while standing and moving. This is helpful in identifying the natural gait, symmetry in the distribution of weight through the lower limbs, the right balance in foot placement, unknown injuries to the foot etc.[89]. Therefore they are generally used in the medical sector as well as sports fitness applications. Multiple PDMS-nitrile TENGs could be arranged through the area of the foot to capture the pressure applied as it would vary based on different locations of the foot. TENGs can be arranged under the shoe insole to cover the foot area, this would conceal the device as well.

These PDMS-nitrile pressure sensors could also be placed in crutches to monitor the weight bearing of patients post-surgery. For healing a fracture or injury to the lower limbs, it is important to monitor the force put on the affected area for its effective healing. Based on the stage of healing, it could go from no weight bearing to partial weight bearing and finally to full weight bearing [90]. Most times it is difficult to know the right amount required. By adding pressure sensors to the crutches, the weight applied on each case can be easily managed for an effective recovery. This also eliminates the need for a patient to be constantly monitored in a hospital environment.

This pressure sensor has the potential to monitor the pulse of an individual by placing it on the wrist or chest. Compared to the previous applications, this requires the device to be sensitive to a very low range of pressure. Monitoring the pulse rate of an individual can give details about their fitness and knowing the resting heartbeat is useful to keep track of heart health as well.

6.4 Summary

This chapter includes the applications of the GNPs spray coating method, fabricated textile electrodes and textile TENGs. The ability of textile TENGs to power low-power electronics was demonstrated by lighting up 120 commercial LEDs and lab-made OLED with the TENG output. The potential application of PDMS-nitrile TENG as a pressure sensor, introduced in the previous chapter was also discussed in detail. Outside the wearable range of applications, GNPs spray coating was also done on rubber pads for vibrational study towards building earthquake-safe structures.

6.5 Future work

There are certain fabrication and characterisation steps followed in this work, that could be further modified and analysed. This would provide an improved understanding of certain aspects of the work. Due to limitations in time and availability and to strictly stick to the scope of this work, they were not carried out during the project. Some of the points listed below can be further investigated by continuing project students for the completion of this project and progress in this field.

- In chapter 4, the resistance of GNPs spray-coated fabrics was found to be in the kΩ range. Further studies can be done to reduce this value down to the range of a few Ω. These textile electrodes are already tested by increasing the number of coating cycles to enhance the conductivity, but they get saturated after reaching the kΩ range. Also, increasing the concentration of GNPs in the suspension beyond 1.4 g/L results in the sedimentation of GNPs as the solution is over-saturated. This study can be further explored by adding conductive materials to GNPs such as conductive polymers, nanoparticles etc. or switching to a more conductive grade of GNP etc. As a next step it would be good to explore the possibilities of adding carbon nanotubes (CNT) especially multiwalled CNT (MWCNT), to the current GNPs suspension. This would be able to reinforce the mechanical strength as well as increase the electrical conductivity of the coating, producing a highly conductive and flexible fabric-based electrode. This way, devices fabricated using these electrodes would be able to produce an enhanced performance even under mechanical stress/strain from bodily movements.

- GNPs coating on a much larger area also needs to be studied to understand the uniformity of coating on that scale. For this, a 20 cm × 20 cm area of polyester fabric can be spray coated with GNPs and sheet resistance measurements need to be done at different locations of this sample to check if the resistance values are similar.

- GNPs coated fabrics, apart from their use as electrodes, can be explored for sensing sweat, humidity, temperature etc. as graphene has already been shown as a good candidate for sensors in chemical [91], electronic [92], optic [93] and general human health monitoring [94] owing to its exceptional properties.

- Raman mapping of GNPs coated glass substrates needs to be analysed thoroughly by using the shift in G peak and 2D peak as well as their ratios to calculate the strain and doping present in this purchased GNPs powder to get a better understanding of the graphene used.

- In TENG fabrication, PDMS spin coating speed needs to be optimised. Only 8, 16 and 32 rps were tested to select the speed, as fine-tuning was not available in the spin coater used. As PDMS is difficult to handle to use a precise amount with a syringe, the amount poured on the sample prior to coating did also vary. TENGs made with these different layers of PDMS thickness then need to be tested for their performance against the same test side at the same ambient conditions in order to select the optimal thickness for better output. PDMS can also be diluted with hexane to achieve better thickness ranges.

- Silver epoxy paste and copper wire used on the edge of GNPs coating for the connection to external circuits also need to be replaced and tested with more wearable-friendly options at the time of integration to garments. The same needs to be done for the AC to DC conversion circuit as well.
- Different chemical modifications other than the SF_6, the introduction of nanostructures on the PDMS surface and the deposition of porous PDMS layer need to be tested to improve the TENG performance.
- A needle puncher of really small needle diameters can be used on the PDMS side to improve the air permeability [28] of the device and the device performance needs to be studied before and after introducing holes to the PDMS side.

Chapter 7

Summary

The aim of this thesis was to develop a truly wearable textile-based TENG. This was motivated by the lack of a wearable alternative for the batteries, to build self-powered wearable electronics. TENGs suited the cause as they can be effectively used to harvest the biomechanical energy produced by the human body and convert it to electricity. TENGs works based on triboelectric effect and electrostatic induction. Friction caused by the movements of the human body such as the one between cloth fabric and skin produces a triboelectric charge and by the addition of electrodes, this can be turned into electricity. Graphene is used as the electrode material in order to preserve fabric properties and add conductivity.

In Chapter 3, all the techniques used for the fabrication and characterisation of graphene electrodes and textile TENGs were discussed. This includes the novel method of ultrasonic spray coating of graphene suspension followed in this work. This technique helped the fabrication of a uniform, two-dimensional electrode coating on fabric substrates of low resistance (<50 kΩ). Compared to lab-scale spin coating and vacuum filtration techniques, this method is also industrially scalable and of low cost supporting its mass manufacture. The graphene suspension used is water-based with no added surfactants.

In Chapter 4, textile electrodes made from the spray coating of graphene suspension are characterised towards their application in wearable electronics. Since it is an original work conducted in this project, it is important to understand the topological, mechanical and conductive properties of these fabricated electrodes separately before incorporating them into devices. Surface morphology study conducted using SEM provided good coverage of graphene on the fabric surface down to individual fibres. This ensured good flexibility of the fabric electrode as a continuous thin film-like coverage over the whole fabric would have been prone to cracks. Sheet resistance obtained using the van der Pauw method was found to be in the low kΩ range ensuring suitable conductivity towards electrode applications. Exposure of fabrics to UVO treatment prior to coating studied with a goniometer was found to aid in a better coating of GNPs on the surface. These coated fabrics also showed a good degree of resilience to various levels of bent, compression and tensile load testings, making them a good candidate to be a textile electrode for wearable electronics.

In Chapter 5, novel, simple structured textile TENGs made using these graphene-coated textile electrodes are characterised. PDMS polymer was used as a tribolayer on one side against nylon or nitrile material on the other side. These TENG devices were characterised in detail for different parameters affecting their output for understanding the working mechanism as well as using them as ways to enhance the performance of these devices. It should be noted that, for the entire study, no output-amplifying components were used. All listed values are the direct outputs obtained from this simple TENG structure. PDMS-nylon TENG produced a maximum power output of 330 mW/m^2 at 60 MΩ resistance. Chemically modifying the PDMS side by fluorinating with SF_6 gas plasma enhanced the voltage and current outputs of PDMS-nylon TENG by 154% and 127% reaching 356 V, 2.5 μA at 1 Hz. Since voltage remained independent of frequency, the current response to increased frequency was studied, obtaining a maximum of 7.3 μA at 4Hz. The maximum separation distance between the tribolayers was examined and obtained an increasing response to the range of 4 to 10 mm studied producing a maximum of 397 V and 7.7 μA at 10 mm separation. Increased output values to the increased contact area between the tribolayers were also quantified. Finally, the force applied on contact between the PDMS and test side was studied and a linear response was obtained to increased contacting force-output current relation, indicating its ability to perform as a pressure sensor. One of the parameters that need to be evaluated, but has not been explored in this study, is the contact angle set between the two triboelectric layers. Any change to the angle set between the tribolayers would affect the area in contact, thus affecting the output. TENGs were also tested for their ability to withstand high humidity, ionised atmosphere, and mechanical deformations and the device was able to perform well under these harsh conditions adding to the durability of the device.

In Chapter 6, the potential applications of these TENG devices towards smart textiles were demonstrated. As TENGs were fabricated as energy-harvesting devices to replace the role of batteries in low-power circuits, it was important to demonstrate their ability to power up such devices. This was done by connecting the output from these textile TENGs to commercial LEDs and lab-made organic LEDs. For this, it was important to use a circuit consisting of mainly a rectifier and capacitor to convert the AC output from TENG devices to DC. This way, output from a PDMS-nylon TENG was able to light up 120 commercial LEDs arranged on a breadboard and the OLED. Apart from energy harvesting applications, these TENG devices were also shown to perform as a pressure sensor, due to their linear current response to the applied force. Depending on the range of pressure studied, applications of these sensors can vary from monitoring pulse rate, keeping track of weight bearing in limb injuries, foot pressure mapping etc. in remote health monitoring. As a next step, it would be good to demonstrate this ability by placing the TENG device at the appropriate locations such as the wrist or chest for pulse monitoring, in the crutches for weight bearing and under shoe insoles for foot pressure mapping.

To summarise, this thesis focused on the study of a simpler, truly wearable, TENG structure with an ultrasonically spray-coated graphene electrode. This involved the detailed study of graphene suspensions, fabricated novel textile electrodes and TENG devices made using these electrodes. Graphene electrodes on fabrics were in the kΩ/sq range of sheet resistance and the GNPs were found to coat the fabrics uniformly. The sheet resistance of these electrodes can be further lowered in future continuation by the addition of MWCNTs to the GNPs suspension which would also reinforce the mechanical properties of the coating adding to the flexibility of the resulting device. TENG study involved understanding its electrical response by studying different parameters associated with its vertical contact-separation mode of operation. In general, they were able to produce up to 400 V and 7.7 μA with a power density of 0.3 W/m^2 at 60 MΩ. These results can be further improved by adding physical and chemical modifications to the PDMS tribolayer. The potential of these TENGs as power sources was also demonstrated with different electronic devices and their abilities to work as pressure sensors are discussed in various health monitoring sectors.

Appendix A

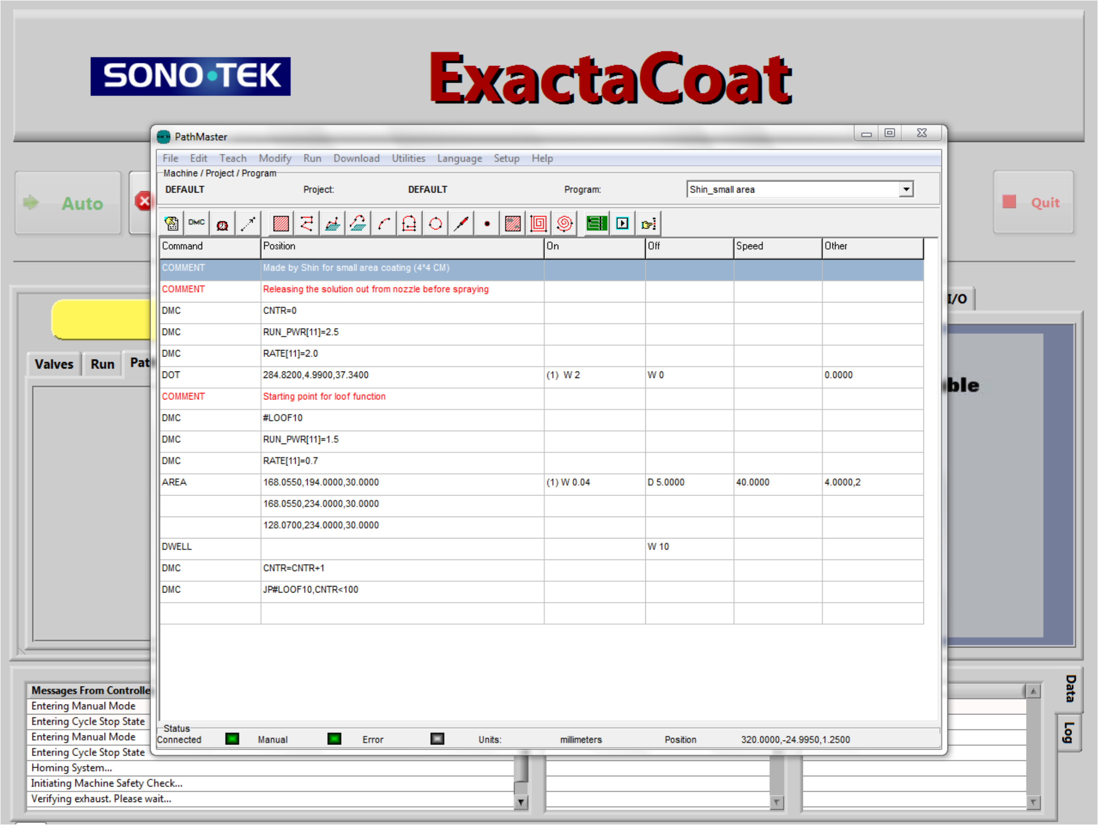

Machine / Project / Program
DEFAULT
Project: DEFAULT
Program: Shin_small area

Command	Position	On	Off	Speed	Other
COMMENT	Made by Shin for small area coating (4*4 CM)				
COMMENT	Releasing the solution out from nozzle before spraying				
DMC	CNTR=0				
DMC	RUN_PWR[11]=2.5				
DMC	RATE[11]=2.0				
DOT	284.8200,4.9900,37.3400	(1) W 2	W 0		0.0000
COMMENT	Starting point for loof function				
DMC	#LOOF10				
DMC	RUN_PWR[11]=1.5				
DMC	RATE[11]=0.7				
AREA	168.0550,194.0000,30.0000	(1) W 0.04	D 5.0000	40.0000	4.0000,2
	168.0550,234.0000,30.0000				
	128.0700,234.0000,30.0000				
DWELL			W 10		
DMC	CNTR=CNTR+1				
DMC	JP#LOOF10,CNTR<100				

Status
Connected 🟩 Manual 🟩 Error ■ Units: millimeters Position 320.0000,-24.9950,1.2500

```
Messages From Controlle
Entering Manual Mode
Entering Cycle Stop State
Entering Manual Mode
Entering Cycle Stop State
Homing System...
Initiating Machine Safety Check...
Verifying exhaust. Please wait...
```

Figure A.1: A program written in the pathmaster software of the ultrasonic spray coater for spray coating a 4 cm × 4 cm area (specified with x,y,z coordinates under the area command), with 100 passes (specified using variable CNTR) of coating and 10 seconds gap (dwell command) between each coat.

Appendix B

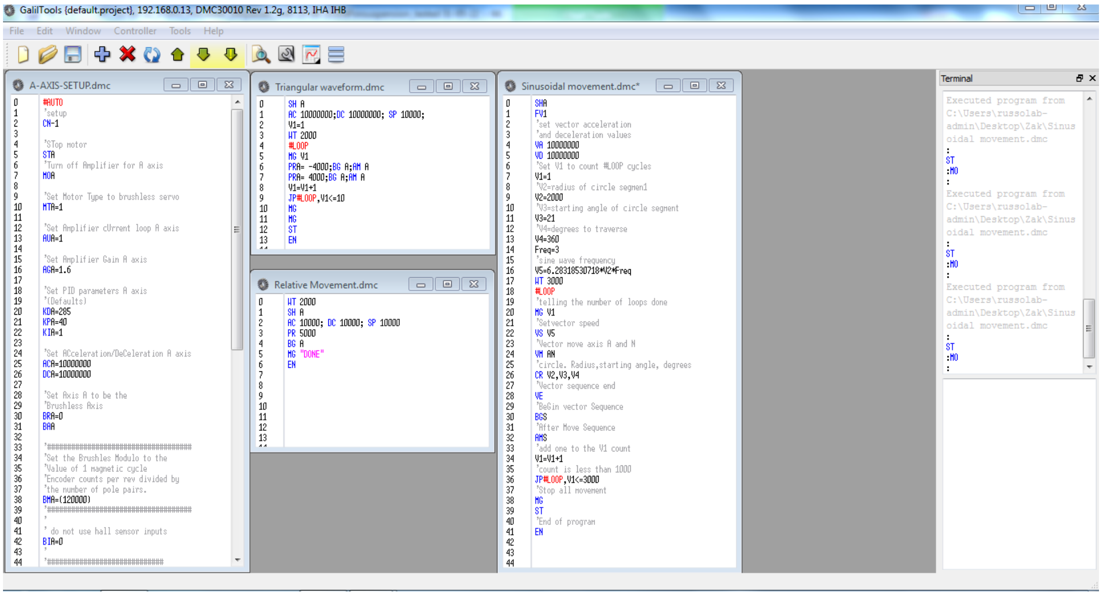

```
#AUTO
'setup
CN-1

'STop motor
STA
'Turn off Amplifier for A axis
MOA

'Set Motor Type to brushless servo
MTA=1

'Set Amplifier cUrrent loop A axis
AUA=1

'Set Amplifier Gain A axis
AGA=1.6

'Set PID parameters A axis
'(Defaults)
KDA=285
KPA=40
KIA=1

'Set ACceleration/DeCeleration A axis
ACA=10000000
DCA=10000000

'Set Axis A to be the
'Brushless Axis
BRA=0
BAA

'########################################
'Set the Brushles Modulo to the
'Value of 1 magnetic cycle
'Encoder counts per rev divided by
'the number of pole pairs.
BMA=(120000)
'########################################
'
' do not use hall sensor inputs
BIA=0
'
'################################
```

```
SH A
AC 10000000;DC 10000000; SP 10000;
V1=1
WT 2000
#LOOP
MG V1
PRA= -4000;BG A;AM A
PRA= 4000;BG A;AM A
V1=V1+1
JP#LOOP,V1<=10
MG
MG
ST
EN
```

```
WT 2000
SH A
AC 10000; DC 10000; SP 10000
PR 5000
BG A
MG "DONE"
EN
```

```
SHA
FV1
'set vector acceleration
'and deceleration values
VA 10000000
VD 10000000
'Set V1 to count #LOOP cycles
V1=1
'V2=radius of circle segmen1
V2=2000
'V3=starting angle of circle segment
V3=21
'V4=degrees to traverse
V4=360
Freq=3
'sine wave frequency
V5=6.28318530718*V2*Freq
WT 3000
#LOOP
'telling the number of loops done
MG V1
'Setvector speed
VS V5
'Vector move axis A and N
VM AN
'circle. Radius,starting angle, degrees
CR V2,V3,V4
'Vector sequence end
VE
'BeGin vector Sequence
BGS
'After Move Sequence
AMS
'add one to the V1 count
V1=V1+1
'count is less than 1000
JP#LOOP,V1<=3000
'Stop all movement
MG
ST
'End of program
EN
```

```
Executed program from
C:\Users\russolab-
admin\Desktop\Zak\Sinus
oidal movement.dmc
:
ST
:MO
:
Executed program from
C:\Users\russolab-
admin\Desktop\Zak\Sinus
oidal movement.dmc
:
ST
:MO
:
Executed program from
C:\Users\russolab-
admin\Desktop\Zak\Sinus
oidal movement.dmc
:
ST
:MO
:
```

Figure B.1: Galil tool software used to control the contact-separation motion of the linear motor in TENG characterisation set-up. Number of cycles (V1), separation distance between the sample holders (V2), contact force (V3), frequency of contact (Freq) are generally changed to study the effect on TENG output. Values are provided in micrometer units.

Appendix C

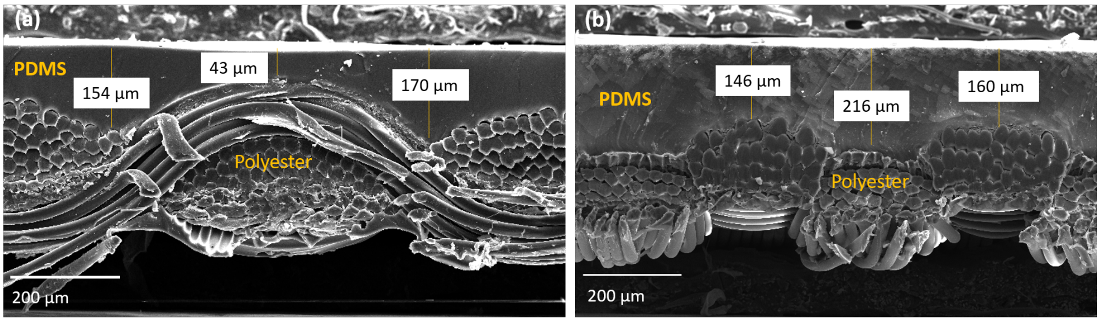

Figure C.1: Thickness study done on PDMS polymer spin-coated on GNPs spray coated polyester fabrics. Both samples are spin coated at 8 rps, 30 seconds speed. Sample a) has a minimum of 43 μm and a maximum thickness of 170 μm while sample b) has a minimum of 146 μm and a maximum thickness of 216 μm.

Bibliography

[1] Sumit Majumder, Tapas Mondal, and M. Jamal Deen. "Wearable Sensors for Remote Health Monitoring". In: *Sensors* 17.1 (2017), p. 130. ISSN: 1424-8220.

[2] Han Jin et al. "Advanced Materials for Health Monitoring with Skin-Based Wearable Devices". In: *Advanced Healthcare Materials* 6.11 (2017), p. 1700024. ISSN: 2192-2659.

[3] Hengxin Liu et al. "Recent progress in the fabrication of flexible materials for wearable sensors". In: *Biomaterials Science* 10.3 (2022), pp. 614–632. ISSN: 20474849.

[4] R. D.I.G. Dharmasena and S. R.P. Silva. "Towards optimized triboelectric nanogenerators". In: *Nano Energy* 62.5 (2019), pp. 530–549. ISSN: 22112855.

[5] Zhong Lin Wang and Aurelia Chi Wang. "On the origin of contact-electrification". In: *Materials Today* 30.11 (2019), pp. 34–51. ISSN: 1369-7021.

[6] Shuaihang Pan and Zhinan Zhang. "Fundamental theories and basic principles of triboelectric effect: A review". In: *Friction* 7.1 (2018), pp. 2–17. ISSN: 2223-7704.

[7] R. D.I.G. Dharmasena et al. "A unified theoretical model for Triboelectric Nanogenerators". In: *Nano Energy* 48.3 (2018), pp. 391–400. ISSN: 22112855.

[8] Simiao Niu et al. "Theoretical study of contact-mode triboelectric nanogenerators as an effective power source". In: *Energy and Environmental Science* 6.12 (2013), pp. 3576–3583. ISSN: 17545692.

[9] Simiao Niu and Zhong Lin Wang. "Theoretical systems of triboelectric nanogenerators". In: *Nano Energy* 14 (2014), pp. 161–192. ISSN: 22112855.

[10] Changsheng Wu et al. "Triboelectric Nanogenerator: A Foundation of the Energy for the New Era". In: *Advanced Energy Materials* 9.1 (2019), pp. 1–25. ISSN: 16146840.

[11] Feng Ru Fan, Zhong Qun Tian, and Zhong Lin Wang. "Flexible triboelectric generator". In: *Nano Energy* 1.2 (2012), pp. 328–334. ISSN: 2211-2855.

[12] Kai Dong et al. "A Stretchable Yarn Embedded Triboelectric Nanogenerator as Electronic Skin for Biomechanical Energy Harvesting and Multifunctional Pressure Sensing". In: *Advanced Materials* 30.10 (2018), p. 1804944. ISSN: 1521-4095.

[13] Jin Yang et al. "Triboelectrification-based organic film nanogenerator for acoustic energy harvesting and self-powered active acoustic sensing". In: *ACS Nano* 8.3 (2014), pp. 2649–2657. ISSN: 1936086X.

[14] Xiandi Wang et al. "Self-Powered High-Resolution and Pressure-Sensitive Triboelectric Sensor Matrix for Real-Time Tactile Mapping". In: *Advanced materials (Deerfield Beach, Fla.)* 28 (15 2016), pp. 2896–2903. ISSN: 1521-4095.

[15] Sungmook Jung et al. "Fabric-Based Integrated Energy Devices for Wearable Activity Monitors". In: *Advanced Materials* 26 (36 2014), pp. 6329–6334. ISSN: 1521-4095.

[16] Minglu Zhu et al. "Haptic-feedback smart glove as a creative human-machine interface (HMI) for virtual/augmented reality applications". In: *Science Advances* 6 (19 2020). ISSN: 23752548.

[17] Changsheng Wu et al. "Keystroke dynamics enabled authentication and identification using triboelectric nanogenerator array". In: *Materials Today* 21 (3 2018), pp. 216–222. ISSN: 18734103.

[18] Yu Chen, Yali Ling, and Rong Yin. "Fiber/Yarn-Based Triboelectric Nanogenerators (TENGs): Fabrication Strategy, Structure, and Application". In: *Sensors* 22 (24 2022), p. 9716. ISSN: 1424-8220.

[19] Watcharapong Paosangthong, Russel Torah, and Steve Beeby. "Recent progress on textile-based triboelectric nanogenerators". In: *Nano Energy* 55 (2019), pp. 401–423. ISSN: 2211-2855.

[20] Sung Soo Kwak, Hong Joon Yoon, and Sang Woo Kim. "Textile-Based Triboelectric Nanogenerators for Self-Powered Wearable Electronics". In: *Advanced Functional Materials* 29 (2 2019), p. 1804533. ISSN: 1616-3028.

[21] Jianjun Luo et al. "Recent progress of triboelectric nanogenerators: From fundamental theory to practical applications". In: *EcoMat* 2.4 (2020), p. 12059. ISSN: 2567-3173.

[22] Peng Huang et al. "Textile-Based Triboelectric Nanogenerators for Wearable Self-Powered Microsystems". In: *Micromachines* 12.2 (2021), p. 158. ISSN: 2072-666X.

[23] A. I.S. Neves et al. "Transparent conductive graphene textile fibers". In: *Scientific Reports* 5 (2015), pp. 1–7. ISSN: 20452322.

[24] Mohammad Shateri-Khalilabad and Mohammad E. Yazdanshenas. "Fabricating electroconductive cotton textiles using graphene". In: *Carbohydrate Polymers* 96.1 (2013), pp. 190–195. ISSN: 01448617.

[25] Mahmuda Akter Shathi et al. "Graphene coated textile based highly flexible and washable sports bra for human health monitoring". In: *Materials and Design* 193 (2020), p. 108792. ISSN: 18734197.

[26] Paolo Bondavalli et al. "Deposition of graphene and related nanomaterials by dynamic spray-gun method: a new route to implement nanomaterials in real applications". In: *Journal of Physics: Materials* 2.3 (2019), p. 032002. ISSN: 2515-7639.

[27] Hee Jae Hwang et al. "Extremely Foldable and Highly Porous Reduced Graphene Oxide Films for Shape-Adaptive Triboelectric Nanogenerators". In: *Small* 17.9 (2021), p. 1903089. ISSN: 16136829.

[28] Yiming Liu et al. " Thin, soft, garment-integrated triboelectric nanogenerators for energy harvesting and human machine interfaces ". In: *EcoMat* 3.4 (2021), e12123. ISSN: 2567-3173.

[29] Faizatul Farah Hatta, Muhammad Aniq Shazni Mohammad Haniff, and Mohd Ambri Mohamed. "A review on applications of graphene in triboelectric nanogenerators". In: *International Journal of Energy Research* 46.2 (2022), pp. 544–576. ISSN: 1099114X.

[30] K. S. Novoselov et al. "Electric field in atomically thin carbon films". In: *Science* 306.5696 (2004), pp. 666–669. ISSN: 00368075.

[31] K. S. Novoselov et al. "The electronic properties of graphene". In: *Reviews of Modern Physics* 81.1 (2009), pp. 109–162. ISSN: 0034-6861.

[32] Claudia Backes et al. "Production and processing of graphene and related materials". In: *2D Materials* 7.2 (2020), p. 022001. ISSN: 2053-1583.

[33] Francesco Bonaccorso et al. "Production and processing of graphene and 2d crystals". In: *Materials Today* 15.12 (2012), pp. 564–589. ISSN: 13697021.

[34] L. Colombo et al. “A roadmap for graphene”. In: *Nature* 490.7419 (2012), pp. 192–200. ISSN: 0028-0836.

[35] Maryam Saeed et al. “Chemical Vapour Deposition of Graphene—Synthesis, Characterisation, and Applications: A Review”. In: *Molecules* 25.17 (2020), p. 3856. ISSN: 14203049.

[36] Avijit Kumar, Kaustuv Banerjee, and Peter Liljeroth. “Molecular assembly on two-dimensional materials”. In: *Nanotechnology* 28.8 (2017), p. 082001. ISSN: 0957-4484. arXiv: `1611.02462`.

[37] Gholam Reza Yazdi, Tihomir Iakimov, and Rositsa Yakimova. “Epitaxial Graphene on SiC: A Review of Growth and Characterization”. In: *Crystals* 6.5 (2016), p. 53. ISSN: 2073-4352.

[38] K. S. Novoselov et al. “Two-dimensional atomic crystals”. In: *Proceedings of the National Academy of Sciences of the United States of America* 102.30 (2005), pp. 10451–10453. ISSN: 00278424.

[39] Raluca Tarcan et al. “Reduced graphene oxide today”. In: *Journal of Materials Chemistry C* 8.4 (2020), pp. 1198–1224. ISSN: 20507526.

[40] Yenny Hernandez et al. “High-yield production of graphene by liquid-phase exfoliation of graphite”. In: *Nature Nanotechnology* 3.9 (2008), pp. 563–568. ISSN: 1748-3395. arXiv: `0805.2850`.

[41] Keith R. Paton et al. “Scalable production of large quantities of defect-free few-layer graphene by shear exfoliation in liquids”. In: *Nature Materials* 13.6 (2014), pp. 624–630. ISSN: 14764660.

[42] Pietro Cataldi, Athanassia Athanassiou, and Ilker S. Bayer. “Graphene nanoplatelets-based advanced materials and recent progress in sustainable applications”. In: *Applied Sciences (Switzerland)* 8.9 (2018), p. 1438. ISSN: 20763417.

[43] Sung Hoon Jeong et al. “Graphene coated cotton fabric as textile structured counter electrode for DSSC”. In: *Electrochimica Acta* 173 (2015), pp. 164–171. ISSN: 00134686.

[44] Archana Samanta and Romain Bordes. “Conductive textiles prepared by spray coating of water-based graphene dispersions”. In: *RSC Advances* 10.4 (2020), pp. 2396–2403. ISSN: 20462069.

[45] Felice Torrisi and Tian Carey. "Graphene, related two-dimensional crystals and hybrid systems for printed and wearable electronics". In: *Nano Today* 23 (2018), pp. 73–96. ISSN: 1878044X.

[46] Jiesheng Ren et al. "Environmentally-friendly conductive cotton fabric as flexible strain sensor based on hot press reduced graphene oxide". In: *Carbon* 111 (2017), pp. 622–630. ISSN: 00086223.

[47] Koen Gilissen et al. "Ultrasonic spray coating as deposition technique for the light-emitting layer in polymer LEDs". In: *Organic Electronics* 20 (2015), pp. 31–35. ISSN: 1566-1199.

[48] Ben Millington, Vincent Whipple, and Bruno G. Pollet. "A novel method for preparing proton exchange membrane fuel cell electrodes by the ultrasonic-spray technique". In: *Journal of Power Sources* 196.20 (2011), pp. 8500–8508. ISSN: 0378-7753.

[49] K. Xerxes Steirer et al. "Ultrasonic spray deposition for production of organic solar cells". In: *Solar Energy Materials and Solar Cells* 93.4 (2009), pp. 447–453. ISSN: 0927-0248.

[50] Shuaihang Pan and Zhinan Zhang. "Fundamental theories and basic principles of triboelectric effect: A review". In: *Friction* 7.1 (2019), pp. 2–17. ISSN: 22237704.

[51] Xiao Sheng Zhang et al. "All-in-one self-powered flexible microsystems based on triboelectric nanogenerators". In: *Nano Energy* 47.1 (2018), pp. 410–426. ISSN: 22112855.

[52] Simiao Niu et al. "Optimization of triboelectric nanogenerator charging systems for efficient energy harvesting and storage". In: *IEEE Transactions on Electron Devices* 62.2 (2015), pp. 641–647. ISSN: 00189383.

[53] Andrea C. Ferrari and Denis M. Basko. "Raman spectroscopy as a versatile tool for studying the properties of graphene". In: *Nature Nanotechnology* 8.4 (2013), pp. 235–246. ISSN: 17483395. arXiv: `1306.5856`.

[54] A. C. Ferrari et al. "Raman spectrum of graphene and graphene layers". In: *Physical Review Letters* 97.18 (2006), pp. 1–4. ISSN: 00319007.

[55] L. M. Malard et al. "Raman spectroscopy in graphene". In: *Physics Reports* 473.5-6 (2009), pp. 51–87. ISSN: 03701573. arXiv: `arXiv:0709.1174v1`.

[56] L J Van Der PAUW. “A method of measuring the resistivity and Hall coefficient on lamellae of arbitrary shape”. In: *Philips Technical Review* 20.8 (1958), pp. 220–224.

[57] Jitendra Pratap Singh and Swadesh Verma. “Raw materials for terry fabrics”. In: *Woven Terry Fabrics* (2017), pp. 19–28.

[58] Dong-Wook Shin et al. “A New Facile Route to Flexible and Semi-Transparent Electrodes Based on Water Exfoliated Graphene and their Single-Electrode Triboelectric Nanogenerator”. In: *Advanced Materials* 30.39 (2018), p. 1802953.

[59] Kavya Sreeja Sadanandan et al. “Graphene coated fabrics by ultrasonic spray coating for wearable electronics and smart textiles”. In: *Journal of Physics: Materials* 4.1 (2021), p. 014004. ISSN: 25157639.

[60] Minsu Seol et al. “Triboelectric Series of 2D Layered Materials”. In: *Advanced Materials* 30.39 (2018), p. 1801210. ISSN: 1521-4095.

[61] Mustafa Ertekin. “Aramid fibers”. In: *Fiber Technology for Fiber-Reinforced Composites* (2017), pp. 153–167.

[62] T. M.G. Mohiuddin et al. “Uniaxial strain in graphene by Raman spectroscopy: G peak splitting, Grüneisen parameters, and sample orientation”. In: *Physical Review B - Condensed Matter and Materials Physics* 79.20 (2009), p. 205433. ISSN: 1550235X. arXiv: `0812.1538`.

[63] Ryan Beams, Luiz Gustavo Cançado, and Lukas Novotny. “Raman characterization of defects and dopants in graphene”. In: *Journal of physics. Condensed matter : an Institute of Physics journal* 27.8 (2015), p. 083002. ISSN: 1361-648X.

[64] Ji Eun Lee et al. “Optical separation of mechanical strain from charge doping in graphene”. In: *Nature Communications* 3.1 (2012), pp. 1–8. ISSN: 2041-1723.

[65] Dimitar Dimov. “Fundamental physical properties of graphene reinforced concrete.” PhD thesis. University of Exeter, 2018, pp. 57–63.

[66] Morten Hannibal Madsen et al. “Accounting for PDMS shrinkage when replicating structures”. In: *Journal of Micromechanics and Microengineering* 24.12 (2014), p. 127002. ISSN: 0960-1317.

[67] Bhawana Singh Tomar, A. Shahin, and Mahesh S. Tirumkudulu. “Cracking in drying films of polymer solutions”. In: *Soft Matter* 16.14 (2020), pp. 3476–3484. ISSN: 17446848.

[68] A. Gomes et al. “Influence of Thickness and Contact Area on the Performance of PDMS-Based Triboelectric Nanogenerators”. In: (2018). arXiv: `1803.10070`.

[69] H. Tarik Baytekin et al. “Is Water Necessary for Contact Electrification?” In: *Angewandte Chemie* 123.30 (2011), pp. 6898–6902.

[70] Daewoong Hong, Young Man Choi, and Jaehwa Jeong. “Test bed for contact-mode triboelectric nanogenerator”. In: *Review of Scientific Instruments* 89.6 (2018), p. 065110. ISSN: 10897623.

[71] Renyun Zhang and Håkan Olin. “Material choices for triboelectric nanogenerators: A critical review”. In: *EcoMat* 2.4 (2020), p. 12062. ISSN: 2567-3173.

[72] Hyenwoo Chu et al. “Conformal, graphene-based triboelectric nanogenerator for self-powered wearable electronics”. In: *Nano Energy* 27 (2016), pp. 298–305. ISSN: 22112855.

[73] Tianjian Ji and Aikaterini Pachi. “Frequency and velocity of people walking”. In: *Structural Engineer* 84.3 (2005), pp. 36–40.

[74] Johnny Padulo, Karim Chamari, and Luca Paolo Ardigò. “Walking and running on treadmill: the standard criteria for kinematics studies”. In: *Muscles, Ligaments and Tendons Journal* 4.2 (2014), p. 159. ISSN: 22404554.

[75] Weixu Yang et al. “Fundamental research on the effective contact area of micro-/nano-textured surface in triboelectric nanogenerator”. In: *Nano Energy* 57.12 (2019), pp. 41–47. ISSN: 22112855.

[76] Ping Zhang, Weikang Zhang, and Honghao Zhang. “A high-performance textile-based triboelectric nanogenerator manufactured by a novel brush method for self-powered human motion pattern detector”. In: *Sustainable Energy Technologies and Assessments* 46.January (2021), p. 101290. ISSN: 22131388.

[77] Zhen Qin et al. “Flexible Janus Electrospun Nanofiber Films for Wearable Triboelectric Nanogenerator”. In: *Advanced Materials Technologies* 5.2 (2020), pp. 1–9. ISSN: 2365709X.

[78] Xiong Pu et al. “Wearable Self-Charging Power Textile Based on Flexible Yarn Supercapacitors and Fabric Nanogenerators”. In: *Advanced Materials* 28 (1 2016), pp. 98–105. ISSN: 1521-4095.

[79] Xuhui Sun et al. "Self-powered textile for wearable electronics by hybridizing fiber-shaped nanogenerators, solar cells, and supercapacitors". In: *Science Advances* 2.10 (2016), e1600097.

[80] Sreekanth J. Varma et al. "Fiber-Type Solar Cells, Nanogenerators, Batteries, and Supercapacitors for Wearable Applications". In: *Advanced Science* 5.9 (2018), p. 1800340. ISSN: 21983844.

[81] Changsheng Xiang et al. "Carbon nanotube and graphene nanoribbon-coated conductive Kevlar fibers". In: *ACS Applied Materials and Interfaces* 4.1 (2012), pp. 131–136. ISSN: 19448244.

[82] Huhu Cheng et al. "Textile electrodes woven by carbon nanotube-graphene hybrid fibers for flexible electrochemical capacitors". In: *Nanoscale* 5.8 (2013), pp. 3428–3434. ISSN: 20403364.

[83] C Murphy. "Organic light-emitting diodes with FeCl3-FLG intercalated few-layer graphene electrodes". PhD thesis. University of Exeter, 2022.

[84] Chii Rong Yang et al. "Study on fabric-based triboelectric nanogenerator using graphene oxide/porous PDMS as a compound friction layer". In: *Nano Energy* 92 (2022), p. 106791. ISSN: 2211-2855.

[85] James M. Kelly. "Earthquake-Resistant Design with Rubber". In: *Earthquake-Resistant Design with Rubber* (1997).

[86] Maria Rosaria Marsico et al. "The Effect of Graphene Ultrasonic Coating on Recycled Rubber". In: *Advanced Engineering Materials* 24.11 (2022), p. 2200957. ISSN: 1527-2648.

[87] Xiaoping Chen et al. "Advances in Healthcare Electronics Enabled by Triboelectric Nanogenerators". In: *Advanced Functional Materials* 30.43 (2020), p. 2004673. ISSN: 1616-3028.

[88] Sihong Wang, Long Lin, and Zhong Lin Wang. "Triboelectric nanogenerators as self-powered active sensors". In: *Nano Energy* 11 (2015), pp. 436–462. ISSN: 2211-2855.

[89] Abdul Hadi Abdul Razak et al. "Foot Plantar Pressure Measurement System: A Review". In: *Sensors (Basel, Switzerland)* 12.7 (2012), p. 9884. ISSN: 14248220.

[90] Erik N. Kubiak et al. "Early weight bearing after lower extremity fractures in adults". In: *Journal of the American Academy of Orthopaedic Surgeons* 21.12 (2012), pp. 727–738. ISSN: 1067151X.

[91] Fazel Yavari and Nikhil Koratkar. “Graphene-based chemical sensors”. In: *Journal of Physical Chemistry Letters* 3.13 (2012), pp. 1746–1753. ISSN: 19487185.

[92] Qiyuan He et al. “Graphene -based electronic sensors”. In: *Chemical Science* 3.6 (2012), pp. 1764–1772. ISSN: 20416520.

[93] Xianghua Deng, Hao Tang, and Jianhui Jiang. “Recent progress in graphene-material-based optical sensors”. In: *Analytical and Bioanalytical Chemistry* 406.27 (2014), pp. 6903–6916. ISSN: 16182650.

[94] Haizhou Huang et al. “Graphene-based sensors for human health monitoring”. In: *Frontiers in Chemistry* 7.6 (2019), p. 399. ISSN: 22962646.